Analysis and Optimization of Transport and Reaction Processes in the Cylindrical Flow-Through Catalytic Membrane Reactors

Qaiser Abbas, BS Chemical Engineering

Submitted in fulfillment of the requirements for the degree of Master of Science in Chemical & Materials Engineering

School of Engineering and Digital Sciences

Department of Chemical & Materials Engineering

Nazarbayev University

53 Kabanbay Batyr Avenue,

Astana, Kazakhstan, 010000

Lead Supervisor: Prof. Boris Golman

Co-Supervisor: Prof. Piotr Sebastian Skrzypacz

April 2024

Declaration

I hereby affirm that this manuscript, titled "Analysis and Optimization of Transport and Reaction Processes in the Cylindrical Flow-Through Catalytic Membrane Reactor," is entirely my own creation, with the exception of adequately acknowledged quotations and citations.

Furthermore, to the best of my knowledge and belief, I certify that it has not been submitted in whole or in part for any other degree or diploma at Nazarbayev University or any other national or international institution previously or concurrently.

Name: Qaiser Abbas
Date: April 30th , 2024

Abstract

Cylindrical flow-through catalytic membrane reactors, employing porous membranes impregnated with catalysts, offer enhanced selectivity and yield in chemical reactions. This work is focused on mathematical modeling and numerical analysis of a cylindrical flow-through catalytic membrane reactor. The reactor's geometry, which incorporates a porous membrane, is specially tailored for the cylindrical configuration, addressing a research gap in realistic geometries. The proposed mathematical model includes a series of irreversible reactions with power-law kinetics occurring under non-isothermal conditions. A system of non-linear diffusion-convection-reaction equations is formulated for a cylindrical catalytic membrane reactor under both steady and unsteady-state. The study investigates the occurrence of dead zones within the membrane reactor as a result of rapid reactant depletion, a phenomenon that has not been extensively studied in prior literature for cylindrical membrane reactors. Problems with fractional reaction exponents require efficient numerical solvers since conventional iterative solvers encounter difficulties due to the fact that the power-law reaction term with fractional reaction exponent is not differentiable at the vanishing concentration. A novel time-marching scheme specifically designed for the cylindrical catalytic flow-through membrane reactor is developed and applied for simulations to get valuable insights into dead-core phenomena. The effects of dimensionless process parameters such as Thiele modulus, mass Peclet number, heat Peclet number, etc. and a model parameter (i.e., geometry parameter) on the concentration and temperature profiles, as well as dead-zone formation, are extensively investigated under steady-state. The simulation results demonstrate that these parameters affect the occurrence of dead zones and their size. The impact of convective flow on the reactor performance indicators under steady-state is also presented. Moreover, the investigation extends to unsteady-state conditions, exploring the dynamic behavior of concentration and temperature profiles as well as productivity under both isothermal and non-isothermal scenarios. In the case of a single reaction, the analysis of productivity reveals substantial percent increments, offering insights into the identification of optimal conditions. Finally, a comprehensive exploration into the optimal conditions for productivity in a sequential reaction is conducted.

Keywords: flow-through catalytic membrane reactor, cylindrical reactor geometry, power-law kinetics, dead zone formation, time-marching scheme, modified Crank-Nicolson scheme, optimization, forced periodic operations.

Acknowledgments

First, I would like to convey my greatest gratitude to my dedicated supervisors, Prof. Boris Golman and Prof. Piotr Sebastian Skrzypacz. Their unwavering guidance and encouragement throughout my academic journey have been crucial in completing my Master's program thesis. I express my sincere gratitude for the extensive amount of time dedicated to engaging and enlightening conversations.

Furthermore, I would like to express deep appreciation to the administrative staff at Nazarbayev University. Regularly operating in the background, their contributions, while occasionally going unnoticed, have been instrumental in fostering an academic atmosphere conducive to learning.

Finally, I extend my sincere thanks to my parents and wife, whose constant encouragement and support have been my pillars of strength. Their unwavering faith in my skills has consistently been a strong motivator, and I appreciate their influence in my life.

Table of Contents

List of Abbreviations & Symbols

Alphabet

B_{eff}	=	effective permeability of porous medium	$[m^2]$
C_i	=	concentration of component i within membrane	$[mol\ m^{-3}]$
$C_{i,\text{ exit}}$	=	concentration of component i within exhaust stream	$[mol\ m^{-3}]$
C_{i_0}	=	concentration of component i within feed stream	$[mol\ m^{-3}]$
c_i	=	dimensionless concentration of component i inside membrane	$[-]$
$\tilde{C}_{bA}$	=	time-independent bulk concentration	$[mol\ m^{-3}]$
c_p	=	fluid's specific heat capacity	$[J\ mol^{-1}K^{-1}]$
$c_{p,m}$	=	specific heat capacity of membrane	$[J\ mol^{-1}K^{-1}]$
$D_{i,\text{ eff}}$	=	effective diffusivity of component i	$[m^2 s^{-1}]$
E_i	=	activation energy of specific step	$[J\ mol^{-1}]$
$(-\Delta H)_\rho$	=	enthalpy of reaction ρ per mole of reactant i	$[J\ mol^{-1}]$
$\tilde{J}_{SS}$	=	average productivity under steady-state conditions	$[mol\ s^{-1}]$
$\tilde{J}_{USS}$	=	average productivity under unsteady-state conditions	$[mol\ s^{-1}]$
j_i	=	total molar flux of species i per unit cross-sectional area of membrane	$[mol\ m^{-2}s^{-1}]$
K_{eff}	=	effective thermal conductivity	$[J\ m^{-1}s^{-1}K^{-1}]$
k_ρ	=	reaction rate constant for reaction ρ	$[mol^{1-n}(m^3)^{n-1}s^{-1}]$
$k_{\rho,0}$	=	rate constant for reaction ρ determined at T_0	$[mol^{1-n}(m^3)^{n-1}s^{-1}]$

L	=	Membrane thickness	$[m]$
l	=	length of cylinder	$[m]$
P	=	pressure within membrane	$[Pa]$
Pe_m	=	mass Peclet number	$[-]$
Pe_h	=	heat Peclet number	$[-]$
q	=	heat flux per unit membrane's cross-sectional area	$[J\ m^{-2}s^{-1}]$
R_G	=	universal gas constant	$[J\ mol^{-1}K^{-1}]$
R_i	=	molar reaction rate of component i per unit volume of porous membrane	$[mol\ \ m^3\ \ s^{-1}]$
r	=	radial position in membrane	$[m]$
r_ρ		volumetric reaction rate of reaction ρ	$[mol\ \ m^3\ \ s^{-1}]$
r_{in}	=	inner radius of membrane	$[m]$
r_{out}	=	outer radius of membrane	$[m]$
S	=	selectivity of component *B*	$[-]$
T	=	temperature within membrane	$[K]$
T_0	=	temperature at the inlet of membrane porous space	$[K]$
$t_{d,A}$	=	characteristic diffusion time of species *A*	$[s]$
$t_{h,A}$	=	characteristic heat conductivity time	$[s]$
$\tilde{T}_b$	=	time-independent bulk temperature	$[K]$
u_D	=	filter velocity or Darcian fluid velocity within the porous membrane	$[m\ \ s^{-1}]$
X	=	conversion of component *A*	$[-]$
Y	=	yield of component *B*	$[-]$
z	=	dimensionless distance	$[-]$

Greek Symbols

β_1, β_2	=	Prater numbers	$[-]$
γ_1, γ_2	=	Arrhenius numbers	$[-]$
ρ_g	=	density of fluid	$[kg\ m^{-3}]$
ρ_m	=	density of membrane	$[kg\ m^{-3}]$
$\varsigma_{i\rho}$	=	stoichiometric coefficient of species i in reaction ρ	$[-]$
φ_1, φ_2	=	Thiele moduli	$[-]$
δ	=	geometry parameter	$[-]$
ζ	=	ratio of inlet concentrations of component *A* raised to the power of reaction exponents	$[-]$
θ	=	dimensionless temperature	$[-]$
μ	=	dynamic viscosity of fluid phase	$[kg\ m^{-1}s^{-1}]$
ψ	=	effective diffusivities ratio	$[-]$
ε	=	porosity of the membrane	$[-]$
ω_{mA}, ω_h	=	angular frequencies	$[-]$
Θ	=	ratio of unsteady-state productivity to steady-state productivity	$[-]$

Subscripts and superscripts

j	=	spatial step
n	=	time step

List of Figures

List of Tables

Chapter 1 – Introduction

1.1 Overview of the topic

Cylindrical flow-through catalytic membrane reactors are devices that employ porous membranes impregnated with catalysts to increase yield and productivity in chemical reactions. This reactor design facilitates enhanced catalytic activity by ensuring intensive contact between reactants and catalysts while minimizing mass transport resistances [1]. The porous membrane, predominantly constructed from ceramic material, does not serve any separative function but is exclusively employed as microstructured catalyst support. Cylindrical catalytic membrane reactors offer advantages over conventional reactor configurations like packed beds and monoliths, facilitating intensive contact between reactants and catalysts, ensuring continuous operation with regulated residence times, and promoting higher selectivity while minimizing undesirable byproducts [1][2][3][4][5][6].

In study [7], a mathematical model of a flow-through catalytic membrane reactor was developed for non-isothermal series reactions with linear kinetics. The findings confirmed that using a membrane reactor substantially improved both the yield and selectivity of an intermediate product in the case of first-order series reactions. Furthermore, the study [8] focused on developing stationary model equations with power-law kinetics of fractional order under the assumptions of the large ratio of the membrane diameter to the membrane wall thickness. However, a noticeable research gap exists in developing these models for the case of realistic cylindrical geometry of membrane reactors. In this work, we aim to fill this gap by constructing more accurate model equations for cylindrical membrane reactors, taking into account for the new terms in the mass and heat balance equations. The stationary model equations with fractional reaction exponents are specifically tailored to the cylindrical geometry and can be employed in many significant industrial reactions [9][10]. In reaction systems governed by power-law kinetics with fractional reaction exponents, rapid depletion of reactants can induce the formation of regions where the reactant concentration reaches zero. Those regions within the reactor where reactants vanish entirely and chemical reactions cease are called dead zones [9][11][12][13].

1.2 Problem statement

The unique design of cylindrical flow-through catalytic membrane reactors involving porous membranes impregnated with catalysts offers great potential for improving the

selectivity and yield of chemical reactions. However, a noticeable gap exists in the literature regarding the development of accurate mathematical models tailored specifically for cylindrical reactor geometries. Limited research has been undertaken regarding cylindrical reactor designs, as the available literature predominantly focuses on planar configurations, hence neglecting the distinctive complexities associated with cylindrical reactors. Moreover, the formation of dead zones in these reactors, caused by the rapid depletion of reactants, has not been sufficiently investigated. The lack of comprehensive mathematical models and numerical analyses limits our understanding of cylindrical flow-through catalytic membrane reactor performance. Addressing this gap requires the development of robust mathematical models capable of capturing the complexities of mass and heat transfer, reaction kinetics, and dead core formation within cylindrical membrane reactors. In addition, it is necessary to employ effective numerical algorithms to simulate the behavior of reactors under both steady-state and unsteady-state conditions, taking into account the impact of geometric parameters, reaction kinetics, and process parameters. Traditional iterative solvers are rendered impractical due to the non-differentiability of the nonlinear power-law reaction term when concentrations approach zero. Existing solvers from the literature, including those proposed by [14][15][16][17][18], have proven to be relatively inefficient in addressing dead-zone phenomena. In light of these challenges, our research aims to investigate and develop an efficient solver for such nonlinear problems involving power-law kinetics.

Furthermore, one of the common challenges encountered in industrial gas-solid catalytic reactions is the attainment of maximum selectivity for intermediate products formed in series or series-parallel complex exothermic reactions. Addressing this challenge is critical for optimizing process efficiency while minimizing the formation of undesirable byproducts. Flow-through catalytic membrane reactors could be one of the promising solutions to enhance the selectivity of our intermediate desired products. The purpose of this research is also to investigate and address the complexities associated with the use of flow-through membrane reactors, with an emphasis on maximizing selectivity and minimizing byproduct formation in significant industrial catalytic processes.

1.3 Aim, objectives, and structure of report

This research aims to investigate the performance of cylindrical flow-through catalytic membrane reactors in series and series-parallel reactions with power-law kinetics of fractional order under steady and unsteady-state conditions. Moreover, the formation of dead zones in

such reactors will be studied, and the performance indicators, such as selectivity, yield and productivity of these reactors under steady and unsteady-state conditions, will also be investigated. To attain these objectives, the research is focused on:

- Derivation of the general and dimensionless systems of nonlinear differential equations for concentrations and temperature distributions in the reactor, taking into account the diffusion, conduction, convection, and reaction processes.
- To create an appropriate time-marching scheme tailored to our model of the cylindrical catalytic flow-through membrane reactor.
- Development and implementation of the numerical algorithm, including writing Python code to efficiently solve the systems of nonlinear differential equations for concentrations and temperature distributions.
- Comparison of our cylindrical geometry model of a membrane reactor with the previously established planar model.
- Analysis of the effects of different process and model parameters on concentrations and temperature profiles within reactor under both isothermal and non-isothermal conditions.
- Formulation of the reactor performance indicators such as conversion, selectivity, and yield. Moreover, a parametric study will be conducted to see the influence of mass and heat Peclet numbers on the performance indicators of the reactor, including selectivity and yield under both isothermal and non-isothermal conditions.
- Investigate and compare the productivity of the desired product under both forced unsteady-state and steady-state conditions.

The thesis comprises six chapters, structured as follows: Chapters 1 and 2 provide the introduction and literature review, elucidating the thesis's overview, problem statement, and objectives, along with a comprehensive examination of prior research on catalytic membrane reactors. In Chapter 3, a detailed presentation of the mathematical model is offered, encompassing model and process parameters and presenting dimensionless model equations for steady and unsteady state conditions. Chapter 4 is dedicated to the formulation of the time-marching method, employing the modified Crank-Nicolson scheme. The accuracy of this method is validated through the determination of absolute maximum error and rate of convergence, with further proof of its convergence towards the steady-state solution. Additionally, this section outlines the numerical scheme for unsteady state conditions. Chapter 5 delves into the presentation of simulation results and discussions, exploring both steady and unsteady state conditions for a cylindrical flow-through membrane reactor. The thesis concludes with Chapter 6, summarizing key findings and insights.

Chapter 2 – Literature Review

The scientific term "membrane reactor" was initially introduced in the chemical engineering literature around 1980 [19]. Over the past few decades, this area of research has been increasingly popular among the scientific community. A membrane reactor is a device that combines reaction and separation processes in a single system [20]. It is made from various materials, including metals, ceramics, and polymers. There are various definitions for membrane reactors (MRs) [21]. According to the International Union of Pure and Applied Chemistry (IUPAC), a membrane reactor is a device that carries out a reaction and separation using a membrane within the same physical containment [22]. A membrane reactor is defined as any reactor where a chemical reaction occurs in the presence of a membrane when considering a broader interpretation [23]. The application of membrane reactors has attracted considerable interest over the last fifty years, resulting in an enormous amount of published literature on the topic [3][24][25]. The major difficulty in chemical reaction engineering is the limitation of yield and selectivity for specific reaction products. The presence of a membrane in a membrane reactor actively contributes to the chemical conversion process, resulting in improved yield, selectivity, and reaction rates [3].

2.1 Categories of membrane reactors

Different types of membranes can be categorized according to their specific features, separation methods, and configurations. Membranes can be divided into two main groups based on their nature: synthetic or biological. These categories differ in terms of functionality and the structure of the membrane. Although biological membranes have limitations such as a restricted pH range, vulnerability to microorganisms, and sensitivity to operating temperature, they are easily produced. Conversely, synthetic membranes can be further categorized into inorganic and organic. Inorganic membranes generally can withstand temperatures above 250°C, whereas organic membranes function within the temperature range of 100-300°C [26].

Moreover, inorganic membranes can be classified into two main types: porous and dense membranes. Porous membranes possess a high degree of permeability but lower selectivity, which can be differentiated and further categorized based on the pores' size [27]. Selecting various membrane types depends on individual research requirements and application needs.

Membrane reactor (MR) systems can be built in either flat or tubular geometries. Tubular membrane reactors, depicted in **Figure 2.1**, can be further classified according to distinct features and design factors [5].

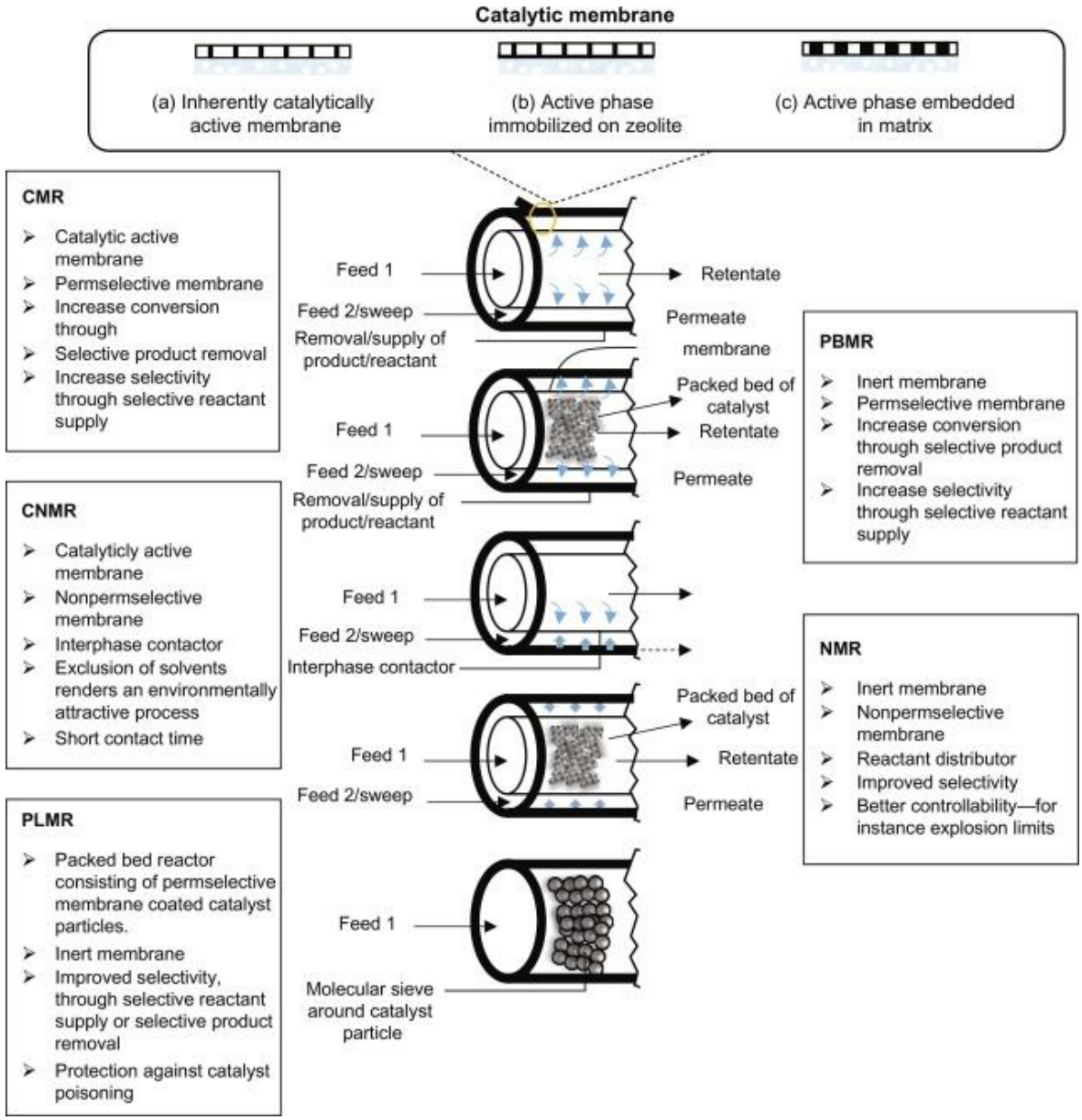

Figure 2.1 Categorization of membrane reactors according to the function and position of the membrane [5]

2.2 Catalytic membrane reactors

Membrane reactors that incorporate catalysts (CMRs) are categorized into three distinct categories: extractor, distributor, and contactor reactors [28][29]. The reactor classifications are illustrated in **Figure 2.2.**

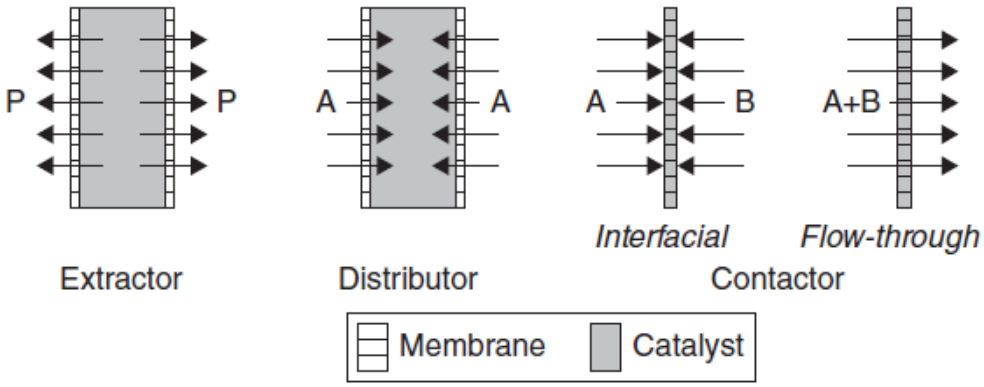

Figure 2.2 Illustration of the position of catalyst in membrane reactors, where A and B are reactants, and P is a product [28]

The extractor mode is employed to selectively remove products from the reaction mixture, while the distributor mode is utilized to regulate the addition of reactants to the reaction mixture. Ultimately, the contactor mode is employed to enhance the efficiency of the interaction between the reactants and the catalyst. An active contactor mode membrane reactor functions as a forced flow-through system, with the membrane acting as both a diffusion barrier and a catalytically active component [3][24]. This particular membrane type forms a reaction zone in which the catalyst is impregnated within the membrane's pores, resulting in enhanced catalytic activity [24][30].

2.3 Flow-through catalytic membrane reactors

The concept of a flow-through catalytic membrane reactor (FTCMR) delineates a novel approach to heterogeneous reactions, wherein the catalyst is immobilized within the pores of a predominantly ceramic membrane. These pores facilitate the movement of the reaction mixture through convection and diffusion [31]. Unlike membranes with separative functions, the porous membrane primarily serves as a "microstructured catalyst support." This reactor design facilitates heightened catalytic activity by ensuring intensive contact between reactants and catalysts, potentially resulting in a narrow residence time distribution [20][3][5][32][1].

A distinctive advantage of these reactors, in contrast to conventional counterparts like packed beds and monoliths, lies in their capability to regulate the residence time of products and reactants within the catalytic structure by imposing an external pressure gradient. This control mechanism offers the potential to positively influence selectivity, yield, and catalyst lifespan by effectively "flushing out" undesired byproducts from the immediate reaction zone.

The desired product in many industrial gas-solid catalytic reactions is frequently an intermediate product formed in series or series-parallel complex exothermic reactions. In such cases, flow-through membrane reactors are one of the promising solutions for enhancing the selectivity of intermediate desirable products while concurrently minimizing byproduct formation. Flow-through membrane reactors have proven to be effective in various processes, such as the formation of propylene oxide through partial oxidation [33], the production of biodiesel through esterification [34], partial hydrogenation of 1,5-cyclooctadiene [35], partial hydrogenation of polyunsaturated hydrocarbons [36], partial oxidation of methane to formaldehyde [37], reduction of nitrate/nitrite [38], and the degradation of waterborne environmental pollutants [39][40]. Multiple laboratory studies support these claims. Moreover, the outstanding efficacy of these reactors can be attributed to their extensive specific surface area, spacious pore volume, and improved mass transfer enabled by forced convection [1].

The study [36] investigated the selectivity of partial hydrogenation reactions of unsaturated substrates in a membrane reactor operating at a temperature of 323 K and a hydrogen pressure of 40 bar. The membrane, composed of cross-linked polyacrylic acid (PAA), incorporated palladium nanoparticles as catalysts, resulting in a well-defined pore structure and facilitating the enhanced mass transport of the reaction mixture. The selectivity for partially hydrogenated products was evaluated based on the pore size of the PAA membrane and compared to commercially available catalysts, namely Pd/C and Pd/Al_2O_3. The results showed notable improvements in selectivity when using the membrane reactor compared to tests performed with supported catalysts in slurry and fixed bed reactors. The selectivity enhancements varied from 3% for 1-octyne to a maximum of 40% for geraniol. The results emphasize the capability of membrane reactor technology to increase the selectivity of products in partial hydrogenation reactions, providing possibilities for enhanced process efficiency and product quality.

The study [35] explored the partial hydrogenation of 1,5-cyclooctadiene within a pore-flow-through membrane reactor. The reactor operated at a temperature of 50°C and a hydrogen pressure of 1 MPa. The membrane reactor effectively minimized mass transfer limitations when compared to traditional reactors that utilize millimeter-sized spherical catalyst pellets in fixed-bed or slurry configurations. The conversion rate of 1,5-cyclooctadiene in the membrane reactor was predominantly affected by the quantity of palladium (Pd) and the mass flow rate of the reaction mixture passing through the membrane. Under ideal conditions, a remarkable level of selectivity of 95% for cyclooctene was attained when 1,5-cyclooctadiene was

completely converted. The results emphasize the efficacy of the membrane reactor in obtaining a high level of selectivity and overcoming restrictions in mass transfer.

2.4 Dead Zones

The term "dead zone" was initially coined by Temkin [41] to describe a region in the reactors devoid of chemical reactions due to the absence of reactants. The formation of dead zones has been discovered in numerous applications, such as the hydrogenation of propylene using a commercially available catalyst [9], enzyme-catalyzed bioreactions [42], and flow-through catalytic membrane reactors [8].

These zones can arise due to a range of causes, including suboptimal reactor design, catalyst deterioration, etc. [43][44][45]. In order to maximize the performance and efficiency of flow-through catalytic membrane reactors, it is crucial to understand and mitigate the presence of dead zones in advance.

Researchers and engineers can enhance the performance of flow-through catalytic membrane reactors and optimize reaction efficiency by addressing these dead zones. Furthermore, the presence of dead zones results in an uneven distribution of reactants and products, which may subsequently give rise to variations in reaction rates and product selectivity. This may lead to reduced overall conversion and yield and inefficient catalyst utilization. By eliminating or minimizing these dead cores, we can attain better and more uniform reactant distribution, increased conversion rates, selectivity, and enhanced product quality [46][7].

Extensive research and development have been focused on mitigating the presence of dead zones in flow-through catalytic membrane reactors. Several solutions have been suggested and examined to tackle the root causes of dead zone formation and reduce their negative impact on reactor performance [47]. One approach involves optimising the design parameters of the reactor, such as its geometry, flow distribution, and catalyst location, in order to enhance fluid mixing and minimise the occurrence of stagnant zones. Computational fluid dynamics (CFD) models and experimental validation studies have played a crucial role in identifying the best reactor configurations that minimise the creation of dead zones while maximising mass transport and reaction kinetics [48].

Furthermore, advancements in developing advanced catalyst materials and formulations have become a promising strategy for reducing dead zones in membrane reactors. Tailored catalyst structures with enhanced activity, stability, and selectivity can enhance reaction efficiency and reduce the negative effects of localised dead zones on the overall performance of the reactor. Moreover, the incorporation of catalyst coatings or functionalization procedures onto membrane surfaces could improve catalytic activity while promoting an even distribution of reactants across the entire reactor volume [1][48].

The occurrence of dead zones in membrane reactors and catalyst pellets is an intricate phenomenon impacted by multiple physical and chemical factors. Gaining a more profound comprehension of the fundamental principles is crucial for developing efficient mitigation methods and maximising reactor performance [48]. Fluid dynamics are crucial in determining the flow patterns inside membrane reactors and catalyst pellets, which in turn affect the creation of stagnant areas known as dead zones. Membrane reactors may experience non-uniform fluid flow and recirculation zones, resulting in localised regions with restricted mass transfer. These regions might become stagnant and lack chemical reactions. These flow patterns might occur as a result of limitations in shape, the impact of the layer of fluid at the surface, or inconsistencies in the way the flow is distributed [12]. Diffusion restrictions and pore-scale transport phenomena are factors that lead to the creation of dead zones within catalyst pellets. In catalyst beds with high density, the movement of reactants into the inner pores can be restricted due to mass transport limits. This can lead to uneven reaction rates and localised depletion of reactants. In addition, temperature and concentration gradients intensify mass transport constraints, resulting in the creation of stationary areas inside the catalyst bed [9].

Chapter 3 – Mathematical Model

In this work, we consider a one-dimensional cylindrical-catalytic membrane reactor model. A porous membrane with embedded catalysts in the pore walls transforms the reactant *A* into the product. An intermediate product *B* is followed by the final product *C*. **Figure 3.1** shows the schematics of the cylindrical catalytic membrane reactor, where r_{in} is the inner radius and r_{out} is the outer radius of the membrane. The thickness of the membrane is denoted by $L = r_{out} - r_{in}$. In order to derive our model equations, a cylindrical shell of thickness Δr located at a radius r within a membrane tube is considered.

As depicted in **Figure 3.1**, the membrane's one end is closed, forcing the reactant delivered from the open end to flow through the membrane. The unreacted reactant *A* and the products *B* and *C* formed in the membrane are removed from the reactor from the other end of the reactor.

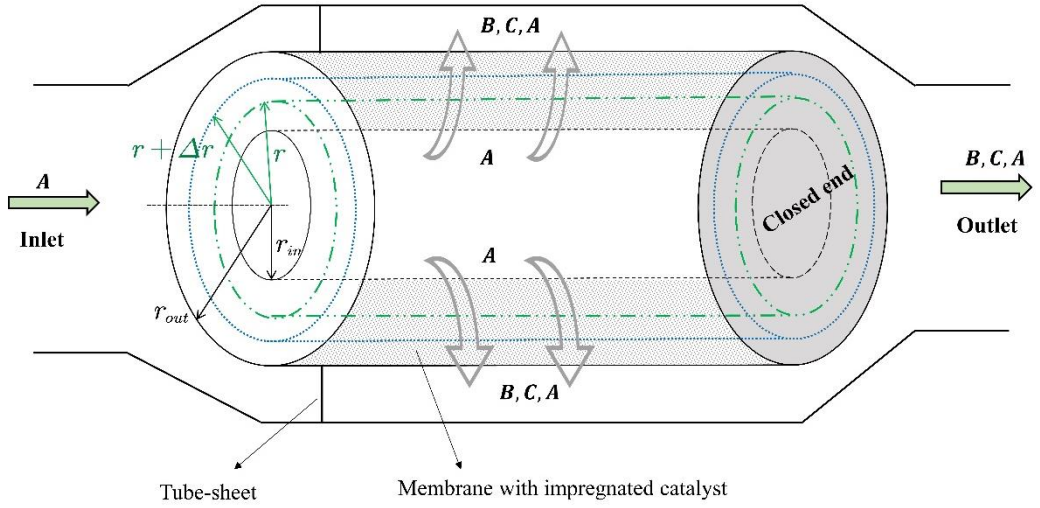

Figure 3.1 Schematics of cylindrical flow-through catalytic membrane reactor

3.1 Model equations for steady-state

In the following, irreversible consecutive reactions occurring under non-isothermal conditions are considered

$$A \xrightarrow{k_1} B \xrightarrow{k_2} C \tag{3.1}$$

In this case, *A* denotes the reactant that is fed into the membrane pores from the inner side of the catalytic membrane. At the same time, *B* is the desired intermediate product that emerges from the outer side of the membrane before undergoing subsequent conversion into *C*. The mass and heat balances for the first-order consecutive reactions by Eq. (3.1) in the flow-through reactor were established in the study [7]. In this work, reactions exhibiting power-law kinetics in a cylindrical geometry closely resembling more realistic conditions are investigated. The reaction rates for the first and second steps for (3.1) are respectively represented as:

$$\begin{aligned} r_1 &= k_1 {C_A}^{p_1} , \\ r_2 &= k_2 {C_B}^{p_2} , \end{aligned} \tag{3.2}$$

where k_1 and k_2 denote reaction rate constants, while p_1 and p_2 represent reaction exponents.

To derive the mass and heat balances, a cylindrical shell of thickness Δr located at a radius r within a membrane tube is considered, as shown in **Figure 3.1**. The expression for the steady-state differential mass balance of the gaseous component i is stated as follows

$$\frac{1}{r}\frac{d(j_i \cdot r)}{dr} - R_i = 0, \tag{3.3}$$

where j_i represents the molar flux of species i (either *A* or *B*) per unit cross-sectional area. The molar reaction rate of component i per unit volume of porous media, denoted as R_i is expressed by the following equation:

$$R_i = \sum_{\rho} \varsigma_{i\rho} r_\rho, \tag{3.4}$$

where $\varsigma_{i\rho}$ is the stoichiometric coefficient of species i and r_ρ is the reaction rate in reaction ρ.

Similarly, the energy balance equation can be written as

$$\frac{1}{r}\frac{d(q \cdot r)}{dr} - \sum_{\rho} (-\Delta H)_\rho r_\rho = 0, \tag{3.5}$$

where q represents the heat flux while $(-\Delta H)_\rho$ is the heat of reaction per mole of component i.

In this study, the molar diffusion flux of species i in the radial direction, $j_{i,\mathrm{diff}}$, can be defined using the Ficks's first law

$$j_{i,\text{diff}} = -D_{i,\text{eff}} \frac{dC_i}{dr}, \tag{3.6}$$

where $D_{i,\text{eff}}$ is the effective diffusivity of component i in the membrane porous structure.

The Darcy equation is employed to describe the convective flow through a porous media. The flow velocity within the porous membrane structure is defined as:

$$u_D = -\frac{B_{\text{eff}}}{\mu} \frac{dP}{dr}, \tag{3.7}$$

where u_D is the filter velocity (also known as the Darcian fluid velocity). It can be defined as the average flow rate over the cross-sectional area of a porous media. The parameter B_{eff} denotes the effective permeability of the porous medium, μ is the fluid viscosity and $\frac{dP}{dr}$ is the pressure gradient in the direction of flow.

The total molar flux of species i through the porous medium of the membrane given as

$$j_i = -D_{i,\text{eff}} \frac{dC_i}{dr} + u_D C_i, \tag{3.8}$$

is a combination of molar fluxes by diffusion and convection of species i in the membrane porous space.

The total heat flux through the porous medium of the membrane involves effective conduction and convective transport terms, which can be expressed as

$$q = -K_{\text{eff}} \frac{dT}{dr} + \rho_g c_p u_D T \ , \tag{3.9}$$

where K_{eff} is the effective thermal conductivity, dependent on the membrane's porous structure, membrane conductivity, and fluid conductivity, ρ_g is the fluid density, c_p is the fluid's specific heat capacity, and T is the temperature inside the membrane.

Let us substitute Eqs. (3.8) and (3.9) into Eq. (3.3) and Eq. (3.5) , respectively. According to the chain rule of differentiation, the derivative terms can be expanded, and the final equations become:

$$D_{i,\text{ eff}} \frac{d^2 C_i}{dr^2} + \left(\frac{D_{i,\text{ eff}}}{r} - u_D \right) \frac{dC_i}{dr} + \left(R_i - \frac{u_D C_i}{r} \right) = 0 \ , \tag{3.10}$$

$$K_{i,\text{eff}}\frac{d^2T}{dr^2}+\left(\frac{K_{i,\text{eff}}}{r}-\rho_g c_p u_D\right)\frac{dT}{dr}+\left(\sum_\rho(-\Delta H)_\rho r_\rho-\frac{\rho_g c_p u_D}{r}T\right)=0\ . \quad (3.11)$$

To finalize our model, it is necessary to define a reaction term within the systems of Eq. (3.10) and Eq. (3.11). The reaction term for power-law kinetics for successive reaction Eq. (3.1) is defined as

$$\begin{aligned} R_A &= -r_1\ , \\ R_B &= -r_2+r_1\ , \end{aligned} \quad (3.12)$$

where r_1 and r_2 are defined due to Eq. (3.2). According to the Arrhenius equation, the reaction rate constant k_i at temperature T is defined as

$$k_i = k_{i,0}\cdot\exp\left(-\frac{E_i}{R_G}\left(\frac{1}{T}-\frac{1}{T_0}\right)\right), \quad (3.13)$$

where $k_{i,0}$, E_i, T_0, and R_G denote the rate constant determined at T_0, activation energy, temperature at the inlet of the membrane porous space, and universal gas constant, respectively.

3.1.1 Dimensional model equations

Combining Eqs. (3.12), and (3.13) along with Eq. (3.2) into Eqs. (3.10), and (3.11) results in the final system of nonlinear differential equations for unknown concentrations and temperature ($C_A,\ C_B,$ and T) in the porous membrane, i.e., $r_{in}<r<r_{out}$:

$$\begin{aligned} D_{A,\text{eff}}\frac{d^2C_A}{dr^2}+\left(\frac{D_{A,\text{eff}}}{r}-u_D\right)\frac{dC_A}{dr}-k_{1,0}\cdot\exp\left(\frac{-E_1}{R_G}\left(\frac{1}{T}-\frac{1}{T_0}\right)\right){C_A}^{p_1}-\frac{u_D}{r}C_A &= 0, \\ D_{B,\text{eff}}\frac{d^2C_B}{dr^2}+\left(\frac{D_{B,\text{eff}}}{r}-u_D\right)\frac{dC_B}{dr}+k_{1,0}\cdot\exp\left(\frac{-E_1}{R_G}\left(\frac{1}{T}-\frac{1}{T_0}\right)\right){C_A}^{p_1} & \\ -\ k_{2,0}\cdot\exp\left(\frac{-E_2}{R_G}\left(\frac{1}{T}-\frac{1}{T_0}\right)\right){C_B}^{p_2}-\frac{u_D}{r}C_B &= 0, \\ K_{\text{eff}}\frac{d^2T}{dr^2}+\left(\frac{K_{\text{eff}}}{r}-\rho_g c_p u_D\right)\frac{dT}{dr}+k_{1,0}\cdot\exp\left(\frac{-E_1}{R_G}\left(\frac{1}{T}-\frac{1}{T_0}\right)\right){C_A}^{p_1}\cdot(-\Delta H_1) & \\ +k_{2,0}\cdot\exp\left(\frac{-E_2}{R_G}\left(\frac{1}{T}-\frac{1}{T_0}\right)\right){C_B}^{p_2}\cdot(-\Delta H_2)-\frac{\rho_g c_p u_D}{r}T &= 0. \end{aligned} \quad (3.14)$$

The Dirichlet boundary conditions are applied at the member's inlet, i.e. $r = r_{in}$ as follows:

$$C_A = C_{A,0},\ C_B = 0,\ T = T_0, \tag{3.15}$$

where the specified concentration and temperature at the inlet are denoted as $C_{A,0}$ and T_0, respectively. Similarly, the Neumann boundary conditions are imposed at the outlet of the membrane at $r = r_{out}$ given as

$$\frac{dC_A}{dr} = \frac{dC_B}{dr} = \frac{dT}{dr} = 0. \tag{3.16}$$

3.1.2 Dimensionless model equations

To generate the dimensionless form of the system of nonlinear differential equations described in Eq. (3.14), the dimensionless parameters specified in **Table 3.1** are applied. Let

$$z = \frac{r - r_{in}}{L},\ c_A = \frac{C_A}{C_{A0}},\ c_B = \frac{C_B}{C_{A0}},\ \theta = \frac{T}{T_0}$$

be the radial position in the membrane, concentration of A, concentration of B , and temperature, respectively. Then, the steady-state mass and heat balance are represented by the dimensionless equations as follows

$$\begin{aligned}
&\frac{d^2c_A}{dz^2} + \left(\frac{1}{\delta + z} - Pe_m\right)\frac{dc_A}{dz} - {\varphi_1}^2 \cdot \exp\left(\gamma_1\left(1 - \frac{1}{\theta}\right)\right){c_A}^{p_1} - \frac{Pe_m}{\delta + z}c_A = 0,\\
&\frac{d^2c_B}{dz^2} + \left(\frac{1}{\delta + z} - Pe_m\psi\right)\frac{dc_B}{dz} + {\varphi_1}^2\psi \cdot \exp\left(\gamma_1\left(1 - \frac{1}{\theta}\right)\right){c_A}^{p_1}\\
&\qquad - {\varphi_2}^2\zeta \cdot \exp\left(\gamma_2\left(1 - \frac{1}{\theta}\right)\right){c_B}^{p_2} - \frac{Pe_m\psi}{\delta + z}c_B = 0,\\
&\frac{d^2\theta}{dz^2} + \left(\frac{1}{\delta + z} - Pe_h\right)\frac{d\theta}{dz} + {\varphi_1}^2\beta_1 \cdot \exp\left(\gamma_1\left(1 - \frac{1}{\theta}\right)\right){c_A}^{p_1}\\
&\qquad + {\varphi_2}^2\beta_2\zeta \cdot \exp\left(\gamma_2\left(1 - \frac{1}{\theta}\right)\right){c_B}^{p_2} - \frac{Pe_h}{\delta + z}\theta = 0.
\end{aligned} \tag{3.17}$$

In the context of cylindrical geometry, an additional dimensionless parameter is introduced and referred to as δ . This parameter is defined as the ratio of the inner radius r_{in} to the thickness L of the membrane, expressed as follows

$$\delta = \frac{r_{in}}{L}. \tag{3.18}$$

The presence of geometry parameter δ and terms involving this parameter in model equations distinguish the current formulation from prior work [8]. It is worth mentioning that the incorporation of δ is crucial in order to define the geometric characteristics of the cylindrical framework accurately. As the value of δ from Eq. (3.18) tends towards infinity, it will result in the planar geometry case. Moreover, it also improves the model's fidelity, making it more representative of actual cylindrical catalytic membrane reactor configurations. By incorporating δ, the current work aligns with real-world circumstances and recognizes the potential importance of cylindrical shapes in practical applications. Further analysis of it is discussed in the Results and Discussion section. The dimensionless boundary conditions for the dimensionless mass and heat balance Eq. (3.17) are defined as follows:

$$\text{at} \quad z = 0: \quad c_A = 1, \; c_B = 0, \; \theta = 1 \tag{3.19}$$

$$\text{at} \quad z = 1: \quad \frac{dc_A}{dz} = \frac{dc_B}{dz} = \frac{d\theta}{dz} = 0 \; . \tag{3.20}$$

Table 3.1 Dimensionless parameters

Dimensionless Group	Definition
Mass Peclet number	$Pe_m = \frac{u_D L}{D_{A,\text{eff}}}$
Heat Peclet number	$Pe_h = \frac{\rho_g c_p u_D L}{K_{\text{eff}}}$
Thiele moduli	$\varphi_1 = \left(\frac{L^2 k_{1,0} \; {C_{A0}}^{p_1 - 1}}{D_{A,\text{eff}}}\right)^{1/2}, \; \varphi_2 = \left(\frac{L^2 k_{2,0} \; {C_{A0}}^{p_1 - 1}}{D_{B,\text{eff}}}\right)^{1/2}$
Geometry parameter	$\delta = \frac{r_{in}}{L}$
Arrhenius numbers	$\gamma_1 = \frac{E_1}{R_G T_0}, \; \gamma_2 = \frac{E_2}{R_G T_0}$
The energy generation functions, Prater numbers	$\beta_1 = \frac{D_{A,\text{eff}} C_{A0} (-\Delta H_1)}{K_{\text{eff}} T_0}, \; \beta_2 = \frac{D_{\text{eff},B} \; C_{A0} (-\Delta H_2)}{K_{\text{eff}} T_0}$
Effective diffusivities ratio	$\psi = \frac{D_{A,\text{eff}}}{D_{B,\text{eff}}}$
Ratio of inlet concentration powers	$\zeta = \frac{{C_{A0}}^{p_2}}{{C_{A0}}^{p_1}}$

3.2 Model equations for unsteady state

The next step involves formulating a mathematical model under unsteady-state conditions, presenting corresponding equations for the concentrations of *A* and *B*, as well as the temperature.

$$\varepsilon \frac{\partial C_A}{\partial t} = \varepsilon D_{A,\text{eff}}\, r^{-1} \frac{\partial}{\partial r}\left(r \frac{\partial C_A}{\partial r}\right) - \varepsilon \frac{u_D}{r} \frac{\partial (rC_A)}{\partial r} - (1-\varepsilon) R_A \tag{3.21}$$

$$\varepsilon \frac{\partial C_B}{\partial t} = \varepsilon D_{B,\text{eff}}\, r^{-1} \frac{\partial}{\partial r}\left(r \frac{\partial C_B}{\partial r}\right) - \varepsilon \frac{u_D}{r} \frac{\partial (rC_B)}{\partial r} + (1-\varepsilon)\,(R_A - R_B) \tag{3.22}$$

$$\rho_m c_{p,m} \frac{\partial T}{\partial t} = K_e r^{-1} \frac{\partial}{\partial r}\left(r \frac{\partial T}{\partial r}\right) - \frac{\rho_g c_p u_D}{r} \frac{\partial (rT)}{\partial r} + R_A (-\Delta H)_A + R_B (-\Delta H)_B \tag{3.23}$$

Here ρ_m and $c_{p,m}$ are the density and specific heat capacity of the membrane with the gas or fluid in the pores, respectively. ρ_g and c_p are the density and specific heat capacity of fluid, respectively, in membrane pores. ε is the porosity of the membrane.

3.2.1 Dimensional model equations

Combining Eqs. (3.12), and (3.13) along with Eq. (3.2) into Eqs. (3.21), (3.22) and (3.23) results in the final system of nonlinear differential equations for unknown concentrations and temperature ($C_A,\ C_B,$ and T) for unsteady state conditions in the porous membrane, i.e.,

$$\varepsilon \frac{\partial C_A}{\partial t} = \varepsilon D_{A,\text{eff}} \frac{\partial^2 C_A}{\partial r^2} + \varepsilon\left(\frac{D_{A,\text{eff}}}{r} - u_D\right)\frac{\partial C_A}{\partial r} - (1-\varepsilon) k_{1,0} \cdot \exp\left(\frac{-E_1}{R_G}\left(\frac{1}{T} - \frac{1}{T_0}\right)\right) {C_A}^{p_1} - \varepsilon \frac{u_D}{r} C_A,$$

$$\varepsilon \frac{\partial C_B}{\partial t} = \varepsilon D_{B,\text{eff}} \frac{\partial^2 C_B}{\partial r^2} + \varepsilon\left(\frac{D_{B,\text{eff}}}{r} - u_D\right)\frac{\partial C_B}{\partial r} + (1-\varepsilon) k_{1,0} \cdot \exp\left(\frac{-E_1}{R_G}\left(\frac{1}{T} - \frac{1}{T_0}\right)\right) {C_A}^{p_1} - (1-\varepsilon)\ k_{2,0} \cdot \exp\left(\frac{-E_2}{R_G}\left(\frac{1}{T} - \frac{1}{T_0}\right)\right) {C_B}^{p_2} - \varepsilon \frac{u_D}{r} C_B,$$

$$\rho_m c_{p,m} \frac{\partial T}{\partial t} = K_{\text{eff}} \frac{\partial^2 T}{\partial r^2} + \left(\frac{K_{\text{eff}}}{r} - \rho_g c_p u_D\right)\frac{\partial T}{\partial r} + k_{1,0} \cdot \exp\left(\frac{-E_1}{R_G}\left(\frac{1}{T} - \frac{1}{T_0}\right)\right) {C_A}^{p_1} \cdot (-\Delta H_1) + k_{2,0} \cdot \exp\left(\frac{-E_2}{R_G}\left(\frac{1}{T} - \frac{1}{T_0}\right)\right) {C_B}^{p_2} \cdot (-\Delta H_2) - \frac{\rho_g c_p u_D}{r} T. \tag{3.24}$$

3.2.2 Dimensionless model equations

Now, the dimensionless form of the system of nonlinear differential equations will be generated, as described in Eq. (3.24). As the catalytic reaction proceeds under the forced unsteady-state conditions, the bulk concentration C_b of species *A* and bulk temperature T_b at the reactor inlet are changed with respect to dimensionless time τ as follows:

$$\begin{aligned} C_{bA}(\tau) &= \tilde{C}_{bA} + \hat{C}_{bA}(\tau), \\ T_b(\tau) &= \tilde{T}_b + \hat{T}_b(\tau). \end{aligned} \tag{3.25}$$

Here, $\tilde{C}_{bA}$ and $\tilde{T}_b$ denote the time-independent bulk concentration and bulk temperature, respectively.

The dimensionless concentrations and temperature are expressed in terms of $\tilde{C}_{bA}$ and $\tilde{T}_b$, respectively, i.e. $c_A(z,\tau) = \frac{C_A(r,t)}{\tilde{C}_{bA}}, c_B(z,\tau) = \frac{C_B(r,t)}{\tilde{C}_{bA}},$ and $\theta(z,\tau) = \frac{T(r,t)}{\tilde{T}_b}$.

Assuming that we treat the gas and solid phases as a single isothermal pseudo-homogenous phase, then $\tilde{T}_b$ represents the temperature of the pseudo-homogenous phase [49].

Therefore, the dimensionless bulk concentration and bulk temperature are defined by the following equations, respectively.

$$\begin{aligned} c_{bA}(\tau) &= 1 + \hat{c}_{bA}(\tau), \\ \theta_b(\tau) &= 1 + \hat{\theta}_b(\tau). \end{aligned} \tag{3.26}$$

Conditions that are necessary in order to compare the time-dependent catalytic processes with each other at identical average bulk concentrations and temperatures are given as:

$$\begin{aligned} \int_0^{\tau_c} \hat{c}_{bA}(\tau)\, d\tau &= 0, \\ \int_0^{\tau_\theta} \hat{\theta}_b(\tau)\, d\tau &= 0. \end{aligned} \tag{3.27}$$

Thus, the periods τ_c and τ_θ are related to each other as follows:

$$p_c \tau_c = p_\theta \tau_\theta = \tau_f \tag{3.28}$$

Here p_c and p_θ are the positive whole numbers.

The forced periodic variations of bulk concentration and bulk temperature are imposed according to the following equations, respectively.

$$\begin{aligned} c_{bA}(\tau) &= 1 + \delta_{mA} \sin(\omega_{mA} \tau), \\ \theta_b(\tau) &= 1 + \delta_h \sin(\omega_h \tau) \end{aligned} \tag{3.29}$$

Here, angular frequencies are determined as

$$\omega_{mA} = \frac{2\pi}{\tau_c} = \frac{2\pi p_c}{\tau_f}, \omega_h = \frac{2\pi}{\tau_\theta} = \frac{2\pi p_\theta}{\tau_f}.$$

The ranges of possible values for parameters δ_{mA} and δ_h that are adequate from the point of view of implementation of the process under study are as follows:

$$\begin{aligned} 0 < \delta_{mA} \leqslant 1, \\ 0 < \delta_h \leqslant 0.2. \end{aligned}$$

The forced unsteady-state dimensionless mathematical model of the membrane reactor is given by the following equations.

$$\begin{aligned} \frac{\partial c_A}{\partial \tau} &= \frac{\partial^2 c_A}{\partial z^2} + \left(\frac{1}{\delta + z} - Pe_m\right) \frac{\partial c_A}{\partial z} - \frac{(1-\varepsilon)}{\varepsilon} {\varphi_1}^2 \cdot \exp\left(\gamma_1 \left(1 - \frac{1}{\theta}\right)\right) {c_A}^{p_1} - \frac{Pe_m}{\delta + z} c_A \\ \psi \frac{\partial c_B}{\partial \tau} &= \frac{\partial^2 c_B}{\partial z^2} + \left(\frac{1}{\delta + z} - Pe_m \psi\right) \frac{\partial c_B}{\partial z} + \frac{(1-\varepsilon)}{\varepsilon} {\varphi_1}^2 \psi \cdot \exp\left(\gamma_1 \left(1 - \frac{1}{\theta}\right)\right) {c_A}^{p_1} \\ &\quad - \frac{(1-\varepsilon)}{\varepsilon} {\varphi_2}^2 \zeta \cdot \exp\left(\gamma_2 \left(1 - \frac{1}{\theta}\right)\right) {c_B}^{p_2} - \frac{Pe_m \psi}{\delta + z} c_B \\ \frac{1}{\Omega} \frac{\partial \theta}{\partial \tau} &= \frac{\partial^2 \theta}{\partial z^2} + \left(\frac{1}{\delta + z} - Pe_h\right) \frac{\partial \theta}{\partial z} + {\varphi_1}^2 \beta_1 \cdot \exp\left(\gamma_1 \left(1 - \frac{1}{\theta}\right)\right) {c_A}^{p_1} \\ &\quad + {\varphi_2}^2 \beta_2 \zeta \cdot \exp\left(\gamma_2 \left(1 - \frac{1}{\theta}\right)\right) {c_B}^{p_2} - \frac{Pe_h}{\delta + z} \theta \end{aligned} \tag{3.30}$$

Here, $t_{d,A} = \frac{L^2}{D_{A,\text{eff}}}$ represents the characteristic diffusion time of species *A* in the membrane, $t_{h,A} = \frac{L^2 \rho_m c_{p,m}}{K_{\text{eff}}}$ denotes the characteristic heat conductivity time in the membrane, τ is the

dimensionless time defined as $\tau = \frac{t}{t_{d,A}}$, $\Omega = \frac{t_{d,A}}{t_{h,A}}$ is the ratio of the characteristic diffusion time of species *A* to characteristic heat conductivity time.

The dimensionless boundary conditions for the dimensionless mass and heat balance Eq. (3.30) are defined as follows:

at $z = 0$:

$$\begin{aligned} c_A(\tau) &= 1 + \delta_{mA} \sin(\omega_{mA}\tau), \\ c_B(\tau) &= 0, \\ \theta(\tau) &= 1 + \delta_h sin(\omega_h \tau). \end{aligned} \tag{3.31}$$

at $z = 1$:

$$\frac{\partial c_A}{dz} = \frac{\partial c_B}{dz} = \frac{\partial \theta}{dz} = 0. \tag{3.32}$$

3.2.3 Productivity

The productivity of *A* in a simple reaction where *A* transforms into *P* $(A \rightarrow P)$ is determined by the following equation. It is the difference between the inlet and outlet fluxes by diffusion and convection of the species *A*.

$$J_A(t) = 2\pi\ell\left(-r_{in} D_{A,\text{eff}} \frac{\partial C_A}{\partial r}(r,t)\,|_{r = r_{in}} + r_{in} u_D C_A(r_{in},t) - r_{out} u_D C_A(r_{out},t)\right) \tag{3.33}$$

Similarly, the dimensionless form of the productivity using Eq. (3.33) can be defined as:

$$J_A(\tau) = 2\pi\ell D_{A,\text{eff}}\, \tilde{C}_{bA}\left(-\delta \left.\frac{\partial c_A(z,\tau)}{\partial z}\right|_{z=0} + Pe_m\left(c_A(0,\tau)\delta - c_A(1,\tau)\,(1+\delta)\right)\right) \tag{3.34}$$

Furthermore, in the scenario of a sequential reaction $(A \rightarrow B \rightarrow C)$, the productivity of the desired product *B* is computed using the subsequent equation.

$$J_B(t) = 2\pi\ell\left(-r_{in} D_{B,\text{eff}} \left.\frac{\partial C_B}{\partial r}(r,t)\right|_{r=r_{in}} - r_{out} u_D C_B(r_{out},t)\right) \tag{3.35}$$

The dimensionless representation of Eq. (3.35) is as follows.

$$J_B(\tau) = 2\pi\ell D_{A,\text{eff}}\ \tilde{C}_{bA}\left(-\frac{\delta}{\psi}\frac{\partial c_B}{\partial z}(z,\tau)\Big|_{z=0} - (1+\delta)\,Pe_m\,c_B(1,\tau)\right) \tag{3.36}$$

Here ℓ is the length of the cylinder.

The average productivity is calculated as follows:

$$\tilde{J} = \frac{1}{\tau_f}\int_0^{\tau_f} J(t)\,dt \tag{3.37}$$

The average productivities under forced unsteady-state conditions are represented by $\tilde{J}_{USS}$ while for steady-state conditions, it is $\tilde{J}_{SS}$, (i.e., for $\delta_{mA} = 0$ and $\delta_h = 0$). Subsequently, their ratio can be computed as follows:

$$\Theta = \frac{\tilde{J}_{USS}}{\tilde{J}_{SS}}.$$

Chapter 4 – Numerical Approach

In this chapter, we will develop the numerical solutions for the model equations developed in the previous chapter under both steady and unsteady state conditions. In the case of steady-state conditions, we employ the time-marching scheme to find the steady-state solution, followed by discretization using the modified Crank-Nicolson method. The accuracy of this method is verified by evaluating the absolute maximum error and rate of convergence, supported by the justification of its convergence to the steady-state solution. Furthermore, this section explores the numerical scheme designed to approximate the concentrations and temperature as well as the productivities under unsteady state conditions.

4.1 Numerical schemes for steady-state

To establish the numerical scheme under steady-state conditions, our initial consideration encompasses the scalar linear diffusion-convection-reaction equation. Then, proceeding to construct a time-marching scheme explicitly designed for the scalar equation governing mass balance. Following this, we will extend our approach to develop a time-marching scheme for the coupled nonlinear system involving both mass and heat balance equations. This system pertains to a single reaction characterized by power-law kinetics.

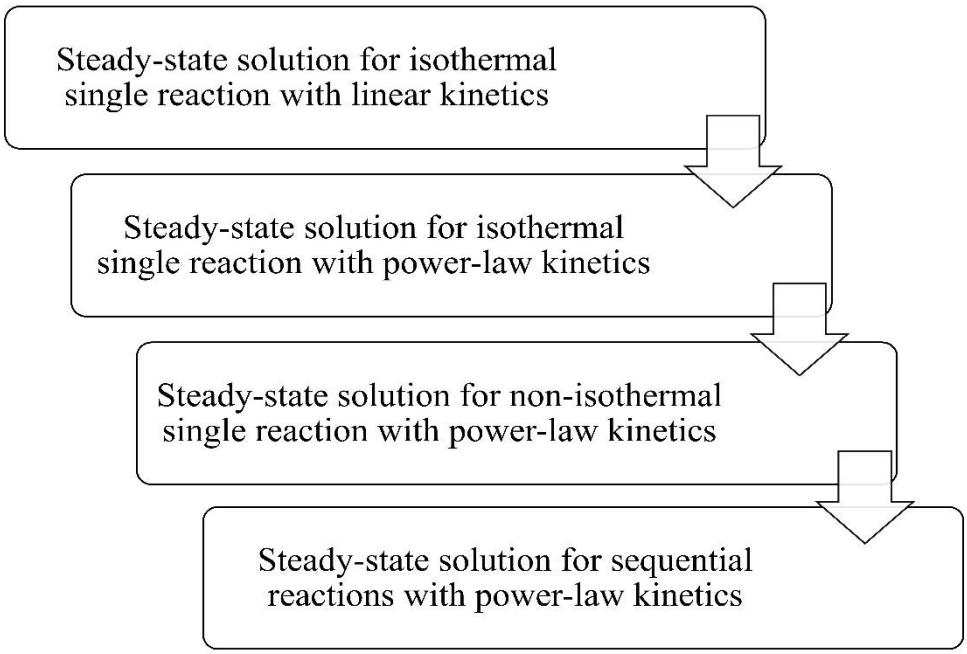

Figure 4.1 Flow diagram illustrating the numerical scheme steps for solving the system of nonlinear differential equations for concentrations and temperature under steady-state

Ultimately, the numerical scheme for the sequential reaction will be presented, incorporating mass and heat balance as described by Eq. (3.17), and subjected to the specified boundary conditions according to Eqs. (3.19) and (3.20) for the reactions with fractional exponents in the cylindrical flow-through catalytic membrane reactor. **Figure 4.1** shows the schematic representation of the numerical scheme steps for solving the system of nonlinear differential equations of concentrations and temperature distribution.

4.1.1 Steady-state solution for isothermal single reaction with linear kinetics

First, the steady-state first-order isothermal reaction is considered, where the component A transforms into P $(A \rightarrow P)$. The corresponding two-point boundary value problem for the mass balance equation reads as follows:

$$\frac{d^2c}{dz^2} + \left(\frac{1}{\delta + z} - Pe_m\right)\frac{dc}{dz} - \left({\varphi_1}^2 + \frac{Pe_m}{\delta + z}\right)c \;=\; 0 \tag{4.1}$$

subject to the boundary conditions

$$c(0) \;=\; 1 \;\text{ and }\; \frac{dc}{dz}(1) \;=\; 0\,. \tag{4.2}$$

The analytic solution to the linear boundary value problem by Eqs. (4.1) and (4.2) can be expressed in terms of Gauss Hypergeometric and Laguerre special functions, and it is given in **Appendix A** by Eq. (A.1).

A spatial equidistant grid $z_0 = 0 < \;\; z_1 < \;\; z_2 < \;\; z_3 < \;\; \ldots \;\; z_N = \;\; 1\,;\; N \in \mathbb{N}$, is used to discretize the scalar Eq. (4.1) subject to the boundary conditions by Eq. (4.2). The mesh size is given by $h = \dfrac{1}{N}$. The diffusion term is discretized through central finite difference, while the backward finite difference is employed for the convection term:

Central finite difference to discretize diffusion term

$$\frac{d^2c}{dz^2} \approx \left(\frac{c(z_{i+1}) - 2c(z_i) + c(z_{i-1})}{h^2}\right), \tag{4.3}$$

Backward finite difference to discretize the convective term

$$\frac{dc}{dz} \approx \left(\frac{c(z_i) - c(z_{i-1})}{h}\right). \tag{4.4}$$

Substituting Eqs. (4.3) and (4.4) into Eq. (4.1) results in

$$\left(\frac{1}{h^2}-\frac{1}{(\delta+z_i)h}+\frac{Pe_m}{h}\right)c_{i-1}+\left(-\frac{2}{h^2}-\frac{1}{(\delta+z_i)h}-\frac{Pe_m}{h}-{\varphi_1}^2-\frac{Pe_m}{\delta+z_i}\right)c_i + \frac{1}{h^2}c_{i+1} \;=\; 0\;, \tag{4.5}$$

where $c_i \approx c(z_i)$. The left boundary condition is employed according to Eq. (4.2), i.e., $c_0 = 1$, and the right boundary is discretized according to finite difference approximation $\frac{c_{N+1}-c_N}{h}=0$ at the outlet. Therefore, the system of linear algebraic equations is obtained for unknown vector $\boldsymbol{c}=[c_{1,}...,c_N]^T$ as follows:

$$\begin{aligned} &B_1c_1+C\,c_2 \;=\; -A_1,\\ &A_ic_{i-1}+B_ic_i+C\,c_{i+1} \;=\; 0, \quad i=2,3,\ldots,N-1,\\ &A_Nc_{N-1}+[B_N+C]\;\;c_N=0, \end{aligned} \tag{4.6}$$

where

$$\begin{aligned} A_i &= \left(\frac{1}{h^2}-\frac{1}{(\delta+z_i)h}+\frac{Pe_m}{h}\right),\\ B_i &= \left(-\frac{2}{h^2}-\frac{1}{(\delta+z_i)h}-\frac{Pe_m}{h}-{\varphi_1}^2-\frac{Pe_m}{\delta+z_i}\right),\\ C &= \frac{1}{h^2}\;. \end{aligned} \tag{4.7}$$

The exact solution given in **Appendix A** by Eq. (A.1) and the numerical solution from Eq. (4.6) are compared in **Figure 4.2** for two distinct sets of Thiele moduli and mass Peclet numbers. Initially, the parameters are maintained at $Pe_m = 1$, $\varphi = 4$, followed by a subsequent evaluation with $Pe_m = 5$, $\varphi = 2.5$. It can be concluded from **Figure 4.2** that the numerical solution coincides with the analytical one.

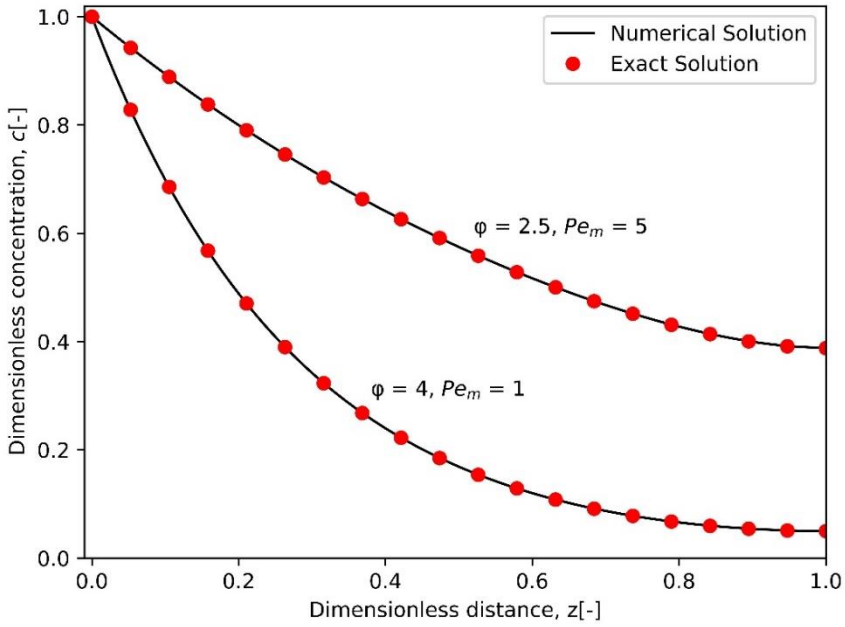

Figure 4.2 Comparing the numerical and exact solutions for two distinct sets of Thiele moduli and mass Peclet numbers, using $p = 1$, and $\delta = 10$.

4.1.2 Steady-state solution for isothermal single reaction with power-law kinetics

Now, the convection-diffusion-reaction equation where *A* transforms into $P(A \rightarrow P)$ under steady-state, isothermal conditions with power-law kinetics is considered. The corresponding mass balance equation is provided as follows:

$$\frac{d^2c}{dz^2} + \left(\frac{1}{\delta + z} - Pe_m\right)\frac{dc}{dz} - {\varphi_1}^2 c^p - \frac{Pe_m}{\delta + z}c = 0\,. \tag{4.8}$$

To determine $c(z)$, we employ the time-marching scheme applied to the non-stationary equation.

$$\frac{\partial \tilde{c}}{\partial t} = \frac{\partial^2 \tilde{c}}{\partial z^2} + \left(\frac{1}{\delta + z} - Pe_m\right)\frac{\partial \tilde{c}}{\partial z} - {\varphi_1}^2 \tilde{c}^p - \frac{Pe_m}{\delta + z}\tilde{c} = 0\,. \tag{4.9}$$

and look for the steady-state limit of the time-dependent solution $\tilde{c}(z,t)$, i.e., $c(z) = \lim_{t\to\infty} \tilde{c}(z,t)$. Equation (4.9) is complemented by boundary and initial conditions as:

$$\begin{aligned} \tilde{c}(0,t) &= 1\,, \quad \frac{d\tilde{c}}{dz}(1,t) = 0\,, \\ \tilde{c}(z,0) &= 1\,. \end{aligned} \tag{4.10}$$

The Crank-Nicolson-based method [50] is used to obtain approximations to $\tilde{c}(z_j, t_n)$ at certain spatial mesh points z_j and discrete times t_n. The method is employed for the discretization of Eq. (4.9). The temporal derivative is discretized as $\frac{c_j^{n+1} - c_j^{n}}{\Delta t}$, while the second and first-order spatial derivatives are discretized as $\frac{1}{2}\left(\frac{c_{j-1}^{n+1} - 2c_j^{n+1} + c_{j+1}^{n+1}}{h^2} + \frac{c_{j-1}^{n} - 2c_j^{n} + c_{j+1}^{n}}{h^2}\right)$ and $\frac{1}{2}\left(\frac{c_j^{n+1} - c_{j-1}^{n+1}}{h} + \frac{c_j^{n} - c_{j-1}^{n}}{h}\right)$.

Furthermore, the terms $\tilde{c}$ and $\tilde{c}^{\,p}$ are discretized as $\frac{1}{2}(c_j^n + c_j^{n+1})$ and $\frac{1}{2}\left((c_j^n)^{\,p} + (c_j^{n+1})^{\,p}\right)$, respectively.

Substituting the aforementioned discretized terms into Eq. (4.9) results in:

$$\begin{aligned}\frac{c_j^{n+1} - c_j^{n}}{\Delta t} = {} & \frac{1}{2h^2} c_{j+1}^{n+1} + \frac{1}{2}\left(\frac{-2}{h^2} + \frac{1}{h}\left(\frac{1}{\delta + z_j} - Pe_m\right) - \frac{Pe_m}{(\delta + z_j)}\right) c_j^{n+1} \\ & + \frac{1}{2}\left(\frac{1}{h^2} - \frac{1}{h}\left(\frac{1}{\delta + z_j} - Pe_m\right)\right) c_{j-1}^{n+1} + \frac{1}{2h^2} c_{j+1}^{n} \\ & + \frac{1}{2}\left(\frac{-2}{h^2} + \frac{1}{h}\left(\frac{1}{\delta + z_j} - Pe_m\right) - \frac{Pe_m}{(\delta + z_j)}\right) c_j^{n} \\ & + \frac{1}{2}\left(\frac{1}{h^2} - \frac{1}{h}\left(\frac{1}{\delta + z_j} - Pe_m\right)\right) c_{j-1}^{n} - \frac{1}{2}\varphi_1^{\,2}\left((c_j^n)^{\,p} + (c_j^{n+1})^{\,p}\right).\end{aligned} \tag{4.11}$$

For j=1, applying the boundary condition at the inlet to the porous medium, we have $c_0^{n+1} = c_0^n = 1$. The Neumann boundary condition at the outlet of the membrane porous medium when $j = N-1$ can be discretized using first-order approximation as $\frac{c_N^n - c_{N-1}^n}{h} = \frac{c_N^{n+1} - c_{N-1}^{n+1}}{h} = 0$.

Let $\mathcal{A} \in \mathbb{R}^{(N-1)\times(N-1)}$ be a square tridiagonal matrix of size $(N-1)\times(N-1)$ be defined as

$$\mathcal{A} = \begin{pmatrix} \alpha_1 & \beta & & & 0 \\ \gamma_2 & \alpha_2 & \beta & & \\ & \ddots & \ddots & \ddots & \\ & & \gamma_{N-2} & \alpha_{N-2} & \beta \\ 0 & & & \gamma_{N-1} & \alpha_{N-1} + \beta \end{pmatrix}, \tag{4.12}$$

where

$$\alpha_j = \frac{-2}{h^2} + \frac{1}{h}\left(\frac{1}{\delta + z_j} - Pe_m\right) - \frac{Pe_m}{(\delta + z_j)} \ ,$$
$$\beta = \frac{1}{h^2} \ , \tag{4.13}$$
$$\gamma_j = \frac{1}{h^2} - \frac{1}{h}\left(\frac{1}{\delta + z_j} - Pe_m\right) .$$

Then, the system of nonlinear algebraic equations for Eq. (4.11) can be written as

$$\frac{\boldsymbol{c}^{n+1} - \boldsymbol{c}^n}{\Delta t} = \frac{1}{2}\boldsymbol{\mathcal{A}}\boldsymbol{c}^{n+1} + \frac{1}{2}\boldsymbol{\mathcal{A}}\boldsymbol{c}^n - \frac{1}{2}{\varphi_1}^2\left((\boldsymbol{c}^n)^{\,p} + (\boldsymbol{c}^{n+1})^{\,p}\right) + \boldsymbol{f}_A , \tag{4.14}$$

where

$$\begin{aligned} \boldsymbol{c}^{n+1} &= [c_1^{n+1}, c_2^{n+1}, \ldots, c_{N-1}^{n+1}]^{\,T} \ , \\ \boldsymbol{c}^{n} &= [c_1^{n}, c_2^{n}, \ldots, c_{N-1}^{n}]^{\,T} \ , \\ \boldsymbol{f}_A &= \left[\frac{1}{h^2} - \frac{1}{h}\left(\frac{1}{\delta + z_1} - Pe_m\right), 0, \ \ldots, 0\right]^{\,T} \ . \end{aligned} \tag{4.15}$$

It is essential to highlight that we ensure the approximate solution's non-negativity at each iteration step to facilitate convergence towards the steady-state limit. For the sake of brevity, the following notation is employed.

$$\boldsymbol{c}^{\,p} = \left[(\max\{c_1, 0\})^{\,p}, (\max\{c_2, 0\})^{\,p}, \ldots, (\max\{c_{N-1}, 0\})^{\,p}\right]^{T} . \tag{4.16}$$

Rearranging Eq. (4.14), the nonlinear algebraic equation for the approximate dimensionless concentration $\boldsymbol{c}^{n+1}$ at each new time step is derived as

$$\boldsymbol{c}^{n+1} = \left(\boldsymbol{I} - \frac{\Delta t}{2}\boldsymbol{\mathcal{A}}\right)^{-1}\left\{\boldsymbol{c}^n + \frac{\Delta t}{2}\boldsymbol{\mathcal{A}}\boldsymbol{c}^n - \frac{\Delta t}{2}{\varphi_1}^2\left((\boldsymbol{c}^n)^{\,p} + (\boldsymbol{c}^{n+1})^{\,p}\right) + \Delta t\boldsymbol{f}_A\right\} . \tag{4.17}$$

The numerical solution of the nonlinear Eq. (4.17) is achieved by applying a few sweeps of fixed-point iteration along with considering only the non-negative part of the concentration in each iteration step [8].

Absolute maximum error and rate of convergence

The absolute maximum error between the numerical solution Eq. (4.17) and the exact solution given in **Appendix A** by Eq. (A.1) at the interior grid points, along with the corresponding convergence rate, are shown in **Table 4.1.** Simulations were performed for

$Pe_m = 1$, $p = 1$, $\varphi = 4$, and $\delta = 10$. The chosen time step was adequately small to ensure that the temporal error remained insignificant when compared to the spatial error.

Table 4.1 The absolute maximum error between numerical and analytical solutions and the rate of convergence

Level i	Error e_i	rate $\log_2\left(\frac{e_i}{e_{i+1}}\right)$
1	7.6802e − 3	
2	1.6561e − 3	2.21335
3	3.9952e − 4	2.05145
4	9.9005e − 5	2.01269
5	2.4699e − 5	2.00305
6	6.6161e − 6	2.00313

4.1.3 Steady-state solution for non-isothermal single reaction with power-law kinetics

In this section, the diffusion-convection-reaction process where *A* transforms into *P* $(A \to P)$ under steady-state, non-isothermal conditions with power-law kinetics is considered. The corresponding mass and heat balance equations are given by

$$\begin{aligned} \frac{d^2 c_A}{dz^2} + \left(\frac{1}{\delta + z} - Pe_m\right)\frac{dc_A}{dz} - {\varphi_1}^2 \cdot \exp\left(\gamma_1\left(1 - \frac{1}{\theta}\right)\right){c_A}^p - \frac{Pe_m}{\delta + z}c_A &= 0 \ , \\ \frac{d^2 \theta}{dz^2} + \left(\frac{1}{\delta + z} - Pe_h\right)\frac{d\theta}{dz} + {\varphi_1}^2 \beta_1 \cdot \exp\left(\gamma_1\left(1 - \frac{1}{\theta}\right)\right){c_A}^p - \frac{Pe_h}{\delta + z}\theta &= 0 \ . \end{aligned} \tag{4.18}$$

Equations (4.18) are complemented by the dimensionless boundary conditions as $c_A(0,t) = 1$, and $\theta(0,t) = 1$ at the membrane's inlet, i.e., $z = 0$. The Neumann boundary conditions are imposed at the outlet of the membrane porous medium $\frac{dc_A}{dz}(1,t) = 0$ and

$\frac{d\theta}{dz}(1,t)=0$ when $z=1$. The initial conditions are defined as $c_A(z,0)=1$, and $\theta(z,0)=1$. The following notations are used.

$$\begin{aligned}
\boldsymbol{c}_A^{n+1} &= [(c_{A,1}^{n+1}, c_{A,2}^{n+1}, \ldots, c_{A,N-1}^{n+1})]^T, \\
\boldsymbol{c}_A^{n} &= [(c_{A,1}^{n}, c_{A,2}^{n}, \ldots, c_{A,N-1}^{n})]^T, \\
\boldsymbol{f}_A &= \left[\left(\frac{1}{h^2} - \frac{1}{h}\left(\frac{1}{\delta + z_1} - Pe_m\right), 0, \ldots, 0\right)\right]^T,
\end{aligned} \tag{4.19}$$

and

$$\begin{aligned}
\boldsymbol{\theta}^{n+1} &= [(\theta_1^{n+1}, \theta_2^{n+1}, \ldots, \theta_{N-1}^{n+1})]^T, \\
\boldsymbol{\theta}^{n} &= [(\theta_1^{n}, \theta_2^{n}, \ldots, \theta_{N-1}^{n})]^T, \\
\boldsymbol{f}_\theta &= \left[\left(\frac{1}{h^2} - \frac{1}{h}\left(\frac{1}{\delta + z_1} - Pe_h\right), 0, \ldots, 0\right)\right]^T.
\end{aligned} \tag{4.20}$$

Then, the system of Eqs. (4.18) is discretized using the modified Crank-Nicolson method. By rearranging the terms, we obtain the system of nonlinear equations for $\boldsymbol{c}_A^{n+1}$ and $\boldsymbol{\theta}^{n+1}$ as follows:

$$\boldsymbol{c}_A^{n+1} = \left(\boldsymbol{I} - \frac{\Delta t}{2}\boldsymbol{\mathcal{A}}\right)^{-1} \left\{ \begin{array}{c} \boldsymbol{c}_A^n + \frac{\Delta t}{2}\boldsymbol{\mathcal{A}}\boldsymbol{c}_A^n \\ -\frac{\Delta t}{2}{\varphi_1}^2 \mathbf{exp}\left(\gamma_1\left(1 - \frac{1}{\boldsymbol{\theta}^n}\right)\right)\left((\boldsymbol{c}_A^{n+1})^p + (\boldsymbol{c}_A^n)^p\right) \\ + \Delta t \boldsymbol{f}_A \end{array} \right\},$$

$$\boldsymbol{\theta}^{n+1} = \left(\boldsymbol{I} - \frac{\Delta t}{2}\boldsymbol{\mathcal{B}}\right)^{-1} \left\{ \begin{array}{c} \boldsymbol{\theta}^n + \frac{\Delta t}{2}\boldsymbol{\mathcal{B}}\boldsymbol{\theta}^n \\ +\frac{\Delta t}{2}{\varphi_1}^2 \beta_1 \left(\mathbf{exp}\left(\gamma_1\left(1 - \frac{1}{\boldsymbol{\theta}^n}\right)\right) + \mathbf{exp}\left(\gamma_1\left(1 - \frac{1}{\boldsymbol{\theta}^{n+1}}\right)\right)\right)(\boldsymbol{c}_A^n)^p \\ + \Delta t \boldsymbol{f}_\theta \end{array} \right\}, \tag{4.21}$$

where $\boldsymbol{I}$ is an identity matrix. $\boldsymbol{\mathcal{A}}$ and $\boldsymbol{\mathcal{B}}$ are square tridiagonal matrices with size $(N-1)\times(N-1)$ defined as

$$\boldsymbol{\mathcal{A}} = \begin{pmatrix} \alpha_1 & \beta & & & 0 \\ \gamma_2 & \alpha_2 & \beta & & \\ & \ddots & \ddots & \ddots & \\ & & \gamma_{N-2} & \alpha_{N-2} & \beta \\ 0 & & & \gamma_{N-1} & \alpha_{N-1}+\beta \end{pmatrix},$$
$$\boldsymbol{\mathcal{B}} = \begin{pmatrix} \omega_1 & \beta & & & 0 \\ \mu_2 & \omega_2 & \beta & & \\ & \ddots & \ddots & \ddots & \\ & & \mu_{N-2} & \omega_{N-2} & \beta \\ 0 & & & \mu_{N-1} & \omega_{N-1}+\beta \end{pmatrix}. \quad (4.22)$$

The entries of the matrices in Eq. (4.22) are given as follows

$$\alpha_j = \frac{-2}{h^2} + \frac{1}{h}\left(\frac{1}{\delta + z_j} - Pe_m\right) - \frac{Pe_m}{\delta + z_j},\ \beta = \frac{1}{h^2},\ \gamma_j = \frac{1}{h^2} - \frac{1}{h}\left(\frac{1}{\delta + z_j} - Pe_m\right), \quad (4.23)$$

$$\omega_j = \frac{-2}{h^2} + \frac{1}{h}\left(\frac{1}{\delta + z_j} - Pe_h\right) - \frac{Pe_h}{\delta + z_j}, \beta = \frac{1}{h^2},\ \mu_j = \frac{1}{h^2} - \frac{1}{h}\left(\frac{1}{\delta + z_j} - Pe_h\right). \quad (4.24)$$

For the sake of brevity, the following notation is employed

$$\mathbf{exp}\left(\gamma_1\left(1 - \frac{1}{\boldsymbol{\theta}^n}\right)\right) = \mathrm{diag}\left[\exp\left(\gamma_1\left(1 - \frac{1}{\boldsymbol{\theta}_1^n}\right)\right), \exp\left(\gamma_1\left(1 - \frac{1}{\boldsymbol{\theta}_2^n}\right)\right), \ldots, \exp\left(\gamma_1\left(1 - \frac{1}{\boldsymbol{\theta}_{N-1}^n}\right)\right)\right]^T$$

The numerical solution at each time step is obtained through fixed-point iteration by using the linear solver provided by the NumPy library in Python [51].

4.1.4 Steady-state solution for sequential reactions with power-law kinetics

The complete system, as described by Eqs. (3.17) for the series reaction, encompasses the equations of mass balances for both components $A,\ B$ along with the equation for heat balance. The instationary system from the previous section is now extended, with the boundary conditions at the inlet of the membrane porous medium as $\tilde{c}_A(0,t) = 1,\ \tilde{c}_B(0,t) = 0,\ \tilde{\theta}(0,t) = 1$. Similarly, the Neumann boundary conditions at the outlet of the membrane porous medium are $\frac{\partial \tilde{c}_A}{\partial z}(1,t) = 0,\ \frac{\partial \tilde{c}_B}{\partial z}(1,t) = 0,\ \frac{\partial \tilde{\theta}}{\partial z}(1,t) = 0.$

The initial conditions are defined as $\tilde{c}_A(z,0) = 1,\ \tilde{c}_B(z,0) = 1,\ \tilde{\theta}(z,0) = 1.$

Employing discretization by the modified Crank-Nicolson method results in the following system of nonlinear algebraic equations for $\boldsymbol{c}_A^{n+1}$, $\boldsymbol{c}_B^{n+1}$ and $\boldsymbol{\theta}^{n+1}$.

$$
\begin{aligned}
\boldsymbol{c}_A^{n+1} &= \left(\boldsymbol{I} - \frac{\Delta t}{2}\boldsymbol{\mathcal{A}}\right)^{-1} \left\{ \begin{array}{c} \boldsymbol{c}_A^n + \frac{\Delta t}{2}\boldsymbol{\mathcal{A}}\boldsymbol{c}_A^n - \frac{\Delta t}{2}{\varphi_1}^2 \mathbf{exp}\left(\gamma_1\left(1-\frac{1}{\boldsymbol{\theta}^n}\right)\right)\left((\boldsymbol{c}_A^{n+1})^{p_1} + (\boldsymbol{c}_A^n)^{p_1}\right) \\ + \Delta t \boldsymbol{f}_A \end{array} \right\}, \\
\boldsymbol{c}_B^{n+1} &= \left(\boldsymbol{I} - \frac{\Delta t}{2}\boldsymbol{\mathcal{M}}\right)^{-1} \left\{ \begin{array}{c} \boldsymbol{c}_B^n + \frac{\Delta t}{2}\boldsymbol{\mathcal{M}}\boldsymbol{c}_B^n + {\varphi_1}^2 \psi \Delta t \cdot \mathbf{exp}\left(\gamma_1\left(1-\frac{1}{\boldsymbol{\theta}^n}\right)\right)(\boldsymbol{c}_A^n)^{p_1} - \\ \frac{\Delta t}{2}{\varphi_2}^2 \zeta \cdot \mathbf{exp}\left(\gamma_2\left(1-\frac{1}{\boldsymbol{\theta}^n}\right)\right)\left((\boldsymbol{c}_B^{n+1})^{p_2} + (\boldsymbol{c}_B^n)^{p_2}\right) + \\ \Delta t \boldsymbol{f}_B \end{array} \right\}, \\
\boldsymbol{\theta}^{n+1} &= \left(\boldsymbol{I} - \frac{\Delta t}{2}\boldsymbol{\mathcal{B}}\right)^{-1} \left\{ \begin{array}{c} \boldsymbol{\theta}^n + \frac{\Delta t}{2}\boldsymbol{\mathcal{B}}\boldsymbol{\theta}^n + \frac{\Delta t}{2}{\varphi_1}^2 \beta_1 \left(\begin{array}{c} \mathbf{exp}\left(\gamma_1\left(1-\frac{1}{\boldsymbol{\theta}^n}\right)\right) + \\ \mathbf{exp}\left(\gamma_1\left(1-\frac{1}{\boldsymbol{\theta}^{n+1}}\right)\right) \end{array} \right)(\boldsymbol{c}_A^n)^{p_1} + \\ \frac{\Delta t}{2}{\varphi_2}^2 \beta_2 \zeta \left(\mathbf{exp}\left(\gamma_2\left(1-\frac{1}{\boldsymbol{\theta}^n}\right)\right) + \mathbf{exp}\left(\gamma_2\left(1-\frac{1}{\boldsymbol{\theta}^{n+1}}\right)\right)\right)(\boldsymbol{c}_B^n)^{p_2} \\ + \Delta t \boldsymbol{f}_\theta \end{array} \right\},
\end{aligned}
\tag{4.25}
$$

where matrices $\boldsymbol{\mathcal{A}}$ and $\boldsymbol{\mathcal{B}}$ are specified by Eq. (4.22) using the entries from Eqs. (4.23) and (4.24). Additionally, the vectors $\boldsymbol{c}_A^{n+1}$, $\boldsymbol{c}_A^n$, $\boldsymbol{f}_A$, $\boldsymbol{\theta}^{n+1}$, $\boldsymbol{\theta}^n$ and $\boldsymbol{f}_\theta$ are also the same as the vectors described by Eqs. (4.19) and (4.20). Similarly, $\boldsymbol{c}_B^{n+1}$, $\boldsymbol{c}_B^n$ and $\boldsymbol{f}_B$ are the vectors which are defined by

$$
\begin{aligned}
\boldsymbol{c}_B^{n+1} &= [\,(c_{B,1}^{n+1}, c_{B,2}^{n+1}, \ldots, c_{B,N-1}^{n+1})\,]^T, \\
\boldsymbol{c}_B^{n} &= [\,(c_{B,1}^{n}, c_{B,2}^{n}, \ldots, c_{B,N-1}^{n})\,]^T, \\
\boldsymbol{f}_B &= \left[\left(\frac{1}{h^2} - \frac{1}{h}\left(\frac{1}{\delta + z_1} - Pe_m \psi\right), 0, \ldots, 0\right)\right]^T.
\end{aligned}
\tag{4.26}
$$

A square tridiagonal matrix $\boldsymbol{\mathcal{M}} \in \mathbb{R}$ with size $(N-1)\times(N-1)$ is defined as

$$
\boldsymbol{\mathcal{M}} = \begin{pmatrix}
m_1 & \beta & & & 0 \\
l_2 & m_2 & \beta & & \\
& \ddots & \ddots & \ddots & \\
& & l_{N-2} & m_{N-2} & \beta \\
0 & & & l_{N-1} & m_{N-1} + \beta
\end{pmatrix}
\tag{4.27}
$$

where the entries of the matrix (4.27) are defined as follows

$$m_j = \frac{-2}{h^2} + \frac{1}{h}\left(\frac{1}{\delta + z_j} - Pe_m\psi\right) - \frac{Pe_m\psi}{\delta + z_j},\ \beta = \frac{1}{h^2},$$
$$l_j = \frac{1}{h^2} - \frac{1}{h}\left(\frac{1}{\delta + z_j} - Pe_m\psi\right). \tag{4.28}$$

The numerical solutions to the nonlinear algebraic system by Eqs. (4.25) are computed at each time step through fixed-point iteration, utilizing the linear solver provided by the NumPy library and the scipy.sparse.diags functions for handling sparse matrices in Python [51]. Numerical results and the analysis of process and model parameters will be presented in the subsequent section.

4.2 Numerical schemes for unsteady state

In order to develop the numerical scheme for unsteady-state conditions, we will follow the same steps undertaken for steady-state conditions. We will first focus on a single reaction under isothermal conditions with power-law kinetics followed by non-isothermal conditions for the single reaction where *A* transforms into product *P*. Subsequently, the numerical scheme for the sequential reaction will be presented, encompassing mass and heat balance given by Eq. (3.30), under the boundary condition according to Eqs. (3.31) and (3.32) in cylindrical flow-through catalytic membrane reactor under unsteady state conditions.

4.2.1 Unsteady-state solution for isothermal single reaction with power-law kinetics

First, we examine the convection-diffusion-reaction equation in which *A* transforms into product *P* ($A \rightarrow P$) under unsteady-state, isothermal conditions characterized by power-law kinetics. The associated mass balance equation is articulated as follows:

$$\frac{\partial c}{\partial \tau} = \frac{\partial^2 c}{\partial z^2} + \left(\frac{1}{\delta + z} - Pe_m\right)\frac{\partial c}{\partial z} - \frac{(1-\varepsilon)}{\varepsilon}{\varphi_1}^2 c^{p_1} - \frac{Pe_m}{\delta + z}c \tag{4.29}$$

Equation (4.29) is subjected to the boundary conditions as follows:

$$c(0,\tau) = 1 + \delta_{mA}\sin(\omega_{mA}\tau),$$
$$\frac{\partial c}{dz}(1,\tau) = 0 \tag{4.30}$$

The initial conditions are defined as:

$$c(z,0) \;=\; 1\,. \tag{4.31}$$

The Crank-Nicolson-based method is used to obtain approximations to $c\,(z_j,\tau_n)$. The method is employed for the discretization of Eqs. (4.29) and (4.30) with respect to time followed by finite difference approximation in space as we did previously. After substituting discretized terms into Eq. (4.29), we get

$$\begin{aligned}\left(\frac{c_j^{\,n+1}-c_j^{\,n}}{\Delta\tau}\right) &= \frac{1}{2h^2}c_{j+1}^{n+1}+\frac{1}{2}\left(\frac{-2}{h^2}+\frac{1}{h}\left(\frac{1}{\delta+z_j}-Pe_m\right)-\frac{Pe_m}{(\delta+z_j)}\right)c_j^{n+1}\\ &\quad+\frac{1}{2}\left(\frac{1}{h^2}-\frac{1}{h}\left(\frac{1}{\delta+z_j}-Pe_m\right)\right)c_{j-1}^{n+1}+\frac{1}{2h^2}c_{j+1}^{n}\\ &\quad+\frac{1}{2}\left(\frac{-2}{h^2}+\frac{1}{h}\left(\frac{1}{\delta+z_j}-Pe_m\right)-\frac{Pe_m}{(\delta+z_j)}\right)c_j^{n}\\ &\quad+\frac{1}{2}\left(\frac{1}{h^2}-\frac{1}{h}\left(\frac{1}{\delta+z_j}-Pe_m\right)\right)c_{j-1}^{n}-\frac{1}{2}\frac{(1-\varepsilon)}{\varepsilon}{\varphi_1}^2\left((c_j^{n})^{\,p}+(c_j^{n+1})^{\,p}\right)\,.\end{aligned} \tag{4.32}$$

Applying the boundary condition at the inlet to the porous medium for $j=1$, we get $c_0^{n+1}=c_0^n=1+\delta_{mA}\sin(\omega_{mA}\tau)$. Utilizing a first-order approximation, i.e., $\frac{c_N^n-c_{N-1}^n}{h}=\frac{c_N^{n+1}-c_{N-1}^{n+1}}{h}=0$ enables the discretization of the Neumann boundary conditions at the outlet of the membrane porous medium when $j=N-1$.

Let $\boldsymbol{\mathcal{A}}\in\mathbb{R}^{(N-1)\times(N-1)}$ be a square tridiagonal matrix of size $(N-1)\times(N-1)$ defined by Eq. (4.12) where its entries are defined by Eq. (4.13).

Then, the system of nonlinear algebraic equations for Eq. (4.32) can be articulated as

$$\left(\frac{\boldsymbol{c}^{\,n+1}-\boldsymbol{c}^{\,n}}{\Delta\tau}\right)=\frac{1}{2}\boldsymbol{\mathcal{A}}\boldsymbol{c}^{\,n+1}+\frac{1}{2}\boldsymbol{\mathcal{A}}\boldsymbol{c}^{\,n}-\frac{(1-\varepsilon)}{2\varepsilon}{\varphi_1}^2\left((\boldsymbol{c}^{\,n})^{\,p}+(\boldsymbol{c}^{\,n+1})^{\,p}\right)+\frac{1}{2}\left(\boldsymbol{f}_A\cdot u_a\right) \tag{4.33}$$

where

$$\begin{aligned}u_a &= \left((1+\delta_{mA}\sin(\omega_{mA}\tau_n))+(1+\delta_{mA}\sin(\omega_{mA}\tau_{n+1}))\right),\\ \boldsymbol{f}_A\cdot u_a &= \left[\left(\frac{1}{h^2}-\frac{1}{h}\left(\frac{1}{\delta+z_1}-Pe_m\right)\right)\begin{pmatrix}(1+\delta_{mA}\sin(\omega_{mA}\tau_n))+\\(1+\delta_{mA}\sin(\omega_{mA}\tau_{n+1}))\end{pmatrix},0,\ldots,0\right]^T\end{aligned} \tag{4.34}$$

Rearranging Eq. (4.33), the nonlinear algebraic equation for the approximate dimensionless concentration $\boldsymbol{c}^{n+1}$ at each new time step is derived as

$$\boldsymbol{c}^{n+1}=\left(\boldsymbol{I}-\frac{\Delta\tau}{2}\boldsymbol{\mathcal{A}}\right)^{-1}\left\{\boldsymbol{c}^{n}+\frac{\Delta\tau}{2}\boldsymbol{\mathcal{A}}\boldsymbol{c}^{n}-\frac{(1-\varepsilon)\Delta\tau}{2\varepsilon}\varphi_1{}^{2}\left((\boldsymbol{c}^{n})^{p}+(\boldsymbol{c}^{n+1})^{p}\right)+\frac{\Delta\tau}{2}(\boldsymbol{f}_A\cdot u_a)\right\} \tag{4.35}$$

The comparison of the concentration profile between the previous steady-state solution according to Eq. (4.17) and the current forced unsteady state solution Eq. (4.35) in the case of a single reaction under isothermal conditions is shown in **Figure 4.3**. This observation indicates that as the value of δ_{mA} approaches zero, both steady and unsteady-state solutions converge and align on the same line. The Root Mean Square Error (RMSE) and Maximum Absolute Difference (MAD) for this scenario are computed and presented in **Table 4.2**. The values of RMSE and MAD suggest a negligible discrepancy between our steady-state and unsteady-state concentration solutions. In other words, it means a high degree of similarity between the two solutions. The numerical simulations were conducted by keeping the parameters as follows: $Pe_m=1$, $\varphi=1.5$, $\varepsilon=0.6$, $p=0.5$, $\delta=10$, $\omega_{mA}=1$ and $\delta_{mA}=1e^{-5}$.

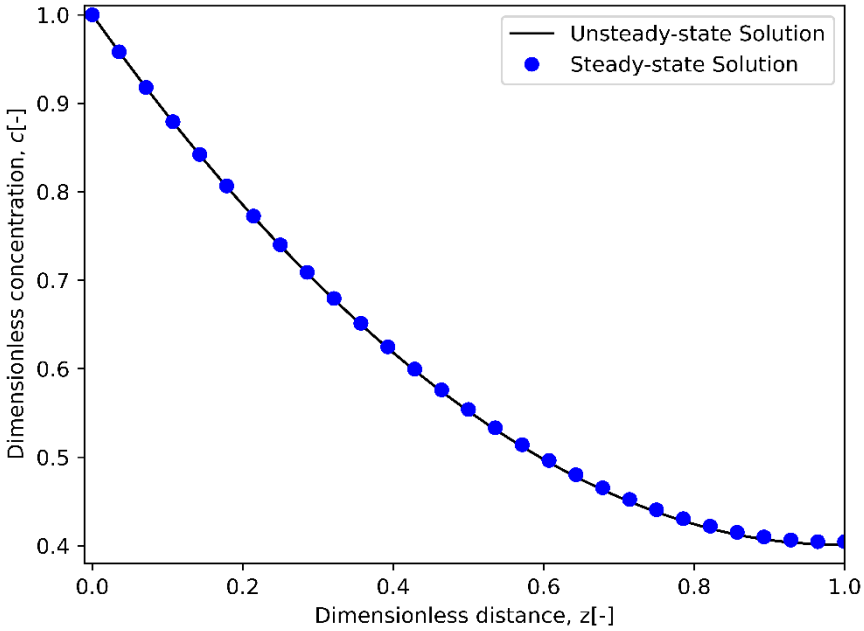

Figure 4.3 Comparing steady and unsteady-state concentration profile for $Pe_m=1$, $\varphi=1.5$, $\varepsilon=0.6$, $p=0.5$, $\delta=10$, $\omega_{mA}=1$ and $\delta_{mA}=1e^{-5}$.

Table 4.2 The Root Mean Square Error and Maximum Absolute Difference for the concentration solutions for steady and unsteady-state conditions

Property	Value
Root Mean Square Error (RMSE)	5.698×10^{-6}
Maximum Absolute Difference (MAD)	8.442×10^{-6}

4.2.2 Unsteady-state solution for non-isothermal single reaction with power-law kinetics

We will now proceed to the diffusion-convection-reaction process where reactant *A* transforms into product *P* $(A \rightarrow P)$ under unsteady-state, non-isothermal conditions characterized by power law-kinetics. The associated mass and heat balance equations are expressed as follows:

$$\frac{\partial c_A}{\partial \tau} = \frac{\partial^2 c_A}{dz^2} + \left(\frac{1}{\delta + z} - Pe_m\right)\frac{\partial c_A}{\partial z} - \frac{(1-\varepsilon)}{\varepsilon}{\varphi_1}^2 \cdot \exp\left(\gamma_1\left(1 - \frac{1}{\theta}\right)\right){c_A}^p - \frac{Pe_m}{\delta + z}c_A = 0 ,$$

$$\frac{1}{\Omega}\frac{\partial \theta}{\partial \tau} = \frac{\partial^2 \theta}{\partial z^2} + \left(\frac{1}{\delta + z} - Pe_h\right)\frac{\partial \theta}{\partial z} + {\varphi_1}^2 \beta_1 \cdot \exp\left(\gamma_1\left(1 - \frac{1}{\theta}\right)\right){c_A}^p - \frac{Pe_h}{\delta + z}\theta = 0 . \tag{4.36}$$

The dimensionless boundary conditions for Eqs. (4.36) are $c_A(0,\tau) = 1 + \delta_{mA}\sin(\omega_{mA}\tau)$, $\theta(0,\tau) = 1 + \delta_h \sin(\omega_h \tau)$ at the inlet of the porous medium, i.e., $z = 0$. Similarly, at the outlet of the membrane porous medium when $z = 1$, Neumann boundary conditions are imposed, i.e., $\frac{\partial c_A}{\partial z}(1,\tau) = 0$ and $\frac{\partial \theta}{\partial z}(1,\tau) = 0$. The notations employed here are similar to those previously defined in Eqs. (4.19) and (4.20)

Then, the system of Eqs. (4.36) is discretized using the modified Crank-Nicolson method. By rearranging the terms, the system of nonlinear equations for $\boldsymbol{c}_A^{n+1}$ and $\boldsymbol{\theta}^{n+1}$ under unsteady state conditions is obtained as follows:

$$\boldsymbol{c}_A^{n+1}=\left(\boldsymbol{I}-\frac{\Delta\tau}{2}\boldsymbol{\mathcal{A}}\right)^{-1}\left\{\begin{array}{c}\boldsymbol{c}_A^n+\frac{\Delta\tau}{2}\boldsymbol{\mathcal{A}}\boldsymbol{c}_A^n\\ -\frac{(1-\varepsilon)\Delta\tau}{2\varepsilon}{\varphi_1}^2\mathbf{exp}\left(\gamma_1\left(1-\frac{1}{\boldsymbol{\theta}^n}\right)\right)\left((\boldsymbol{c}_A^{n+1})^{\,p}+(\boldsymbol{c}_A^n)^{\,p}\right)\\ +\frac{\Delta\tau}{2}(\boldsymbol{f}_A\cdot u_a)\end{array}\right\},$$

$$\boldsymbol{\theta}^{n+1}=\left(\boldsymbol{I}-\frac{\Omega}{2}\Delta\tau\boldsymbol{\mathcal{B}}\right)^{-1}\left\{\begin{array}{c}\boldsymbol{\theta}^n+\frac{\Omega}{2}\Delta\tau\boldsymbol{\mathcal{B}}\boldsymbol{\theta}^n\\ +\frac{\Omega}{2}\Delta\tau{\varphi_1}^2\beta_1\left(\mathbf{exp}\left(\gamma_1\left(1-\frac{1}{\boldsymbol{\theta}^n}\right)\right)+\mathbf{exp}\left(\gamma_1\left(1-\frac{1}{\boldsymbol{\theta}^{n+1}}\right)\right)\right)(\boldsymbol{c}_A^n)^{\,p}\\ +\frac{\Omega}{2}\Delta\tau(\boldsymbol{f}_\theta\cdot u_\theta)\end{array}\right\},\tag{4.37}$$

where u_a and $\boldsymbol{f}_A$ are defined by Eq. (4.34). The terms in the temperature equation are defined as follows:

$$\begin{aligned}u_\theta&=\left((1+\delta_h\sin(\omega_h\tau_n))+(1+\delta_h\sin(\omega_h\tau_{n+1}))\right)\\ \boldsymbol{f}_\theta\cdot u_\theta&=\left[\left(\frac{1}{h^2}-\frac{1}{h}\left(\frac{1}{\delta+z_1}-Pe_h\right)\right)\begin{pmatrix}(1+\delta_h\sin(\omega_h\tau_n))+\\ (1+\delta_h\sin(\omega_h\tau_{n+1}))\end{pmatrix},0,\ldots,0\right]^T\end{aligned}\tag{4.38}$$

Here $\boldsymbol{I}$ is an identity matrix. $\boldsymbol{\mathcal{A}}$ and $\boldsymbol{\mathcal{B}}$ are square tridiagonal matrices defined by Eq. (4.22) with size $(N-1)\times(N-1)$, whereas their entries are defined by Eqs. (4.23) and (4.24) respectively. Similarly, the notations used in Eq. (4.37) are defined by Eq. (4.19) and (4.20).

4.2.3 Unsteady-state solution for sequential reactions with power-law kinetics

Our complete system under unsteady-state conditions, as articulated in Eq. (3.30), for series reaction, comprises the equations of mass balances for both components A and B as well as the equation for heat balance. The system of equations under unsteady-state conditions from the previous section is now extended, with the boundary conditions at the inlet of the

membrane porous medium as $c_A(0,\tau)=1+\delta_{mA}\sin(\omega_{mA}\tau)$, $c_B(0,\tau)=0$, $\theta(0,\tau)=1+\delta_h\sin(\omega_h\tau)$. The boundary conditions at the outlet of the membrane porous medium are $\frac{\partial c_A}{\partial z}(1,\tau)=0$, $\frac{\partial c_B}{\partial z}(1,\tau)=0$, and $\frac{\partial \theta}{\partial z}(1,\tau)=0$.

Then, the system of Eqs. (3.30) is discretized using the modified Crank-Nicolson method. By rearranging the terms, the system of nonlinear equations for $\boldsymbol{c}_A^{n+1}$, $\boldsymbol{c}_B^{n+1}$ and $\boldsymbol{\theta}^{n+1}$ under unsteady state conditions is obtained as follows:

$$\boldsymbol{c}_A^{n+1}=\left(\boldsymbol{I}-\frac{\Delta\tau}{2}\boldsymbol{\mathcal{A}}\right)^{-1}\left\{\begin{array}{c}\boldsymbol{c}_A^n+\frac{\Delta\tau}{2}\boldsymbol{\mathcal{A}}\boldsymbol{c}_A^n\\ -\frac{(1-\varepsilon)\Delta\tau}{2\varepsilon}{\varphi_1}^2\mathbf{exp}\left(\gamma_1\left(1-\frac{1}{\boldsymbol{\theta}^n}\right)\right)\left((\boldsymbol{c}_A^{n+1})^{\,p}+(\boldsymbol{c}_A^n)^{\,p}\right)\\ +\frac{\Delta\tau}{2}(\boldsymbol{f}_A\cdot u_a)\end{array}\right\},$$

$$\boldsymbol{c}_B^{n+1}=\left(\boldsymbol{I}-\frac{\Delta\tau}{2\psi}\boldsymbol{\mathcal{M}}\right)^{-1}\left\{\begin{array}{c}\boldsymbol{c}_B^n+\frac{\Delta\tau}{2\psi}\boldsymbol{\mathcal{M}}\boldsymbol{c}_B^n+\frac{(1-\varepsilon)\Delta\tau}{2\psi\varepsilon}{\varphi_1}^2\cdot\mathbf{exp}\left(\gamma_1\left(1-\frac{1}{\boldsymbol{\theta}^n}\right)\right)(\boldsymbol{c}_A^n)^{\,p_1}-\\ \frac{(1-\varepsilon)\Delta\tau}{2\psi\varepsilon}{\varphi_2}^2\zeta\cdot\mathbf{exp}\left(\gamma_2\left(1-\frac{1}{\boldsymbol{\theta}^n}\right)\right)\left((\boldsymbol{c}_B^{n+1})^{\,p_2}+(\boldsymbol{c}_B^n)^{\,p_2}\right)+\\ \frac{\Delta\tau}{2\psi}\boldsymbol{f}_B\end{array}\right\},$$

$$\boldsymbol{\theta}^{n+1}=\left(\boldsymbol{I}-\frac{\Omega}{2}\Delta\tau\boldsymbol{\mathcal{B}}\right)^{-1}\left\{\begin{array}{c}\boldsymbol{\theta}^n+\frac{\Omega}{2}\Delta\tau\boldsymbol{\mathcal{B}}\boldsymbol{\theta}^n+\frac{\Omega}{2}\Delta\tau{\varphi_1}^2\beta_1\left(\begin{array}{c}\mathbf{exp}\left(\gamma_1\left(1-\frac{1}{\boldsymbol{\theta}^n}\right)\right)+\\ \mathbf{exp}\left(\gamma_1\left(1-\frac{1}{\boldsymbol{\theta}^{n+1}}\right)\right)\end{array}\right)(\boldsymbol{c}_A^n)^{\,p_1}+\\ \frac{\Omega}{2}\Delta\tau{\varphi_2}^2\beta_2\zeta\left(\begin{array}{c}\mathbf{exp}\left(\gamma_2\left(1-\frac{1}{\boldsymbol{\theta}^n}\right)\right)+\\ \mathbf{exp}\left(\gamma_2\left(1-\frac{1}{\boldsymbol{\theta}^{n+1}}\right)\right)\end{array}\right)(\boldsymbol{c}_B^n)^{\,p_2}+\frac{\Omega}{2}\Delta\tau(\boldsymbol{f}_\theta\cdot u_\theta)\end{array}\right\},$$

(4.39)

where matrices $\boldsymbol{\mathcal{A}}$, $\boldsymbol{\mathcal{B}}$ and $\boldsymbol{\mathcal{M}}$ are specified by Eqs. (4.22) and (4.27) using the entries from Eqs. (4.23), (4.24) and (4.28) respectively.

Additionally, the vectors $\boldsymbol{c}_A^{n+1}$, $\boldsymbol{c}_A^n$, $\boldsymbol{f}_A$, $\boldsymbol{c}_B^{n+1}$, $\boldsymbol{c}_B^n$, $\boldsymbol{f}_B$, $\boldsymbol{\theta}^{n+1}$, $\boldsymbol{\theta}^n$ and $\boldsymbol{f}_\theta$ are also the same as the vectors described by Eqs. (4.19), (4.26) and (4.20) respectively.

Chapter 5 – Simulation Results and Discussion

This section presents a comprehensive discussion of the results obtained under both steady-state and unsteady-state conditions. The initial focus is placed on exploring steady-state conditions, involving a comparative analysis between our recently formulated cylindrical geometry model and the previously developed planar geometry model. Subsequently, the impact of various process and model parameters on concentration and temperature profiles is explored within the steady-state condition. Furthermore, we will extend our investigation to concentration and temperature profiles, alongside productivity, under unsteady-state conditions.

5.1 Steady-state condition

5.1.1 Comparison of planar and cylindrical geometries

This section provides a comprehensive comparison between simulation results obtained using our cylindrical model and those from the previously developed planar model [8]

Comparison at large values of geometry parameter δ

Figure 5.1 shows the concentration profile for both the planar and cylindrical models when the value of δ approaches infinity.

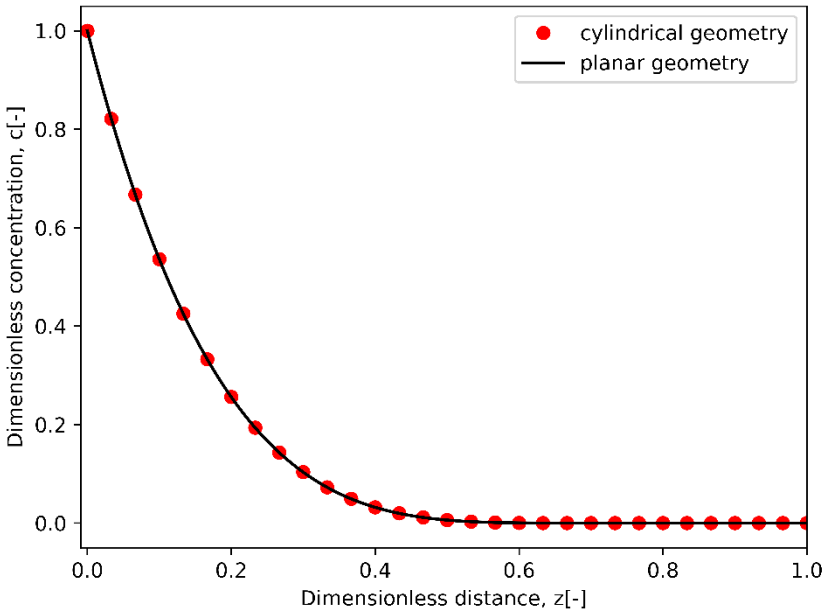

Figure 5.1 Dead-core solutions for planar and cylindrical geometry models for $\varphi = 5$, $p = 0.5, \delta = 10^8$ and $Pe_m = 0$ (no convection).

Figure 5.1 demonstrates that as the value of δ approaches large values, particularly 10^8 for this investigation, a significant result unfolds: the dead core solutions for both planar and our cylindrical geometries from Eq. (4.8) coincide. This notable alignment not only highlights the convergence of solutions but also serves as a clear indication of the accuracy of our model. The simulation was performed using specific parameter values: $\varphi = 5$, $p = 0.5$, and $Pe_m = 0$.

Impact of δ on the concentration profiles

Figure 5.2 shows the impact of δ on profiles of dead core solutions within the cylindrical membrane reactor. The graph shows variations in the dead zones when δ assumes various values. Significantly, the dead core solutions of both planar and cylindrical models align along the same line as the δ approaches infinity, affirming the theoretical expectations stated in the preceding section.

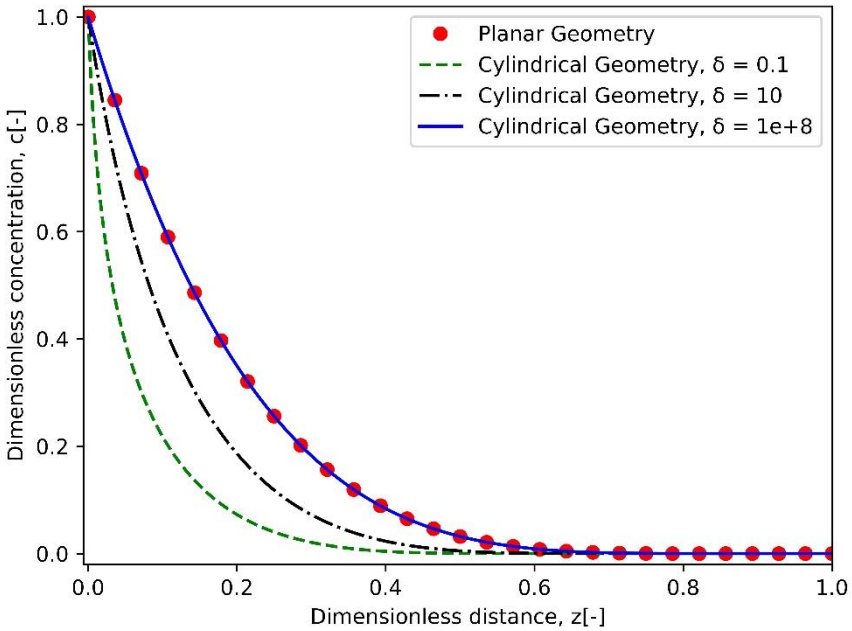

Figure 5.2 Effect of δ on dead core solutions in cylindrical geometry model, validated against planar geometry as δ approaches infinity for $\varphi = 4$, $p = 0.5$, and $Pe_m = 0$ (no convection).

When the value of δ is set to a lower level, i.e. $\delta = 0.1$, the larger dead zone appears, as evidenced by **Figure 5.2**. This phenomenon can be attributed to the inverse relationship between the δ value and the membrane thickness. A smaller δ value correlates to a greater membrane thickness, hence increasing the diffusion distance. The increased distance over

which diffusion occurs leads to more mass transfer limitations, resulting in the formation of a larger dead zone. As the δ values increase, the dead zone progressively shifts away due to lower mass transfer limitations. The cylindrical model solution eventually aligns with the solution of the planar geometry at a sufficiently large delta, specifically when $\delta = 10^8$, as expected. The simulations were conducted for the following parameter values $\varphi = 4$, $p = 0.5$ and $Pe_m = 0$ (no convection).

5.1.2 Effect of process and model parameters

Steady-state isothermal conditions for a single reaction

We will begin by examining the convection-diffusion-reaction problem of Eqs. (4.8) and (4.10), where *A* transforms into *P* $(A \rightarrow P)$ under steady-state, isothermal conditions with power-law kinetics. The effect of various parameters on the concentration profile of reactant *A* is discussed in the subsequent sections.

Effect of Thiele modulus

The Thiele modulus is a main factor in determining the dead zone length. Prior knowledge of the dead zone's location is crucial to prevent inefficient use of costly catalysts.

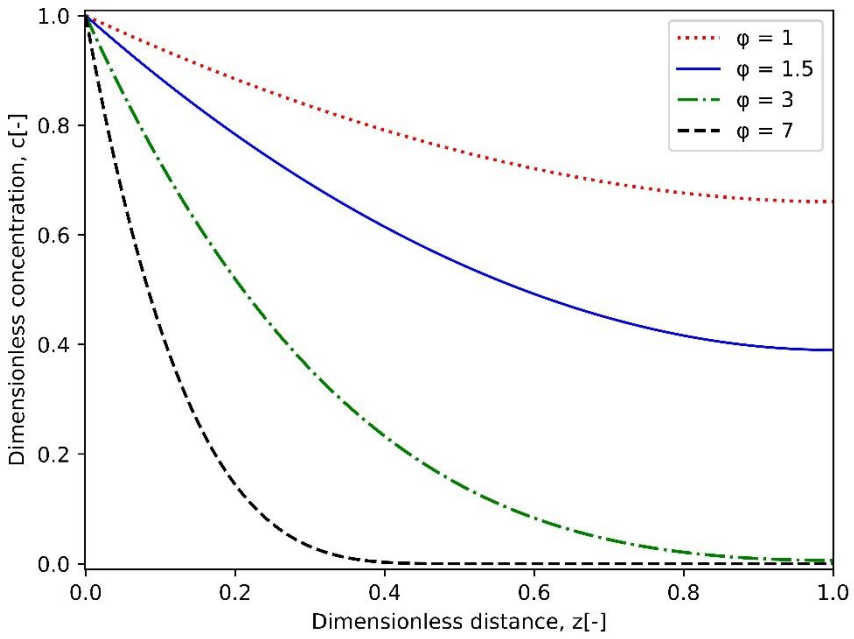

Figure 5.3 Impact of Thiele modulus on the concentration profile of reactant A with dead core and non-dead-core solutions under isothermal conditions for $Pe_m = 1$, $p = 0.5$, and $\delta = 10$.

Figure 5.3 illustrates the impact of the Thiele modulus on the concentration profile of reactant *A* in a single isothermal reaction. The graph shows how the concentration profile changes with varying Thiele Modulus. At lower Thiele modulus values, the concentration distribution appears nearly uniform, signifying a gradual decrease in the concentration of reactant *A*.

As the Thiele modulus increases, a dead core is formed, as shown in **Figure 5.3**. The length of this dead zone grows as the value of the Thiele modulus increases. The dead core profiles suggest that the reaction does not sufficiently propagate to the end of the porous region. Notably, dead cores are observed at $\varphi = 3$ and 7, but vanish as the value of Thiele modulus reduces, i.e., $\varphi = 1$ and 1.5. The disappearance of the dead zone for decreasing Thiele modulus value can be attributed to an interaction between more efficient mass transfer and reaction kinetics. Mass transfer limitations become less pronounced when the Thiele modulus is reduced to a lower value, facilitating a more uniform reaction across the porous membrane.

Effect of reaction exponent at different ***δ*** *values*

Figure 5.4 illustrates the effect of reaction exponent with four distinct plots corresponding to various reaction exponent values: $p = 0.1, 0.5, 1,$ and 1.5. The simulations were performed for $Pe_m = 1$, $\varphi = 3$, and $\delta = 0.5$.

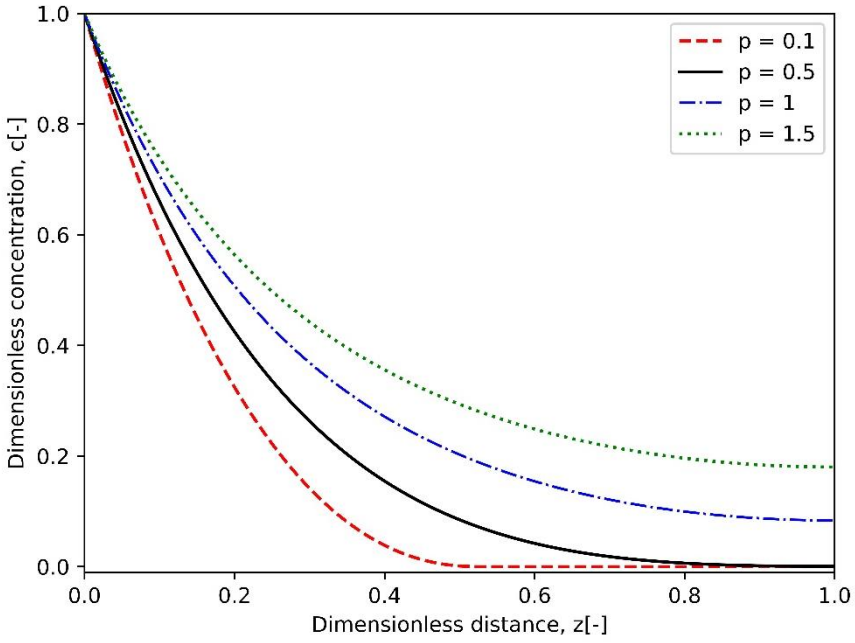

Figure 5.4 Impact of reaction exponent on the concentration profile of reactant A in a single reaction for $\boldsymbol{Pe_m = 1, \varphi = 3, \delta = 0.5}$.

It can be observed that dead zones occur for lower values of the reaction exponent $(p = 0.1 \text{ and } 0.5)$. The phenomena can be explained by the stronger reactions at lower fractional reaction exponents such that the reaction ceases due to mass transfer limitations in some regions of the porous space. As a result, this leads to the formation of dead zones, where the concentration of reactant *A* vanishes and the reaction ceases.

The absence of dead zones at higher reaction exponents can be attributed to a more effective interaction between reaction kinetics and mass transfer. At higher reaction exponents, the mass transfer limitations are not profound, preventing the formation of dead zones. The catalyst is used across the whole membrane in this case, leading to more uniform concentration profiles.

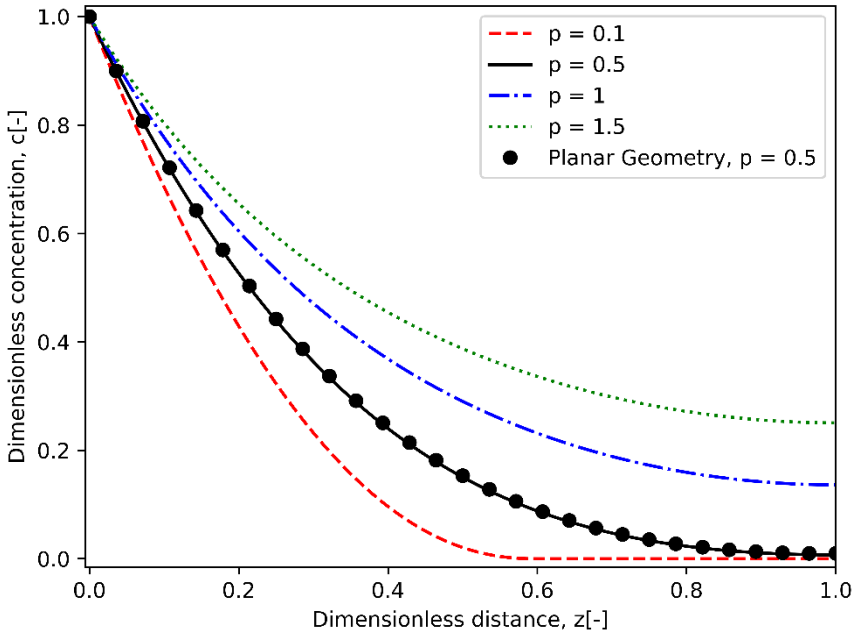

Figure 5.5 Impact of reaction exponent on the concentration profile of reactant A in a single reaction for $Pe_m = 1, \varphi = 3, \delta = 10^8$.

Similarly, when the value of δ approaches infinity, particularly $1e+8$ as in this case, then both planar and cylindrical solutions coincide, as illustrated in **Figure 5.5**.

Steady-state non-isothermal conditions for single reaction

In this section, we will extend our investigation to the diffusion-convection-reaction problem described by Eqs. (4.18) under steady-state and non-isothermal conditions with power-law kinetics.

Effect of Thiele modulus

Figure 5.6 illustrates the effect of Thiele modulus on the steady-state solution profiles for concentration and temperature under non-isothermal conditions for a single reaction. In order to obtain the dead-core solution, the value of φ_1 is set to 4. The numerical simulations were performed by keeping $Pe_m = Pe_h = 1, p = 0.5, \gamma_1 = 5, \beta_1 = 0.1,$ and $\delta = 10$.

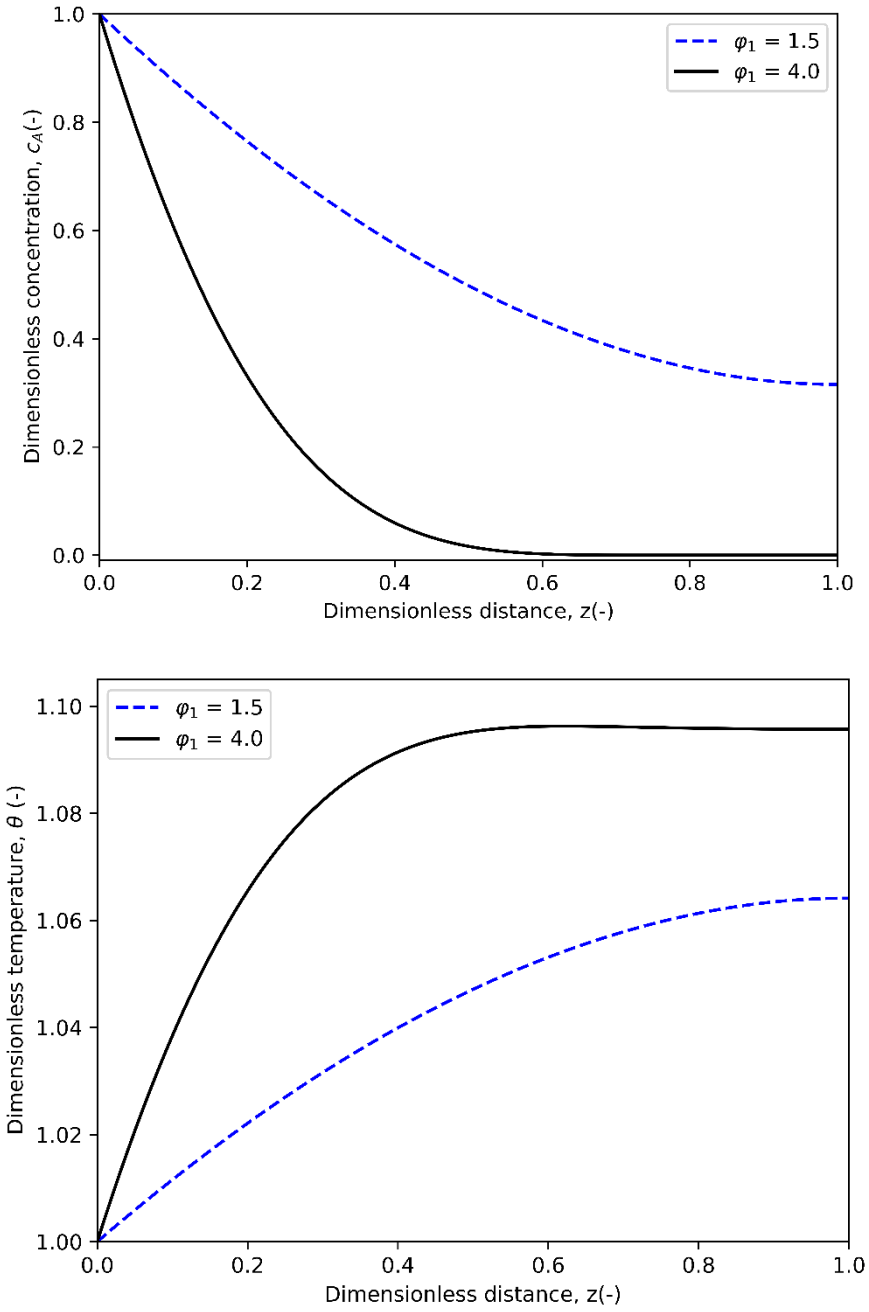

Figure 5.6 Solution profiles for the (a) concentration and (b) temperature for both dead-core and without dead-core for $Pe_m = Pe_h = 1, p = 0.5, \gamma_1 = 5, \beta_1 = 0.1,$ and $\delta = 10$.

Effect of Prater number (energy generation function)

Figure 5.7 illustrates the impact of Prater number on the dimensionless concentration and temperature profiles. The case of $\beta_1 < 0$ corresponds to an endothermic reaction with the value of $\theta < 1$. While, $\beta_1 > 0$ indicates an exothermic reaction, where $\theta > 1$

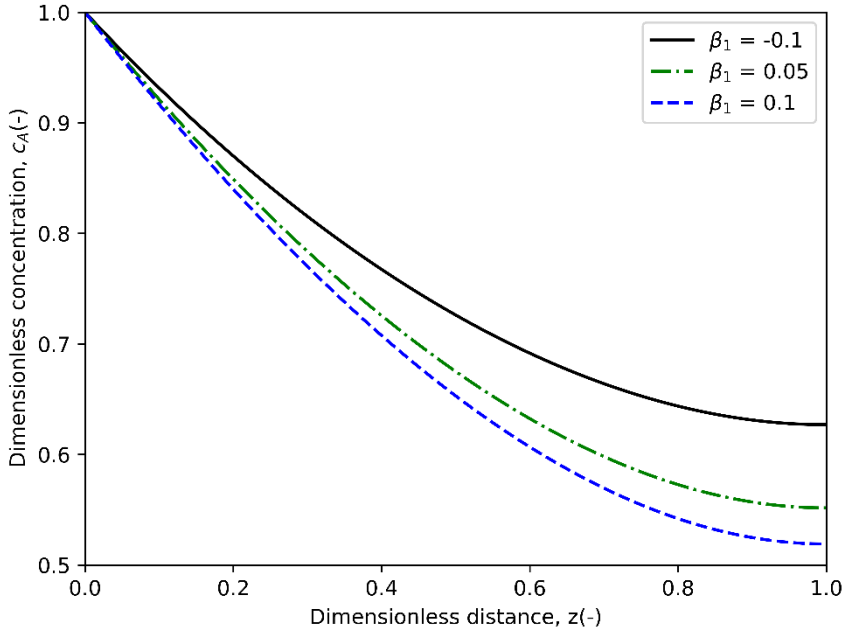

(a)

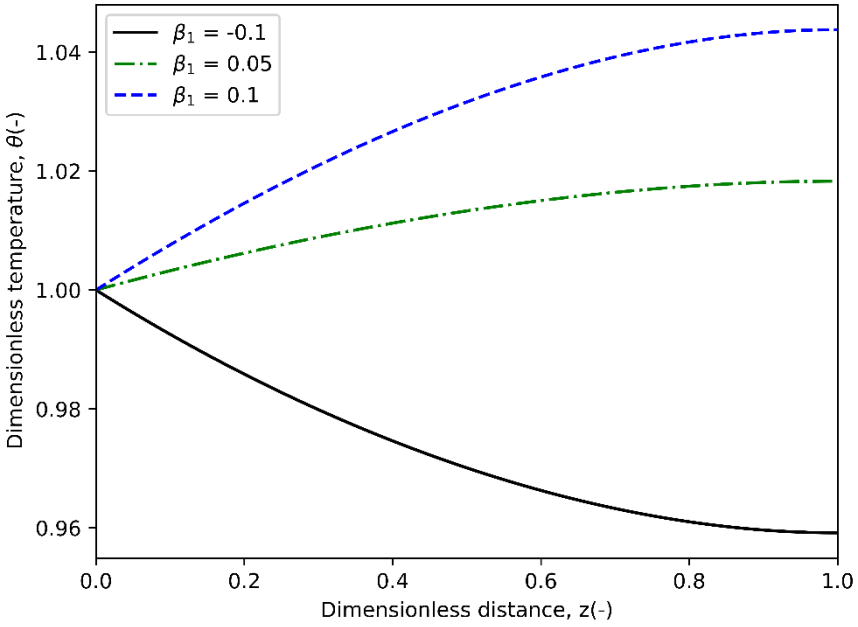

(b)

Figure 5.7 Impact of Prater number on solution profiles of (a) concentration and (b) temperature for $Pe_m = Pe_h = 1, p = 0.5,\ \gamma_1 = 5,\ \varphi_1 = 1.2,$ and $\delta = 10$.

Concurrently, as the value of β_1 increases, the temperature of the system rises as more heat is released due to the reaction, resulting in an enhanced rate of reaction. This phenomenon could be attributed to the temperature-dependent nature of the Arrhenius rate constant. In other words, this results in greater consumption of reactant *A* as the value of β_1 progressively increases, as shown in **Figure 5.7 (a)**.

Effect of geometry parameter (***δ***)

Figure 5.8 illustrates the impact of the model parameter (geometry parameter δ) on the dimensionless concentration and temperature profiles without dead-core. As the value of δ increases, there is a corresponding decrease in the consumption of reactant *A*. This phenomenon can be attributed to the term $\left(\frac{Pe_m}{\delta + z}\right)c_A$ in Eq. (4.18), where, at lower δ values, this term is more dominant, resulting in an increased consumption of reactant *A*. Conversely, as the value of δ increases, the influence of this term decreases, leading to a lower consumption of our reactant *A*, as depicted in **Figure 5.8 (a)**. The numerical simulations were performed for the following parameters: $Pe_m = 1$, $Pe_h = 1$, $p = 0.5$, $\varphi_1 = 1.2$, $\gamma_1 = 5$, and $\beta_1 = 0.1$.

The temperature profile is similarly influenced by the term $\left(\frac{Pe_h}{\delta + z}\right)\theta$ in Eq. (4.18). At the lower value of δ, this term becomes more prominent, resulting in a decrease in the temperature of the porous membrane system. In other words, this decrease in temperature can be justified due to the cooling effect facilitated by convective heat transfer $(Pe_h > 0)$. In the present model of a cylindrical membrane reactor, the cooling phenomena dominate over the heat released by the exothermic reaction, leading to a decrease in temperature within the membrane. Notably, these effects have not been presented in the case of the planar geometry model.

On the contrary, as the value of δ increases, the influence of this term diminishes significantly, resulting in a nearly uniform temperature within the membrane, as shown in **Figure 5.8 (b)**.

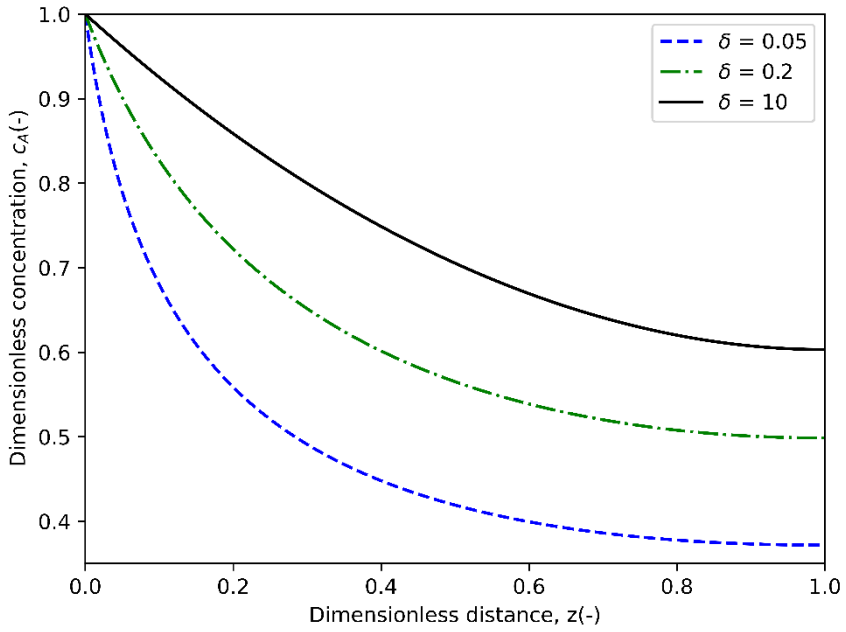

(a)

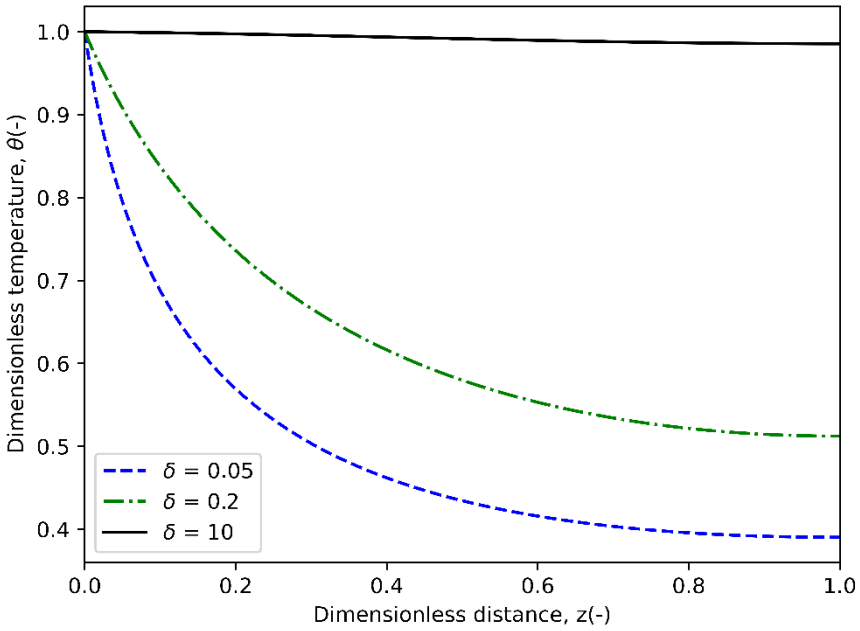

(b)

Figure 5.8 Effect of geometric parameter δ on solution profiles of (a) concentration without dead zones and (b) temperature for $Pe_m = Pe_h = 1, p = 0.5,\ \gamma_1 = 5,\ \varphi_1 = 1.2,$ ***and*** $\beta_1 = 0.1$.

Similarly, the dead-core solution profiles for the dimensionless concentration and temperature are illustrated in **Figure 5.9**, showing the effect of the geometric parameter δ. To obtain the dead-core solutions, the simulations were conducted by keeping $\varphi_1 = 4.5$ and $Pe_m = Pe_h = 0.1$.

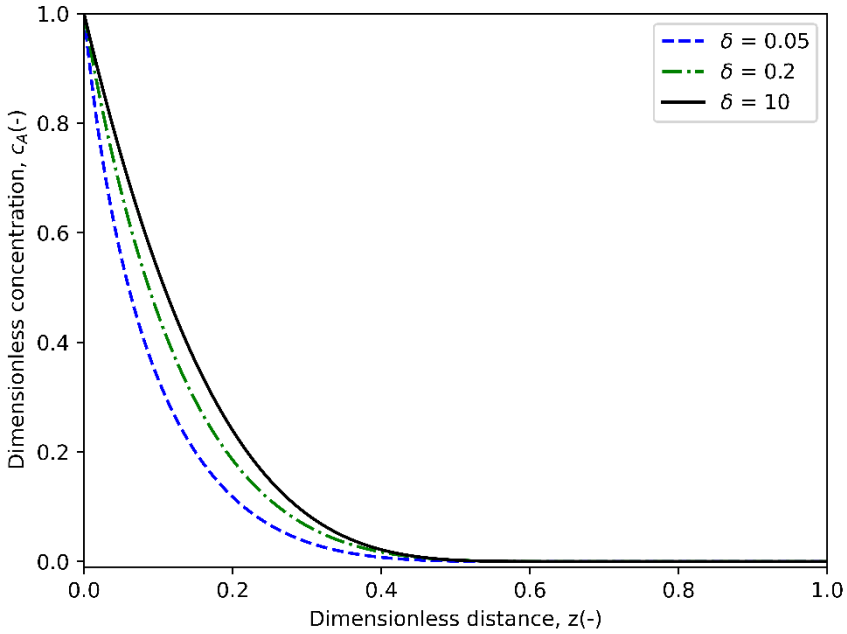

(a)

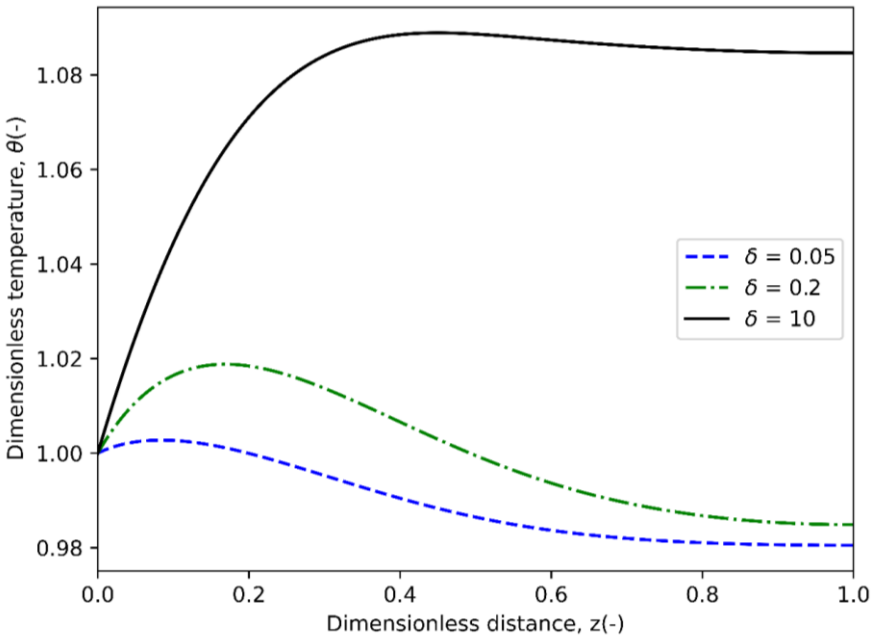

(b)

Figure 5.9 Effect of geometric parameter δ on solution profiles of (a) concentration with dead zones and (b) temperature for $Pe_m = Pe_h = 0.1, p = 0.5$, $\gamma_1 = 5$, $\varphi_1 = 4.5$, and $\beta_1 = 0.1$.

Effects of mass and heat Peclet numbers

The mass and heat Peclet numbers serve as dimensionless parameters that describe the relative contributions of convection to mass and heat transfer with respect to the transport mechanisms of diffusion and conduction, respectively [52].

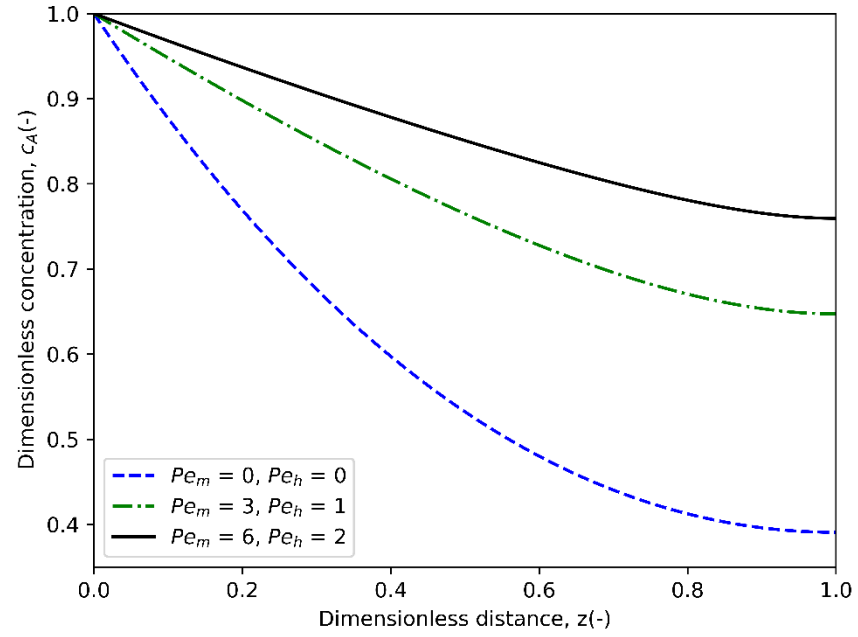

(a)

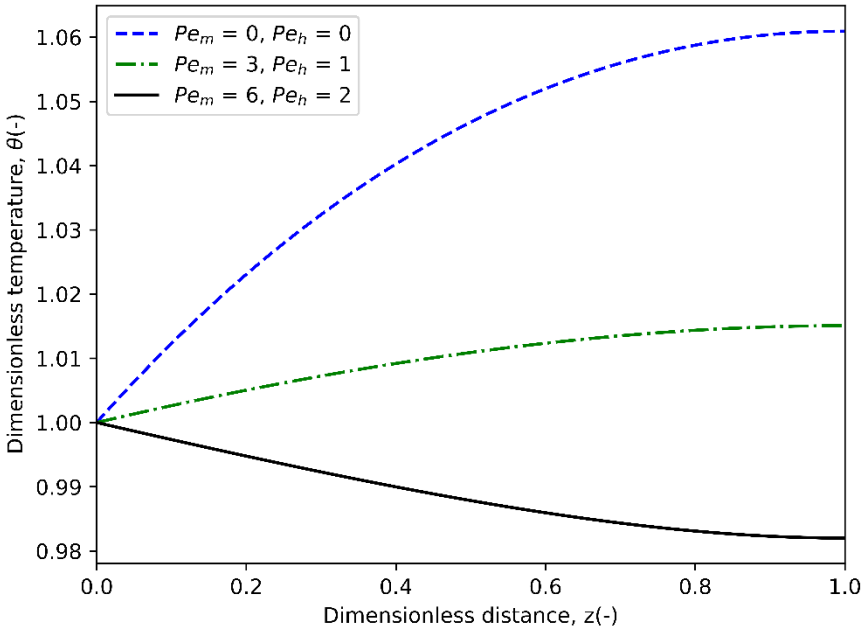

(b)

Figure 5.10 Impact of mass and heat Peclet numbers on solution profiles of (a) concentration and (b) temperature for $\boldsymbol{p = 0.5,\ \gamma_1 = 5,\ \varphi = 1.2,\ \beta_1 = 0.1}$ ***and*** $\boldsymbol{\delta = 10}$.

Figure 5.10 illustrates the effect of mass and heat Peclet numbers on the dimensionless concentration and temperature profile. The following relationship $Pe_m = \alpha \cdot Pe_h$ between these parameters was used in our simulations where α is a predefined number fixed at 3. In the current context, the flow due to convection is considered to be in the positive *z*-direction.

It is worth noting that when the mass Peclet numbers decrease, there is a decrease in the concentration profile of reactant *A*, as shown in **Figure 5.10 (a)**. This decline indicates that diffusion dominates over convection. In other words, a higher diffusion rate compared to convection implies that there could be sufficient time for the reactant *A* to undergo conversion into the product.

Simultaneously, the influence of the heat Peclet number is explored, and remarkable results unfold: there is a shift in the temperature profile with an increase in heat Peclet number, as depicted in **Figure 5.10 (b)**. At lower heat Peclet numbers, there is a notable increase in the temperature of the porous membrane system, i.e. $\theta > 1$. This phenomenon is attributed to the retention of heat within the system, where there is negligible or limited convection, and the transfer of heat is predominantly conduction-based. Conversely, as the heat Peclet number increases, there is a noticeable decline in the temperature of the porous membrane system, i.e. $\theta < 1$. The reason for such a decline in the temperature profile is the same as discussed earlier.

Steady-state non-isothermal conditions for sequential reaction

In this section, we will extend our investigation to study the effects of different parameters on the concentration profiles of *A* and *B* as well as the temperature profile for the consecutive reaction, i.e., $A \xrightarrow{k_1} B \xrightarrow{k_2} C$ as described by Eq. (3.17).

Effects of mass and heat Peclet numbers

Figures 5.11 and **5.12** illustrate the variations in the dimensionless concentration of reactant *A*, intermediate product *B*, and dimensionless temperature by changing the values of Pe_m and Pe_h. During the numerical simulations, the values for the dimensionless parameters were specified as follows: $p = 0.5$, $\varphi_1 = \varphi_2 = 3.5$, $\psi = 1$, $\zeta = 1, \gamma_1 = 10$, $\gamma_2 = 15$, $\beta_1 = \beta_2 = 0.01$, $\delta = 90$. This combination of reaction exponent (p) and Thiele

modulus (φ) results in dead zone formation, especially when the mass Peclet numbers are low. In [11], the necessary and sufficient conditions for the dead zone formation in porous materials were derived. The findings obtained from this study are applicable to the current model, which includes irreversible sequential reactions and power-law kinetics.

The dimensionless concentration profile of reactant *A* is depicted in **Figure 5.11 (a)**. By decreasing the mass Peclet number, the reactant concentration profile undergoes a substantial decline, as shown in **Figure 5.11 (a)**. For lower mass Peclet numbers, the concentration profiles indicate the existence of dead zones. However, when $Pe_m = 15$ there is no prominent dead zone in the concentration profile. Furthermore, it should be noted that the length of dead zone grows as the Peclet number decreases. The lower mass Peclet number indicates that diffusion is more dominant over convection. The enhanced flow rates can lead to an increased reactant concentration, potentially increasing productivity [53]. As shown in **Figure 5.11 (b)**, a higher concentration of the intermediate product *B* is observed till a specific point in the porous membrane for the lower values of mass Peclet number, i.e., $Pe_m = 5$ followed by $Pe_m = 10$. The highest concentration profile is observed at the end of the porous membrane when $Pe_m = 15$**.** This is attributed to the formation of dead-zone for reactant *A* at lower mass Peclet numbers. Achieving a higher concentration of product *B* at the outlet of the membrane requires a high mass Peclet number Pe_m. This observation is because convection substantially accelerates the removal of our intermediate product *B* from the porous membrane prior to its subsequent reactions, resulting in the formation of product *C*. **Figure 5.11 (c)** illustrates the maximum dimensional temperature value corresponding to the highest mass Peclet number.

Similarly, the impact of heat Peclet number Pe_h on the solution profiles is shown in **Figure 5.12**. Notably, the change in Pe_h does not affect the profile of the dimensionless concentration of reactant *A*, as shown in **Figure 5.12 (a)**.

The impact of the heat Peclet number on the intermediate product *B* concentration profile and the temperature profile exhibits an inverse relationship. The higher heat Peclet number values result in an increased concentration profile of *B*, as shown in **Figure 5.12 (b)**. On the other hand, lower temperature profiles were observed at higher heat Peclet numbers, as presented in **Figure 5.12 (c)**.

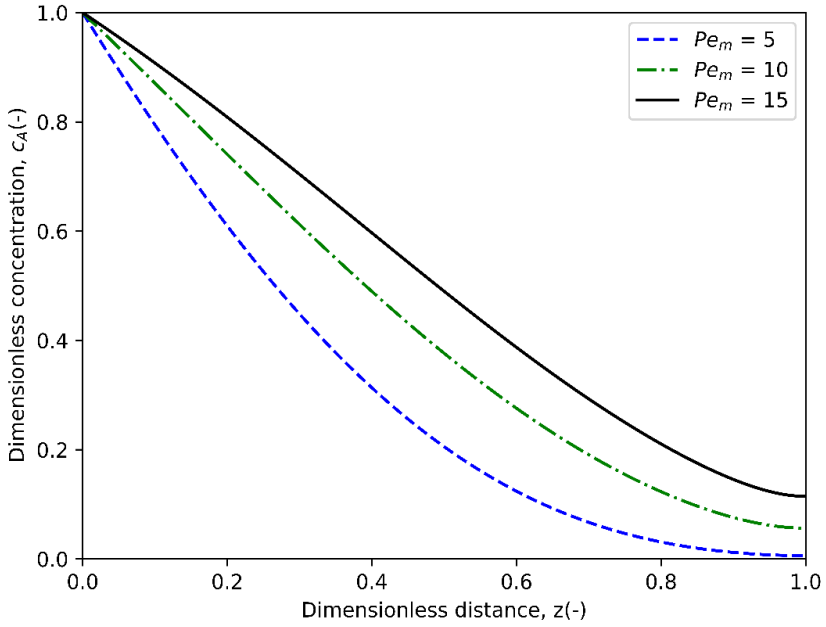

(a) Reactant *A*

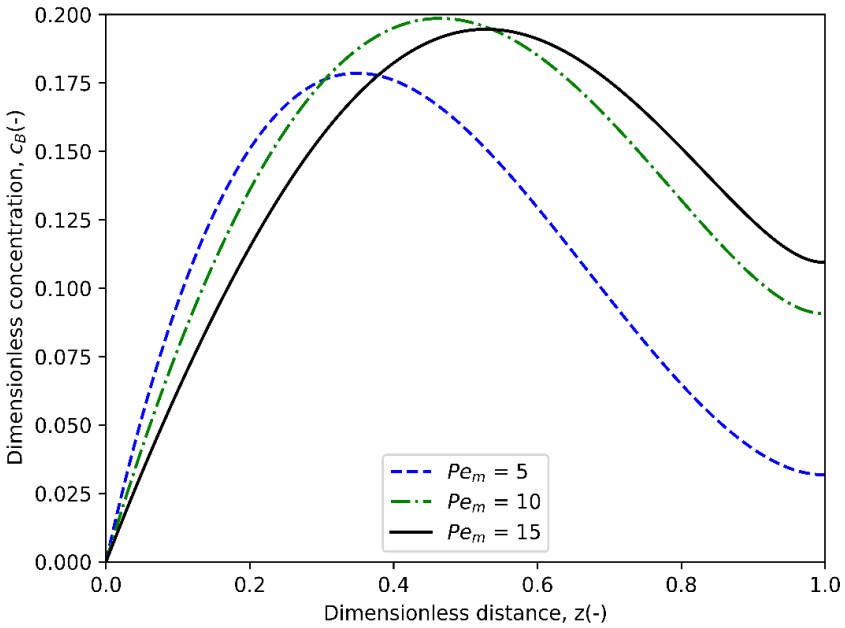

(b) Intermediate product *B*

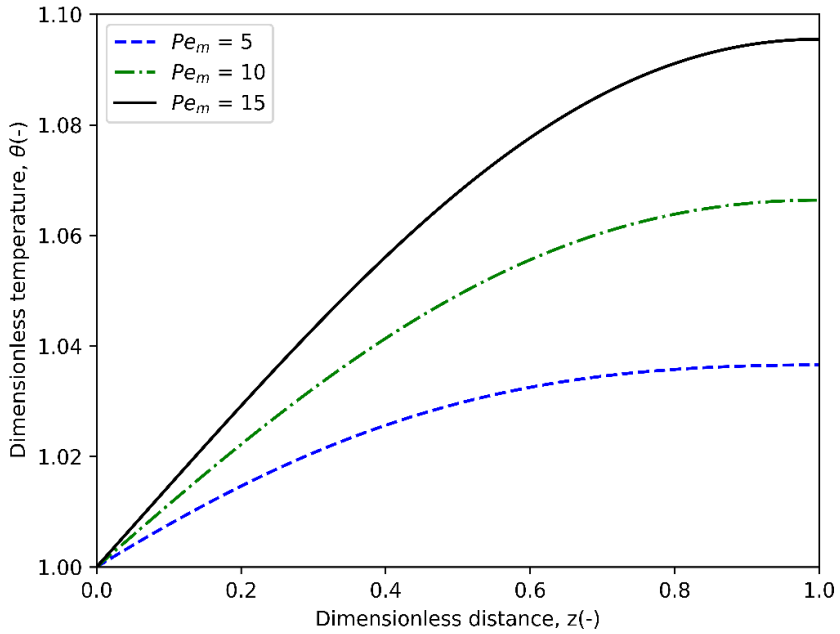

(c) Temperature

Figure 5.11 Impact of mass Peclet number on dimensionless concentration profiles of (a) reactant A (b) intermediate product B, and (c) dimensionless temperature profile in the porous membrane system for $p = 0.5$, $Pe_h = 1, \gamma_1 = 10, \gamma_2 = 15$, $\varphi_1 = \varphi_2 = 3.5, \psi = 1, \zeta = 1.0$, $\beta_1 = \beta_2 = 0.01$ ***and*** $\delta = 90$.

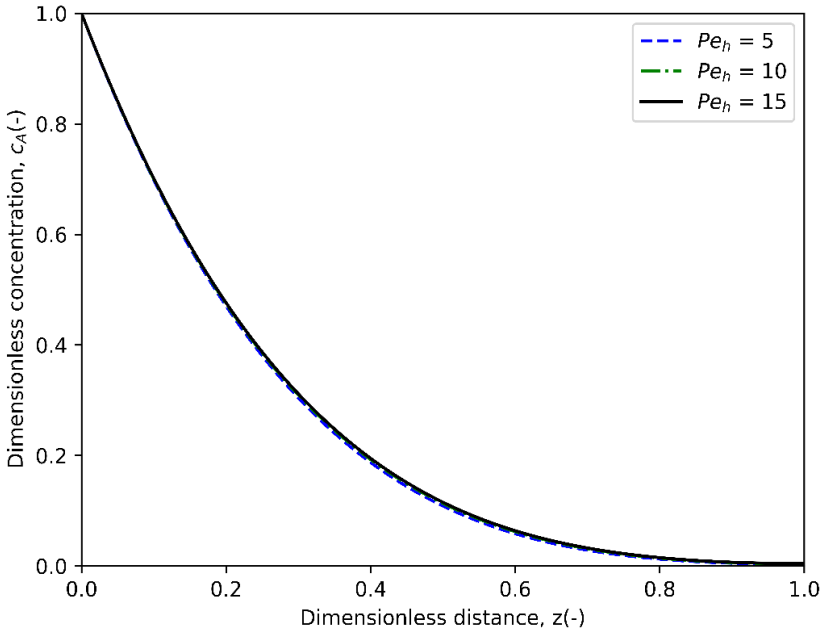

(a) Reactant *A*

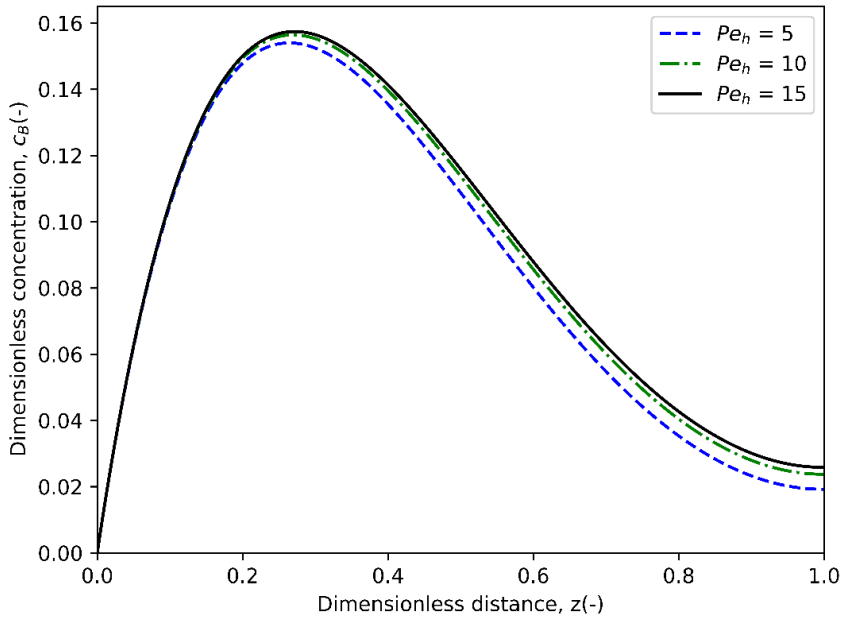

(b) Intermediate product *B*

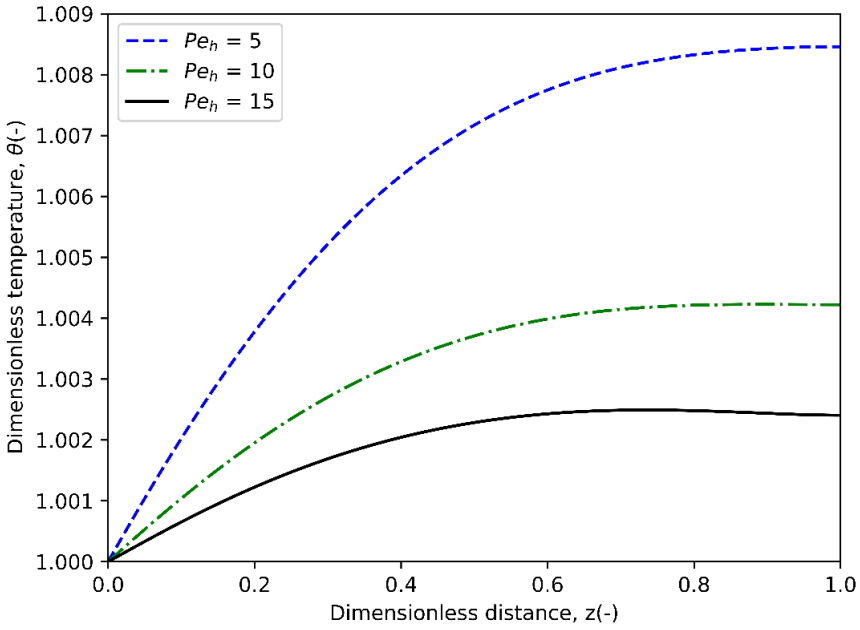

(c) Temperature

Figure 5.12 Impact of heat Peclet number on dimensionless concentration profiles of (a) reactant A (b) intermediate product B, and (c) dimensionless temperature profile in the porous membrane system for $\boldsymbol{p = 0.5, Pe_m = 1,\ \gamma_1 = 10, \gamma_2 = 15,\ \varphi_1 = \varphi_2 = 3.5, \psi = 1, \zeta = 1.0,\ \beta_1 = \beta_2 = 0.01\ and\ \delta = 90}$.

Effects of Thiele moduli

Figure 5.13 illustrates the impact of Thiele moduli on the concentration profiles and temperature. By decreasing the value of the Thiele modulus φ_1 while keeping the φ_2 constant, the concentration of reactant *A* increases, as shown in **Figure 5.13 (a)**. In the current scenario, the conditions for the development of dead zones involve maintaining the values of $p = 0.5$, $\varphi_1 = \varphi_2 = 3$.

As shown in **Figure 5.13 (b)**, a higher dimensionless concentration of the intermediate product *B* is observed till a specific point in the membrane for $\varphi_1 = \varphi_2 = 3$. This concentration of intermediate product *B* subsequently decreases until the end of the membrane, which is attributed to the dead zone formation for reactant *A* under these specified conditions. The highest concentration of *B* is observed at the end of the membrane when $\varphi_1 = 2$, $\varphi_2 = 3$, as depicted in **Figure 5.13 (b).** During the numerical simulations, the values for the dimensionless parameters were specified as follows: $p = 0.5$, $Pe_m = 1$, $Pe_h = 1$, $\psi = 1$, $\zeta = 1$, $\gamma_1 = 10$, $\gamma_2 = 15$, $\beta_1 = \beta_2 = 0.01$, $\delta = 90$.

The temperature decreases as the value of the Thiele modulus decreases, as illustrated in **Figure 5.13 (c).**

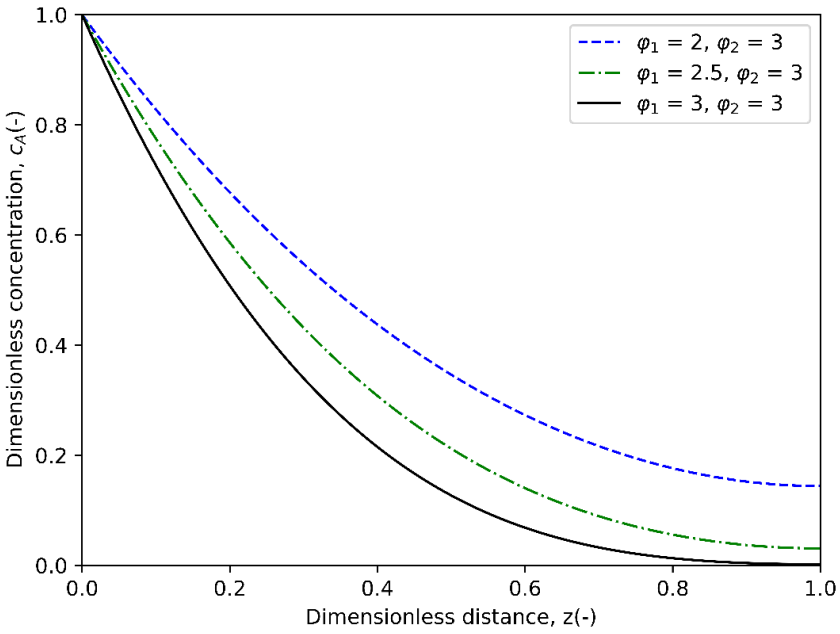

(a) Reactant *A*

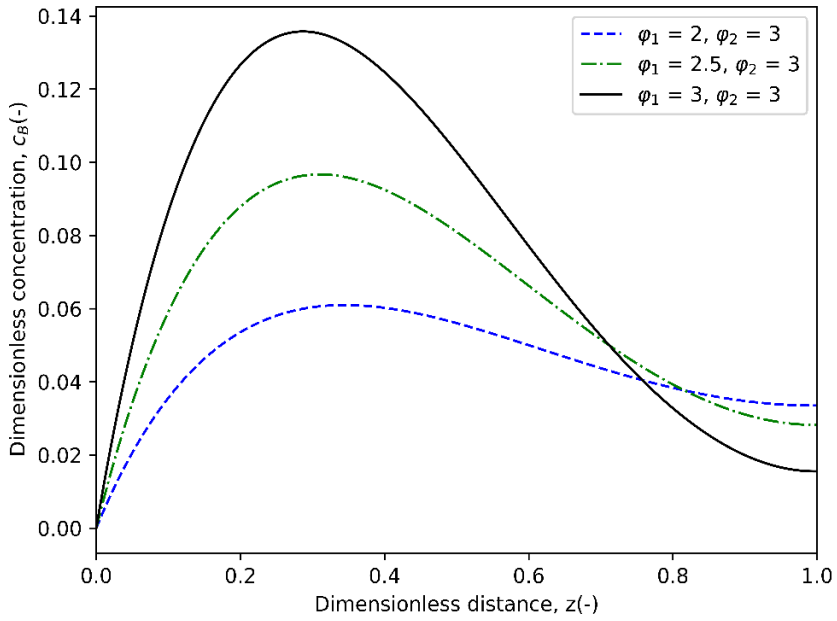

(b) Intermediate product *B*

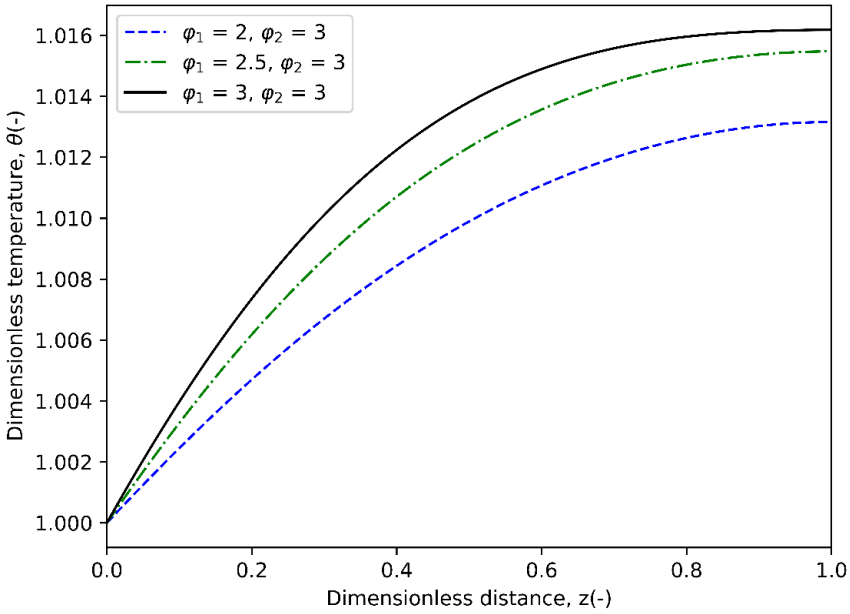

(c) Temperature

Figure 5.13 Impact of Thiele moduli on dimensionless concentration profiles of (a) reactant A (b) intermediate product B, and (c) dimensionless temperature profile in the porous membrane system for $p = 0.5, Pe_m = 1, Pe_h = 1, \gamma_1 = 10, \gamma_2 = 15, \psi = 1, \zeta = 1.0, \beta_1 = \beta_2 = 0.01$ ***and*** $\delta = 90$.

Effects of reaction exponent

The influence of the reaction exponent on the concentration and temperature profiles is shown in **Figures 5.14**, **5.15**, and **5.16**. For reaction exponents $0 < p < 1$ and $p > 1$, **Figures 5.14** and **5.15**, respectively, show the solution profiles with no dead zone.

Comparable trends are presented in **Figures 5.14 (a)** and **5.15 (a)**. In both scenarios, the concentration of reactant *A* decreases more rapidly as the reaction exponent decreases. Similarly, as illustrated in **Figures 5.14 (b)** and **5.15 (b)**, a higher concentration of the intermediate product *B* is attained when the reaction exponents are decreased. Moreover, at the end of the porous membrane system, i.e., $z = 1$, there is a simultaneous decrease in the concentration of reactant *A* and an increase in the concentration of *B*. The higher temperature values are observed at lower values of the reaction exponent, as shown in Figures **5.14** and **5.15**. The simulation parameters were specified as follows: $Pe_m = 1$, $Pe_h = 1$, $\varphi_1 = 1.5$, $\varphi_2 = 0.5$, $\psi = 1$, $\zeta = 1$, $\gamma_1 = 10$, $\gamma_2 = 15$, $\beta_1 = \beta_2 = 0.01$, $\delta = 90$.

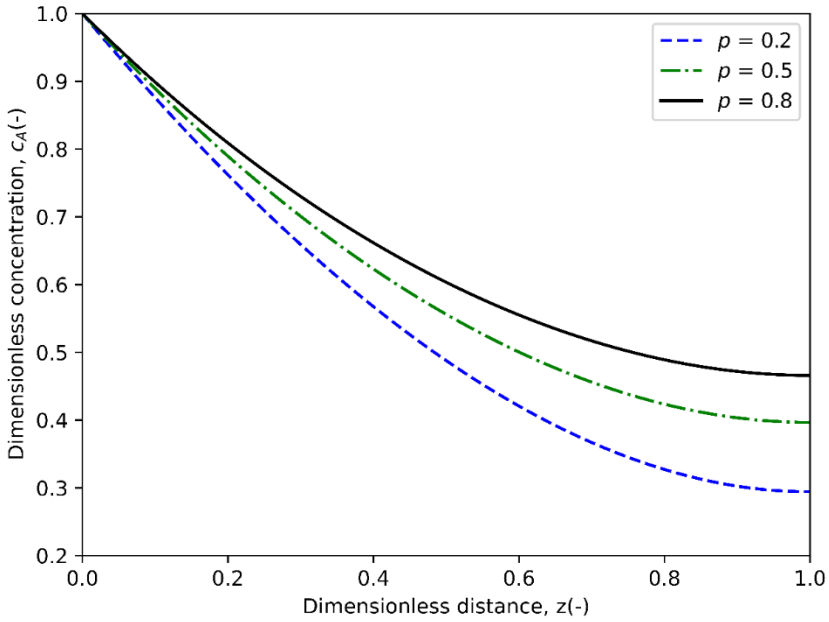

(a) Reactant *A*

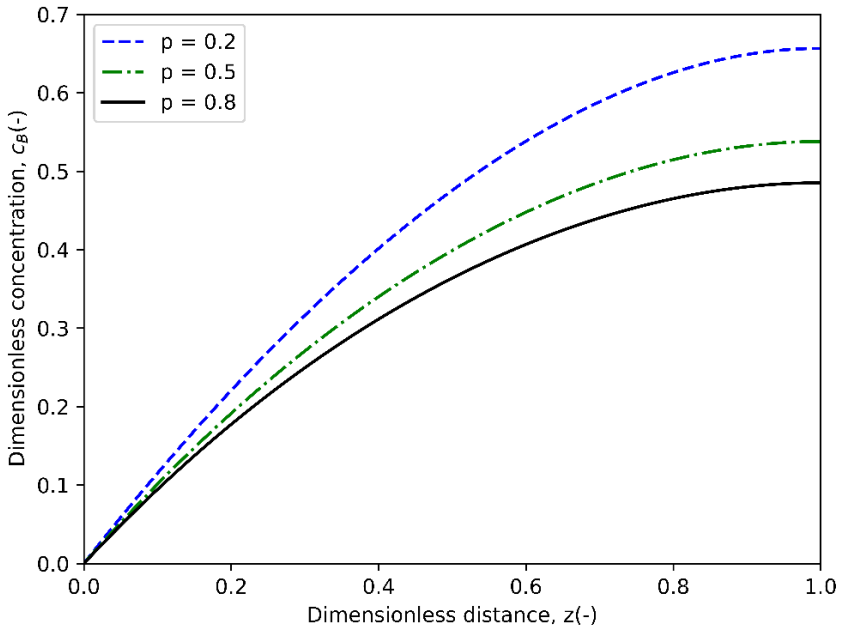

(b) Intermediate product *B*

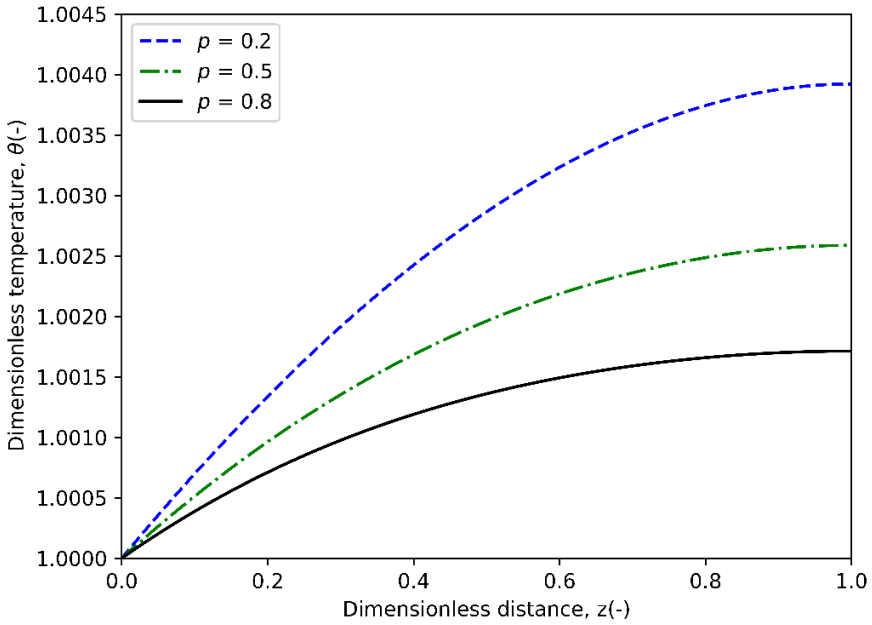

(c) Temperature

Figure 5.14 Impact of reaction exponent $p < 1$ on dimensionless concentration profiles of (a) reactant A (b) intermediate product B, and (c) dimensionless temperature profile in porous membrane system for $Pe_m = 1, Pe_h = 1,\ \gamma_1 = 10, \gamma_2 = 15, \varphi_1 = 1.5, \varphi_2 = 0.5, \psi = 1, \zeta = 1,\ \beta_1 = \beta_2 = 0.01$ and $\delta = 90$.

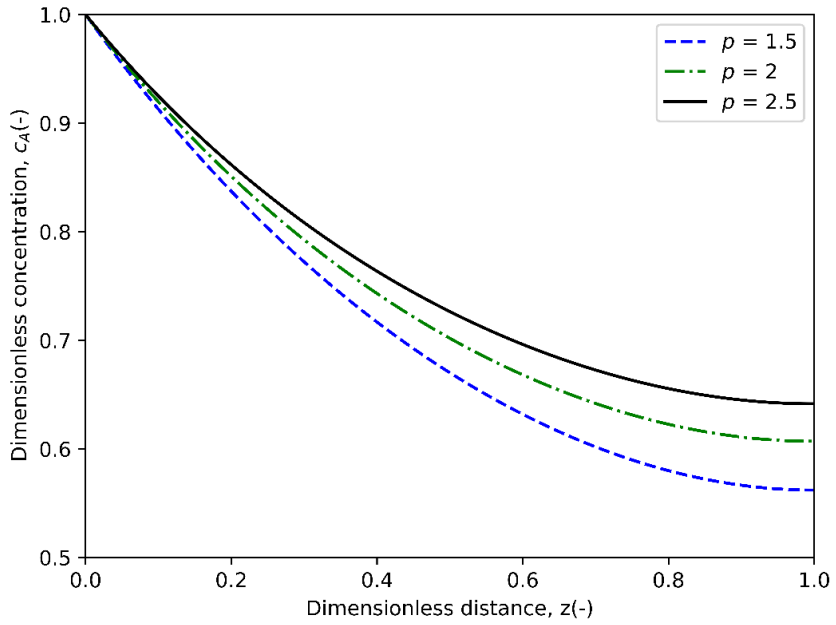

(a) Reactant *A*

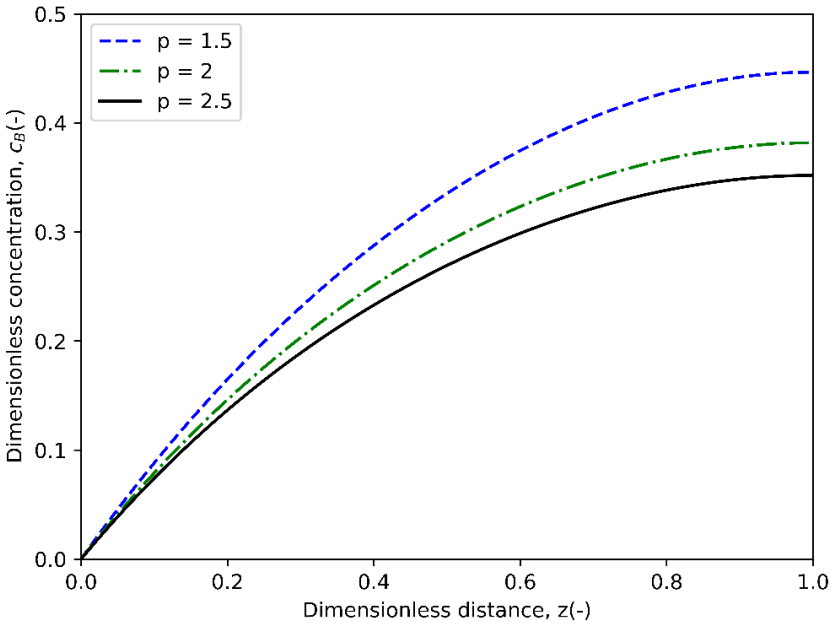

(b) Intermediate product *B*

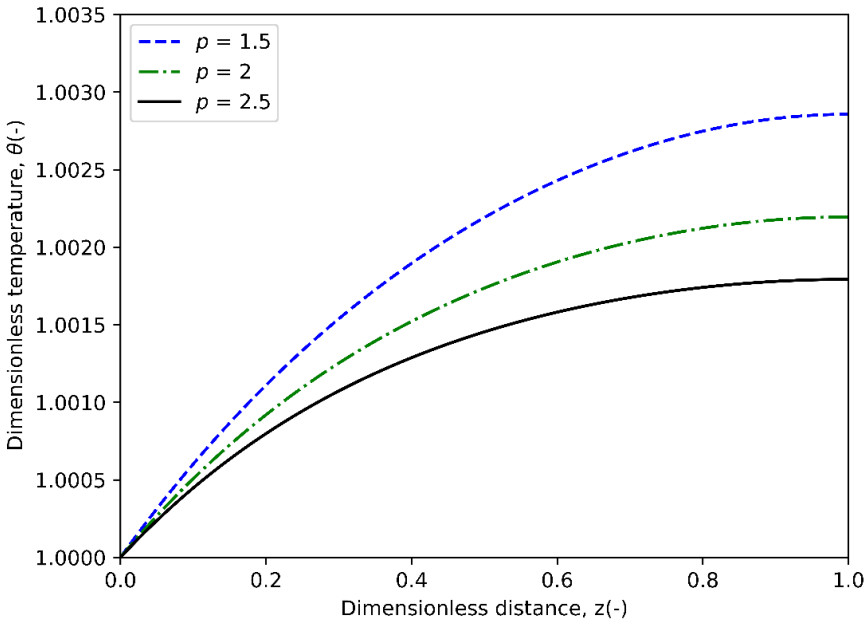

(c) Temperature

Figure 5.15 Impact of reaction exponent $p > 1$ on dimensionless concentration profiles of (a) reactant A (b) intermediate product B, and (c) dimensionless temperature profile in porous membrane system for $Pe_m = 1, Pe_h = 1,\ \gamma_1 = 10, \gamma_2 = 15, \varphi_1 = 1.5, \varphi_2 = 0.5, \psi = 1, \zeta = 1,\ \beta_1 = \beta_2 = 0.01$ and $\delta = 90$.

Solution profiles with dead zones, as shown in **Figure 5.16**, are obtained for $\varphi_1 = 10$ and $\varphi_2 = 5$. The length of the dead zone grows as the value of the reaction exponent decreases. Furthermore, **Figure 5.16 (c)** shows the temperature profiles.

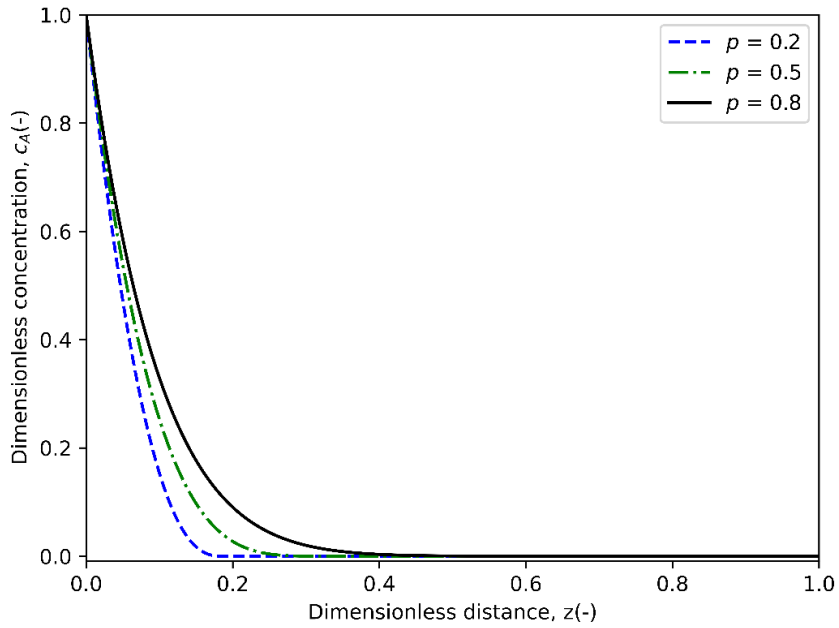

(a) Reactant *A*

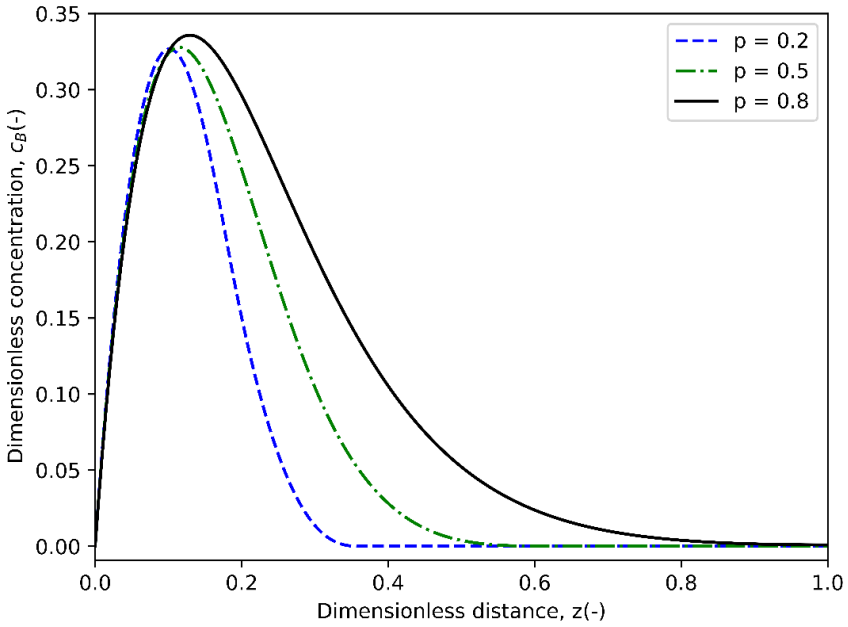

(b) Intermediate product *B*

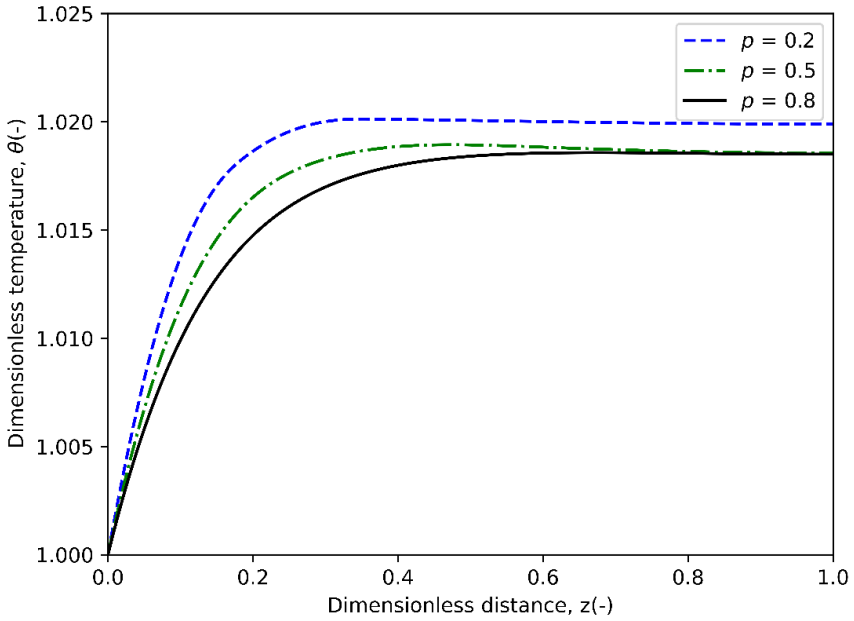

(c) Temperature

Figure 5.16 Impact of reaction exponent $p < 1$ on dimensionless concentration profiles of (a) reactant A (b) intermediate product B, and (c) dimensionless temperature profile in porous membrane system for $Pe_m = 1, Pe_h = 1,\ \gamma_1 = 10, \gamma_2 = 15, \varphi_1 = 10, \varphi_2 = 5, \psi = 1, \zeta = 1.0,\ \beta_1 = \beta_2 = 0.01$ and $\delta = 90$.

5.1.3 Effect of process parameters on reactor performance indicators

The crucial performance indicators in a system with multiple reactions encompass the conversion of reactants, selectivity of the desired product, and overall yield. The definitions of these performance indicators are given below [54]:

Conversion

Conversion refers to the extent to which reactants are transformed into desired products in a chemical reaction.

$$X = \frac{F_{A,0} - F_A}{F_{A,0}} \tag{5.1}$$

where $F_{A,0}$ represents the inlet molar flow rate of reactant *A*.

Selectivity

Selectivity measures the extent to which a chemical reaction produces a specific desired product compared to undesired by-products.

$$S = \frac{moles\ of\ desired\ product\ formed}{moles\ of\ undesired\ product\ formed} \tag{5.2}$$

Similarly, it can be written as follows:

$$S = \frac{F_D - F_{D,0}}{F_U - F_{U,0}} \tag{5.3}$$

where F_D and F_U are the flow rates of the desired and undesired products respectively.

Yield

Yield represents the efficiency of a chemical reaction in producing the desired product, taking into account both conversion and selectivity.

$$Y = \frac{moles\ of\ desired\ product\ formed}{moles\ of\ reactant\ fed} \tag{5.4}$$

Similarly, it can be written as follows:

$$Y = \frac{F_D - F_{D,0}}{F_{A,0} - F_A} \tag{5.5}$$

In the context of flow-through catalytic membrane reactors, a notable distinction arises concerning lower membrane thickness when contrasted with other types of reactors, such as packed-bed reactors. Additionally, the membrane's pores exhibit a straight and relatively larger configuration, resulting in a negligible pressure drop [55]. Consequently, within this framework, the performance indicators could be defined as follows:

Conversion: $$X = 1 - c_{A,\mathrm{exit}} \tag{5.6}$$

Selectivity: $$S = \frac{c_{B,\mathrm{exit}}}{1 - c_{A,\mathrm{exit}}} \tag{5.7}$$

Yield: $$Y = c_{B,\mathrm{exit}} = X \cdot S\,, \tag{5.8}$$

where $c_{A,\mathrm{exit}}$ and $c_{B,\mathrm{exit}}$ denotes the dimensionless concentrations of reactant *A* and our desired product *B*, respectively, in the reactor exhaust.

In this section, we will comprehensively analyze the reactor performance indicators. We will explore the effect of mass and heat Peclet groups on the selectivity and yield of the desired product *B*. **Figure 5.17** demonstrates the impact of mass Peclet number Pe_m on the selectivity and yield of desired intermediate product *B* in a sequential reaction under isothermal conditions. With an increase in mass Peclet number, there is a noticeable increase in the selectivity of desired product *B*.

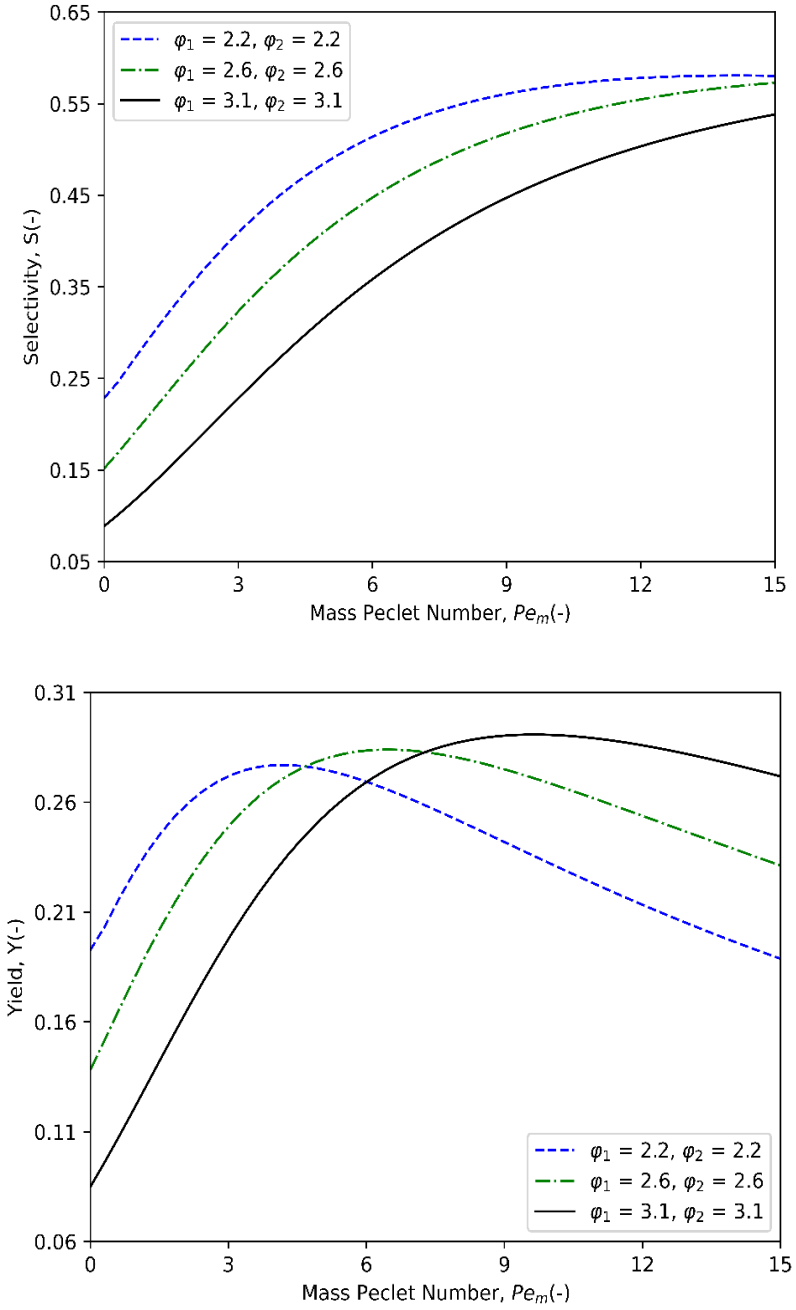

Figure 5.17 Effect of mass Peclet number Pe_m on (a) selectivity and (b) yield of desired product B in sequential reaction under isothermal conditions for $\psi = 1, \zeta = 1.0, p = 0.5$ and $\delta = 10$.

Significantly, the effect of convective flow becomes more prominent for Thiele moduli $\varphi_1 = \varphi_2 = 3.1$. The selectivity undergoes a substantial increase from 8% to 54% depending on the value of Pe_m, as illustrated in **Figure 5.17 (a)**. Furthermore, the yield of Product *B* reaches maximum, where its location shifts towards higher Pe_m values with an increase in Thiele modulus values, as shown in **Figure 5.17 (b)**.

Figure 5.18 shows the effect of the mass Peclet number Pe_m on the selectivity and yield of the desired product *B* under non-isothermal conditions, where heat is solely transferred through conduction, i.e., $Pe_h = 0$, thus emphasizing a more pronounced temperature effect. The selectivity exhibits a monotonic increase with an increase in mass Peclet number, specifically for low Thiele moduli values, as shown in **Figure 5.18 (a)**. However, within an optimal range of φ_1 and φ_2, the selectivity reaches its maximum values as Pe_m increases. **Figure 5.18 (b)** shows the effect of Pe_m on the yield of the desired product. It is worth mentioning that there is a specific Pe_m value that may be determined to attain the highest yield. The yield varies significantly between 0.10 and 0.25, depending on Pe_m, when $\varphi_1 = \varphi_2 = 2.6$. These findings hold significant implications while designing a cylindrical catalytic membrane reactor.

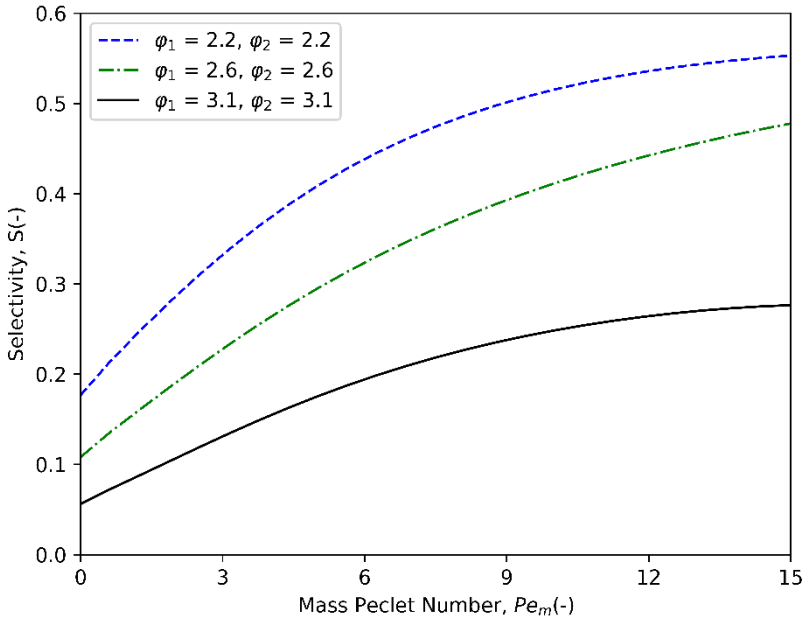

(a)

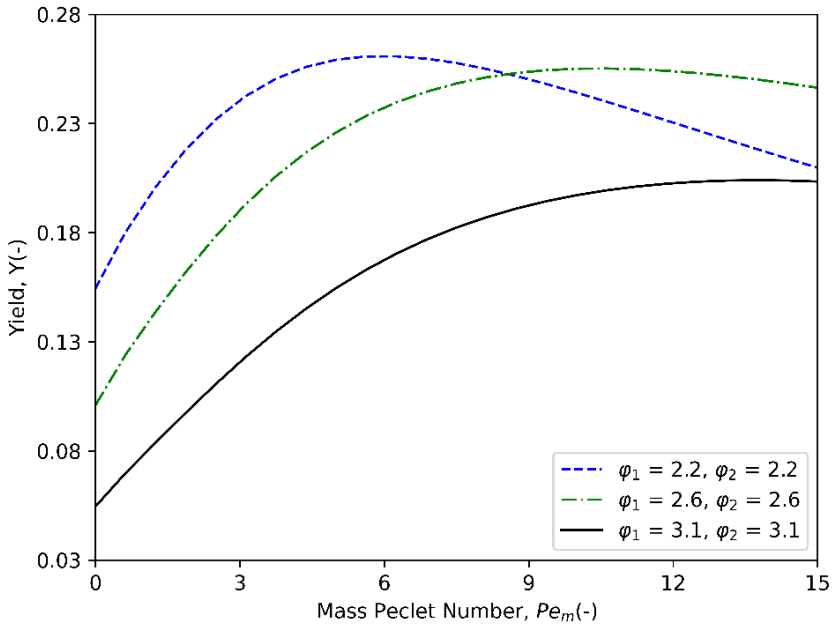

(b)

Figure 5.18 Impact of mass Peclet number Pe_m on (a) selectivity and (b) yield of desired product B in sequential reaction under non-isothermal conditions for $Pe_h = 0, p = 0.5, \gamma_1 = 10, \gamma_2 = 15, \psi = 1, \zeta = 1.0, \beta_1 = \beta_2 = 0.01$ and $\delta = 10$.

Figure 5.19 demonstrates the influence of the heat Peclet number Pe_h on the selectivity and yield of product *B* such that the ratio of mass to heat Peclet number remains constant, i.e., $\frac{Pe_m}{Pe_h} = const.$ With an increase in heat Peclet number, the amount of heat dissipated is dominated by convection. This results in a drop in the temperature within the membrane, which is a favorable condition for selectivity. This is especially beneficial because the activation energy required for the second reaction is greater than that for the first reaction. The selectivity demonstrates an increasing trend as the heat Peclet number increases, particularly for low Thiele moduli values, as shown in **Figure 5.19 (a)**. As illustrated in **Figure 5.19 (b)**, the yield attains its highest value at the specific Pe_h, and the peak shifts towards higher values of Pe_h depending upon the values of Thiele moduli φ_1 and φ_2.

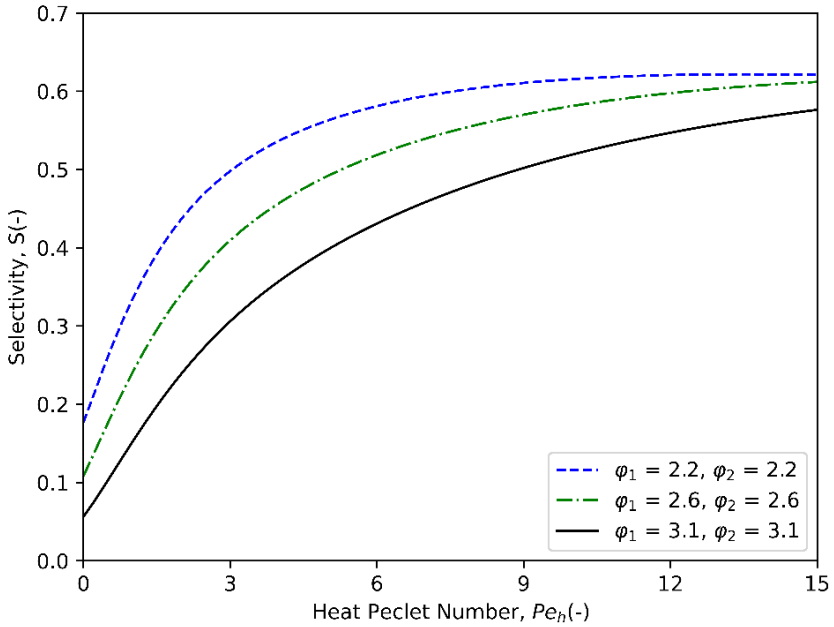

(a)

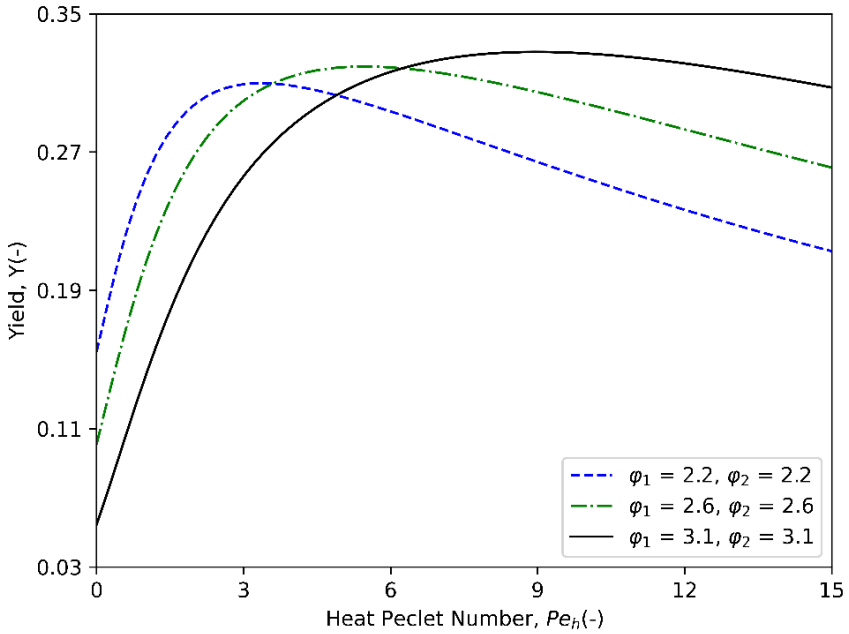

(b)

Figure 5.19 Impact of heat Peclet number Pe_h on (a) selectivity and (b) yield of desired product B in sequential reaction under non-isothermal conditions for $\frac{Pe_m}{Pe_h} = 3, p = 0.5, \gamma_1 = 10, \gamma_2 = 15, \psi = 1, \zeta = 1.0, \beta_1 = \beta_2 = 0.01$ and $\delta = 10$.

5.2 Unsteady-state condition

In this section, we will expand our investigation to include discussions of results under unsteady-state conditions. We will explore concentration and temperature profiles, examining the effects of various parameters on them. Furthermore, we will calculate productivity under both isothermal and non-isothermal conditions, compare it with steady-state conditions, and determine the percentage increment.

5.2.1 Unsteady-state isothermal conditions for a single reaction

We will begin by analyzing the convection-diffusion-reaction problem described by Eqs. (4.29) and (4.30), where *A* transforms into *P* $(A \rightarrow P)$ under unsteady-state, isothermal conditions with power-law kinetics.

Concentration profile of reactant *A*

Figure 5.20 illustrates the concentration profile for reactant *A* under unsteady-state isothermal conditions.

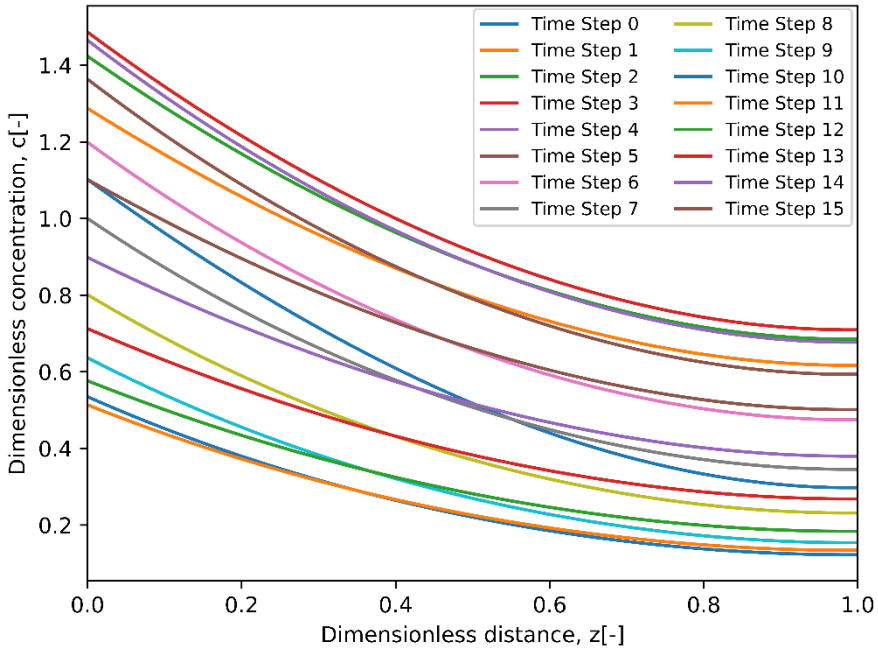

Figure 5.20 Concentration profile of reactant A under unsteady-state isothermal conditions for $Pe_m = 1, \varphi = 1.5, \varepsilon = 0.6, p = 0.5, \delta = 10, \delta_{mA} = 0.5, \omega_{mA} = 1.$

Multiple colored lines, each representing a different time step, provide clear evidence of the dynamic behavior of the concentration distribution. The concentration profile exhibits fluctuations. As time progresses, the concentration varies, displaying transient behavior. The time-dependent boundary conditions and other system dynamics could influence these fluctuations. Understanding these variations is essential for practical applications and process optimization.

Impact of parameter δ_{mA}

Figure 5.21 illustrates the influence of the parameter δ_{mA} on the concentration profile of reactant *A*. The observed trend indicates that an increase in the value of δ_{mA} is associated with a decrease in the concentration at the inlet. This decrease can be attributed to the time-dependent boundary conditions at the inlet. It is worth mentioning that the concentration profile at $\delta_{mA} = 0$ represents steady-state conditions, thereby serving as a point of reference when contrasting values of δ_{mA}, whose comparison is already described.

The numerical simulations were conducted by keeping the following parameters: $\varphi = 1.5$, $Pe_m = 1$, $p = 0.5$, $\varepsilon = 0.6$, $\delta = 10$, and $\omega_{mA} = 0.55$.

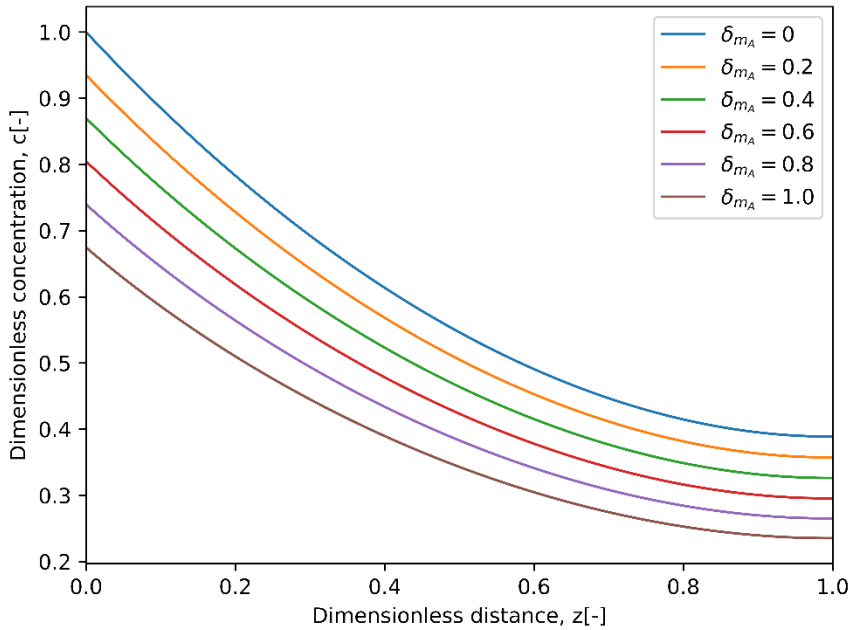

Figure 5.21 Effect of δ_{mA} on concentration profile of reactant A under unsteady-state, isothermal conditions for $\varphi = 1.5, Pe_m = 1, p = 0.5, \varepsilon = 0.6, \delta = 10, \omega_{mA} = 0.55$.

Impact of parameter ω_{mA}

Figure 5.22 shows the influence of the parameter ω_{mA} in terms of τ_c. From its mathematical relationship, we know that the ω_{mA} and τ_c have inverse correlation. Increasing the value of τ_c results a corresponding decrease in the value of ω_{mA}. The concentration profile exhibits noticeable fluctuations by varying the value of τ_c. Such fluctuations are attributed to the impact of time-dependent boundary conditions at the inlet, which incorporates this term.

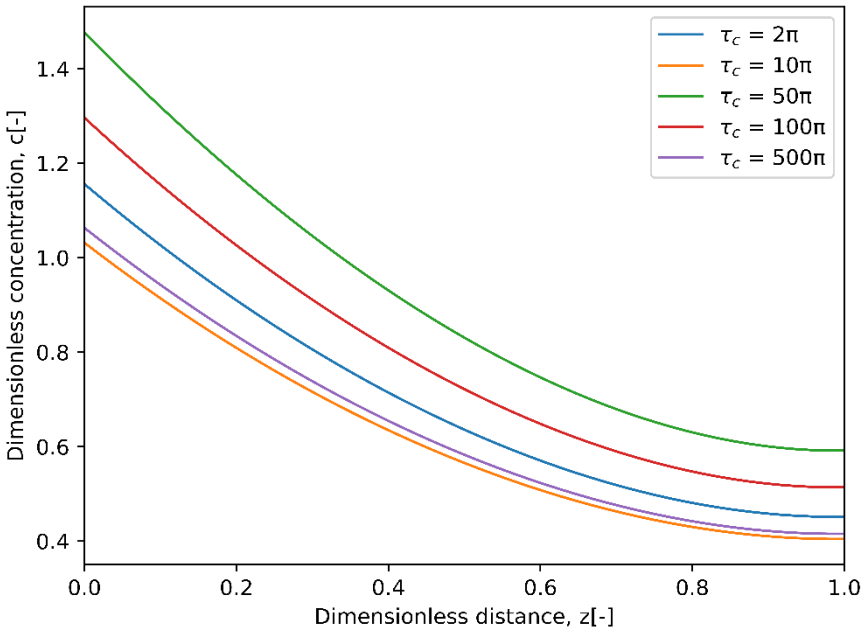

Figure 5.22 Effect of ω_{mA} in terms of τ_c on concentration profile of reactant A under unsteady-state isothermal conditions for $\varphi = 1.5, Pe_m = 1, p = 0.5, \varepsilon = 0.6, \delta = 10, \delta_{mA} = 1, p_c = 1$

Similarly, the impact of ω_{mA} in terms of p_c is shown in **Figure 5.23**. The numerical simulations were conducted by keeping the process parameters as follows:

$\varphi = 1.5$, $Pe_m = 1$, $p = 0.5$, $\varepsilon = 0.6$, $\delta = 10$, and $\delta_{mA} = 1$

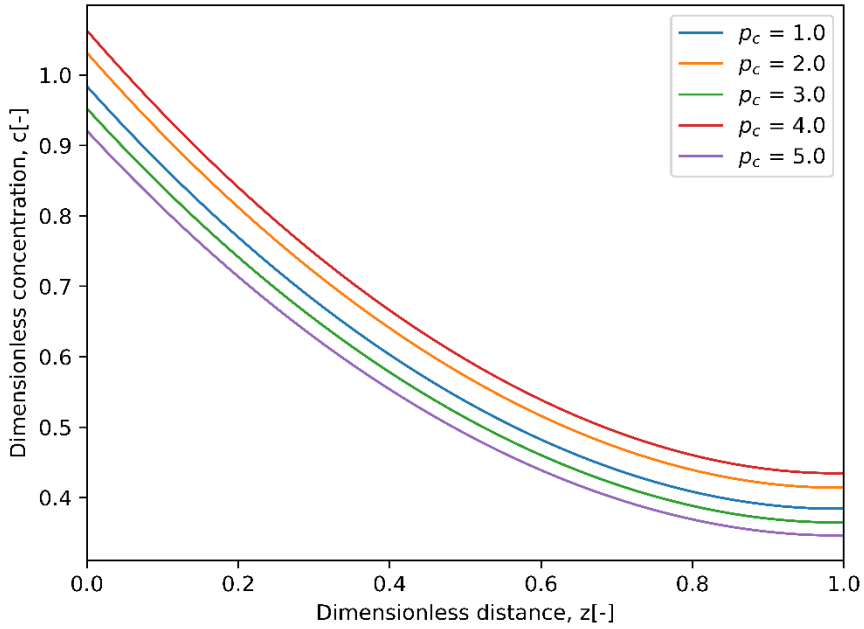

Figure 5.23 Effect of ω_{mA} in terms of p_c on concentration profile of reactant A under unsteady-state isothermal conditions for $\varphi = 1.5, Pe_m = 1, p = 0.5, \varepsilon = 0.6, \delta = 10, \delta_{mA} = 1, \tau_c = 2\pi$.

Productivity

Table 5.1 provides the maximum productivity values attained by varying parameters under unsteady-state and isothermal conditions. The table also encompasses the productivity measurements under steady-state and the corresponding percent increments.

It is worth mentioning that the highest percentage increment in productivity is observed in the scenario where $p = 1.5$ and $Pe_m = 0.5$. The simulations were conducted by varying p, Pe_m, δ_{mA}, and ω_{mA}. The other simulation parameters that were kept constant are as follows as: $\varphi = 2.5$, $\varepsilon = 0.6$, and $\delta = 10$.

Table 5.1 Productivity and percent increment for a single reaction under isothermal conditions

p	Pe_m	Max. Productivity (unsteady-state)	Productivity (steady-state)	Percent increment	δ_{mA}	ω_{mA}
0.5	0.1	203.827	203.528	0.15	0.2	2.5e-5
1.0	0.1	195.033	195.024	0.0041	0.1	6.25e-6
1.0	0.5	195.423	195.411	0.005	0.1	6.25e-6
1.5	0.1	211.889	191.804	10.5	0.99	2.5e-5
1.5	0.5	205.142	148.929	37.8	0.99	2.5e-5
1.5	1.0	192.807	157.749	22.3	0.99	2.5e-5
1.5	5	239.204	217.303	10.1	0.99	0.001
1.5	10	294.225	262.485	12.1	0.99	0.001
1.5	15	327.554	288.267	13.6	0.99	0.006

Figure 5.24 illustrates the impact of δ_{mA} on the productivity percent increment while maintaining conditions of $p<1$ and $Pe_m=15$. It is evident from the figure that the highest percent increment is attained at lower values of δ_{mA}. Similarly, **Figure 5.25** shows the influence of parameter ω_{mA} under similar conditions on the productivity percent increment. The higher percent increment is attained at lower values of ω_{mA}. The results obtained are also presented in **Table 5.1**. The numerical simulations were conducted by keeping the parameters as follows: $\varphi=2.5$, $\varepsilon=0.6$, $\delta=10$, $p=0.5$ and $Pe_m=15$.

Furthermore, **Figure 5.26** illustrates the impact of δ_{mA} on the productivity percent increment by keeping the conditions, i.e., $p>1$ and $Pe_m=15$. The highest percent increment in productivity is attained at higher values of δ_{mA}. The impact of ω_{mA} on productivity percent increment is shown in **Figure 5.27**. These results are also supported by the findings presented in **Table 5.1**. The parameters used are $\varphi=2.5$, $\varepsilon=0.6$, $\delta=10$, $p=1.5$ and $Pe_m=15$.

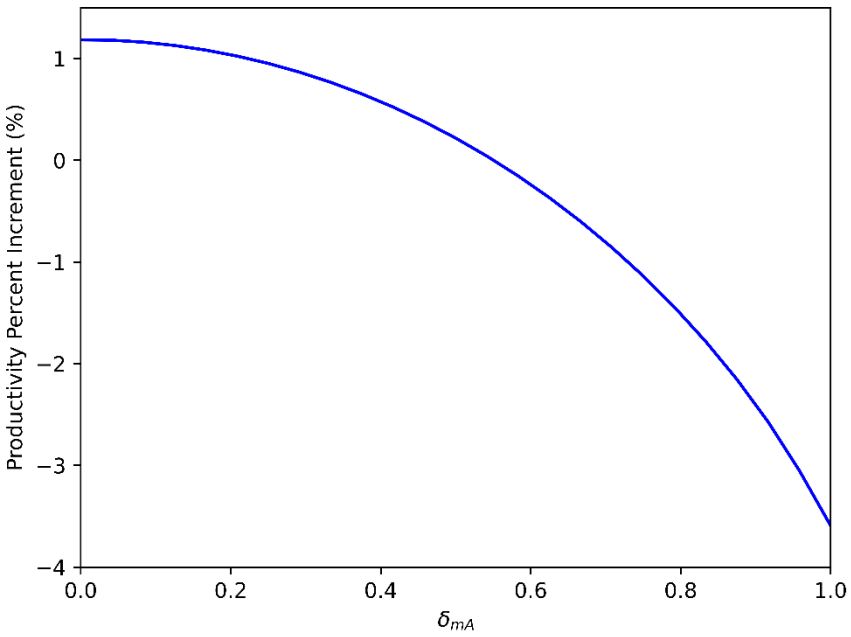

Figure 5.24 Impact of δ_{mA} on productivity percent increment by keeping $\varphi = 2.5$, $\varepsilon = 0.6$, $\delta = 10$, $Pe_m = 15, p = 0.5$, and $\omega_{mA} = 2e - 4$.

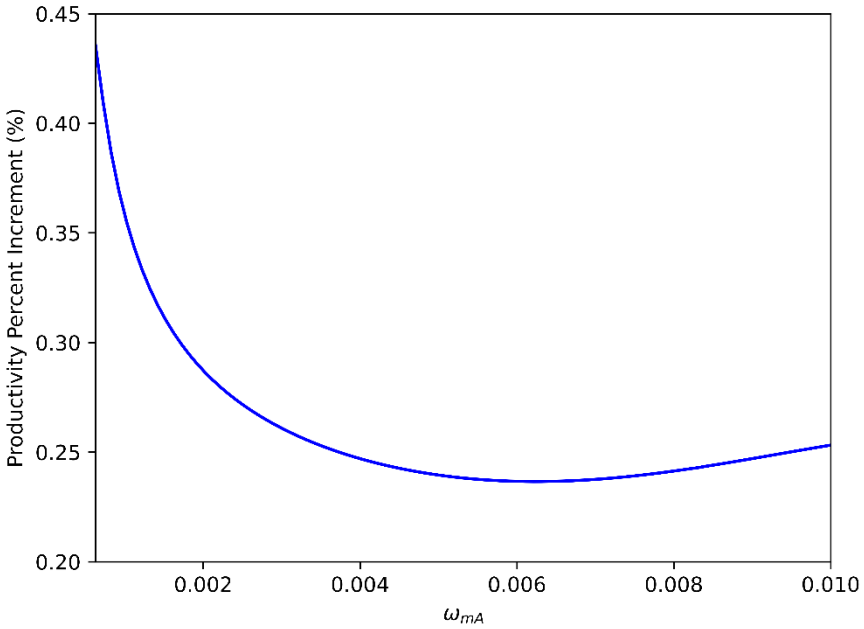

Figure 5.25 Impact of ω_{mA} on the productivity percent increment by keeping $\varphi = 2.5$, $\varepsilon = 0.6$, $\delta = 10$, $Pe_m = 15, p = 0.5$, and $\delta_{mA} = 0.1$.

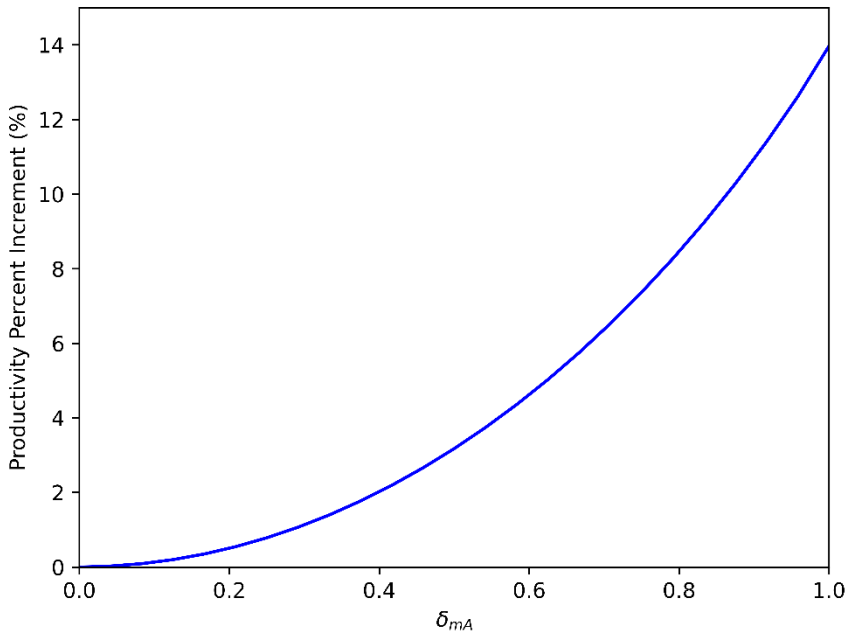

Figure 5.26 Impact of δ_{mA} on the productivity percent increment by keeping $\varphi = 2.5$, $\varepsilon = 0.6$, $\delta = 10$, $Pe_m = 15$, $p = 1.5$, and $\omega_{mA} = 0.006$.

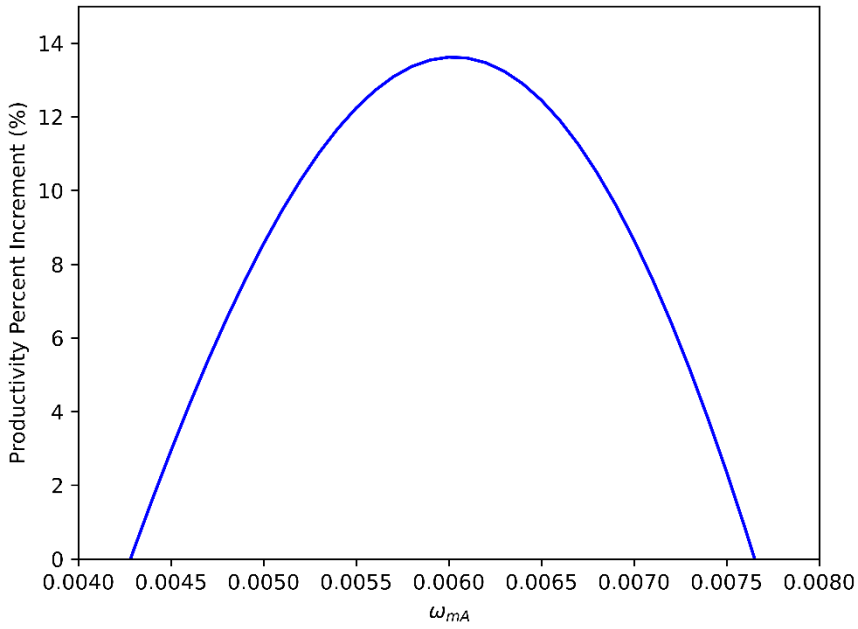

Figure 5.27 Impact of ω_{mA} on the productivity percent increment by keeping $\varphi = 2.5$, $\varepsilon = 0.6$, $\delta = 10$, $Pe_m = 15$, $p = 1.5$, and $\delta_{mA} = 0.99$.

The effect of reaction exponent p and mass Peclet number Pe_m on the productivity percent increment is illustrated in **Figure 5.28** and **Figure 5.29** respectively.

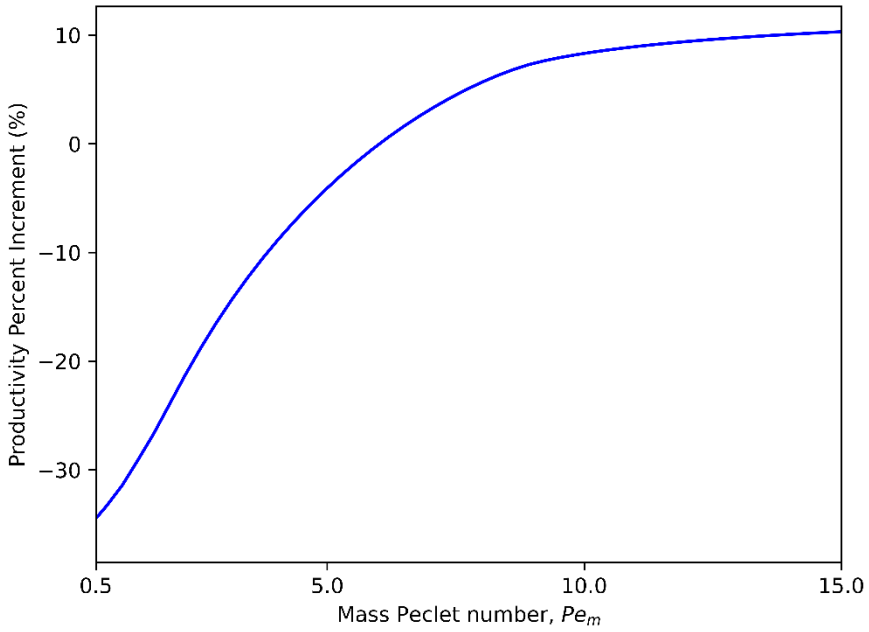

Figure 5.28 Impact of mass Peclet number Pe_m on the productivity percent increment by keeping $\varphi = 2.5$, $\varepsilon = 0.6$, $\delta = 10$, $p = 0.1$, $\delta_{mA} = 0.1$, and $\omega_{mA} = 0.001$.

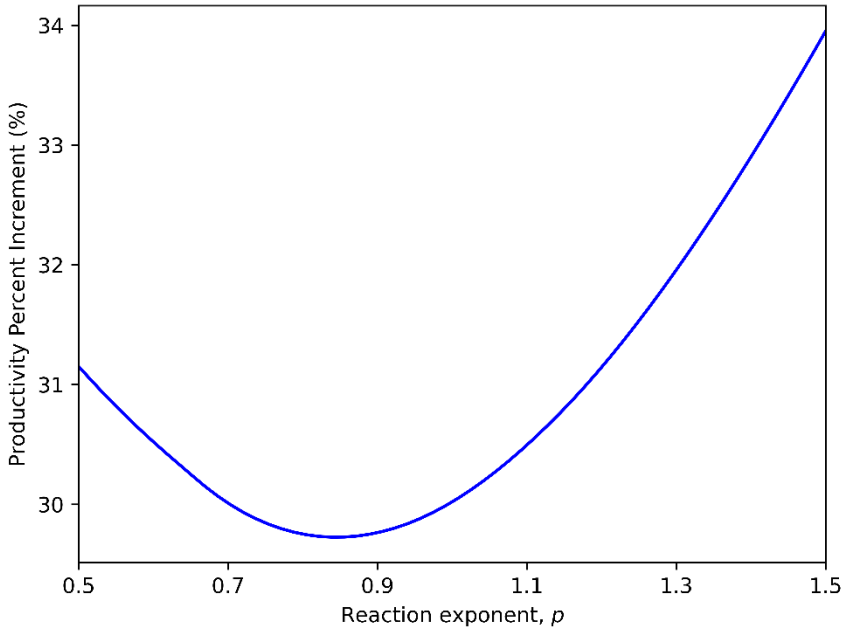

Figure 5.29 Impact of reaction exponent p on the productivity percent increment by keeping $\varphi = 2.5$, $\varepsilon = 0.6$, $\delta = 10$, $Pe_m = 15$, $\delta_{mA} = 0.99$, and $\omega_{mA} = 0.001$.

5.2.2 Unsteady-state non-isothermal conditions for a single reaction

We will now extend our exploration by analyzing the convection-diffusion-reaction problem described by Eqs. (4.36) where *A* transforms into *P* $(A \rightarrow P)$ under unsteady-state, non-isothermal conditions with power-law kinetics.

Concentration and temperature profiles

Figure 5.30 shows the concentration and temperature profiles under unsteady-state non-isothermal conditions for a single reaction.

The presence of multiple colored lines clearly demonstrates the dynamic behavior of the concentration and temperature distribution, each symbolizing a distinct time step. The concentration and temperature vary as time progresses, displaying a transient behavior. The fluctuations in these profiles are attributed to the time-dependent boundary conditions for concentration and temperature, respectively. Understanding these variations is essential for practical applications and process optimization.

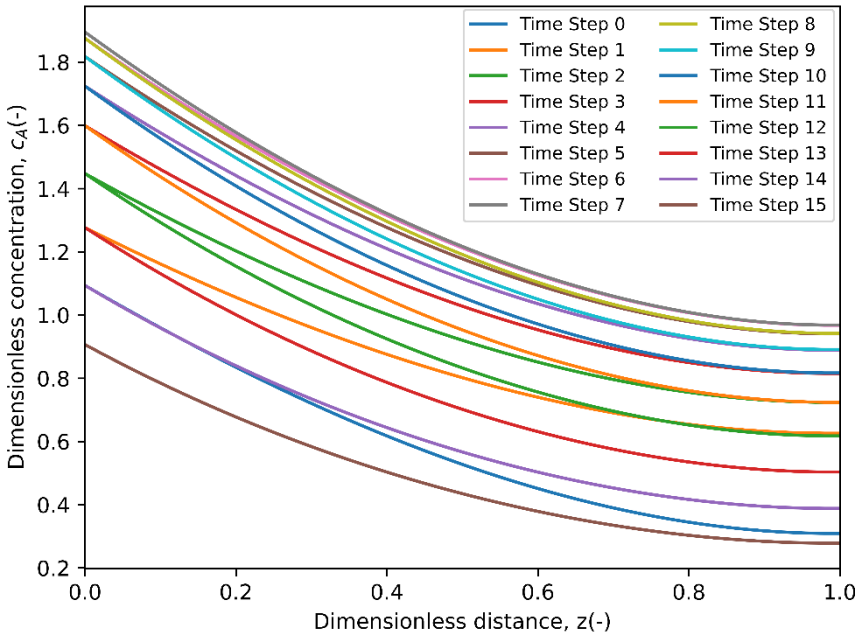

(a)

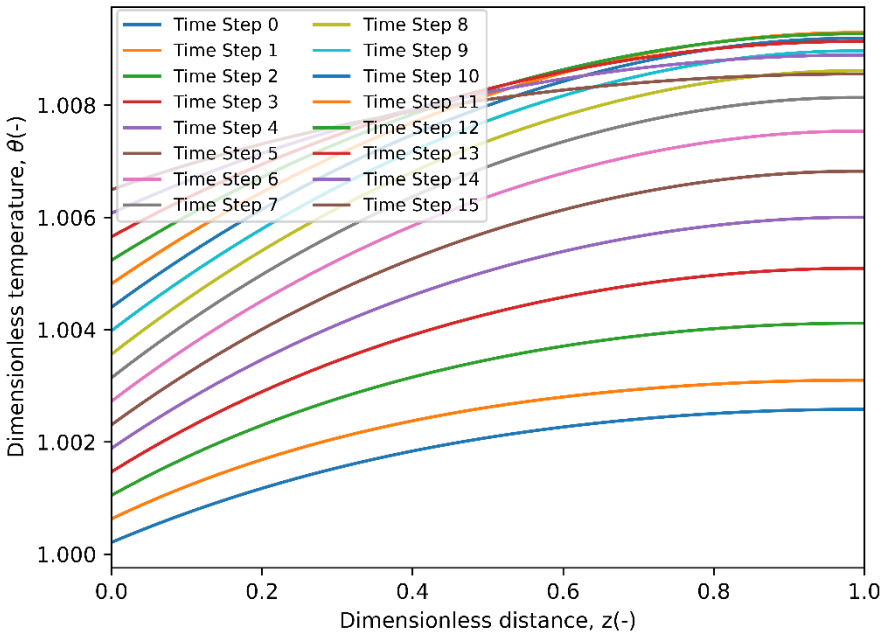

Figure 5.30 (a) Concentration and (b) temperature profiles under unsteady-state isothermal conditions for a single reaction by keeping $Pe_m = Pe_h = 1$, $\varphi = 1.5$, $\varepsilon = 0.6$, $p = 0.5$, $\Omega = 0.8$, $\beta_1 = 0.01$, $\gamma_1 = 10$, $\delta = 90$, $\delta_{mA} = 0.9$, $\omega_{mA} = 0.5$, $\delta_h = 0.2$, and $\omega_h = 0.005$.

Productivity

Table 5.2 provides the maximum productivity values attained by varying parameters under unsteady-state and non-isothermal conditions. The table also encompasses the productivity measurements under steady-state and the corresponding percent increments.

A comparative analysis between **Tables 5.1** and **5.2** reveals that the overall percentage increment is notably lower for non-isothermal conditions compared to isothermal conditions. The highest percent increment in productivity is observed under the conditions where $p = 1.5$ and $Pe_m = 0.5$. The numerical simulations were conducted by varying p, Pe_m, δ_{mA}, and ω_{mA}. The other simulation parameters kept constant are as follows $\varphi = 2.5$, $\varepsilon = 0.6$, $\Omega = 0.8$, $\beta_1 = 0.01$, $\gamma_1 = 10$, $Pe_h = 1$, $\delta_h = 0.2$, $\omega_h = 0.005$ and $\delta = 10$.

Table 5.2 Productivity and percent increment for a single reaction under non-isothermal conditions

p	Pe_m	Max. Productivity (unsteady-state)	Productivity (steady-state)	Percent increment	δ_{mA}	ω_{mA}
0.5	0.1	240.304	239.025	0.54	0.2	2.5e-5
1.0	0.1	222.985	221.081	0.86	0.1	6.25e-6
1.0	0.5	211.304	210.993	0.14	0.1	6.25e-6
1.5	0.1	238.368	217.039	9.83	0.99	2.5e-5
1.5	0.5	229.651	167.879	36.8	0.99	2.5e-5
1.5	1.0	221.667	182.001	21.79	0.99	2.5e-5
1.5	5	238.039	217.325	9.53	0.99	0.001
1.5	10	311.745	280.033	11.32	0.99	0.001
1.5	15	382.164	338.904	12.76	0.99	0.001

5.2.3 Unsteady-state non-isothermal conditions for sequential reaction

In this section, we will extend our investigation by analyzing the problem described by Eqs. (3.30) for the consecutive reaction, i.e., $A \xrightarrow{k_1} B \xrightarrow{k_2} C$ under unsteady-state and non-isothermal conditions. We will examine the concentration profiles of *A* and *B* as well as the temperature profile. Finally, we will compute the productivity of the desired intermediate product *B*.

Figure 5.31 illustrates the concentration profiles of *A* and *B* as well as the temperature profiles under unsteady-state non-isothermal conditions for sequential reaction.

The illustration, featuring multiple colored lines, visually represents the dynamic behavior inherent in the concentration of *A* and the temperature distribution, with each line representing a distinct time step, as illustrated in **Figure 5.31 (a)** and **Figure 5.31 (c)**, respectively. The concentration *A* and temperature vary as time progresses, displaying a

transient behavior. These fluctuations, evident in the profiles, can be attributed to applying time-dependent boundary conditions for the concentration of *A* and temperature, respectively.

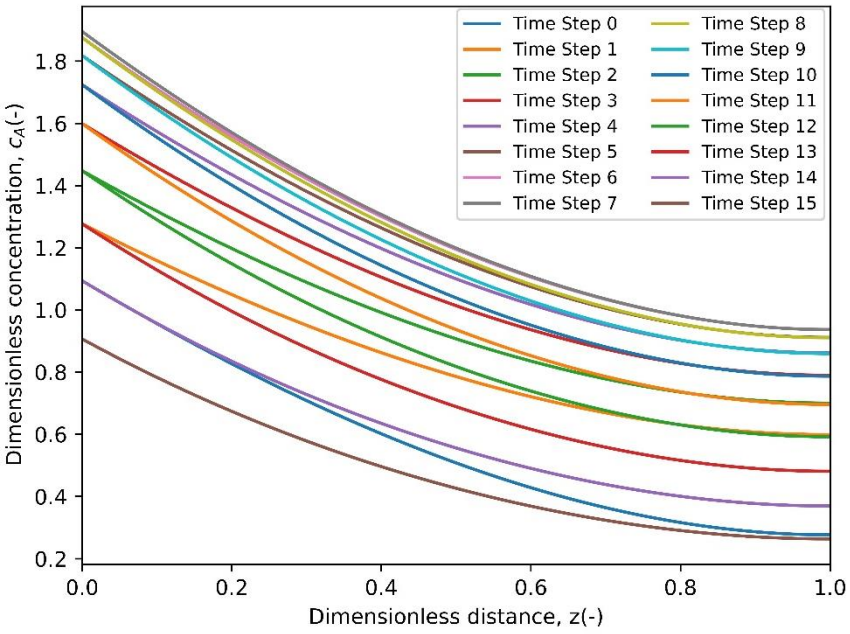

(a) Reactant *A*

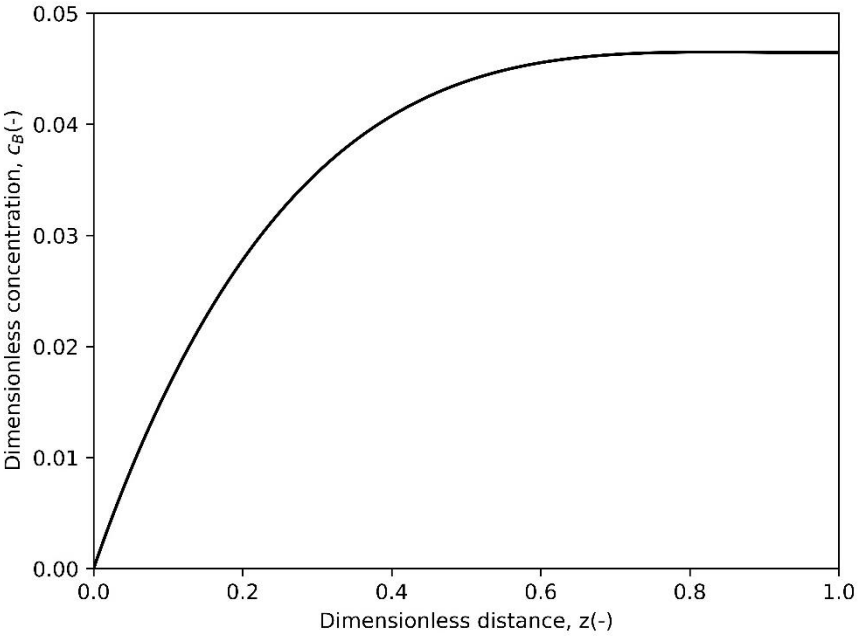

(b) Intermediate product *B*

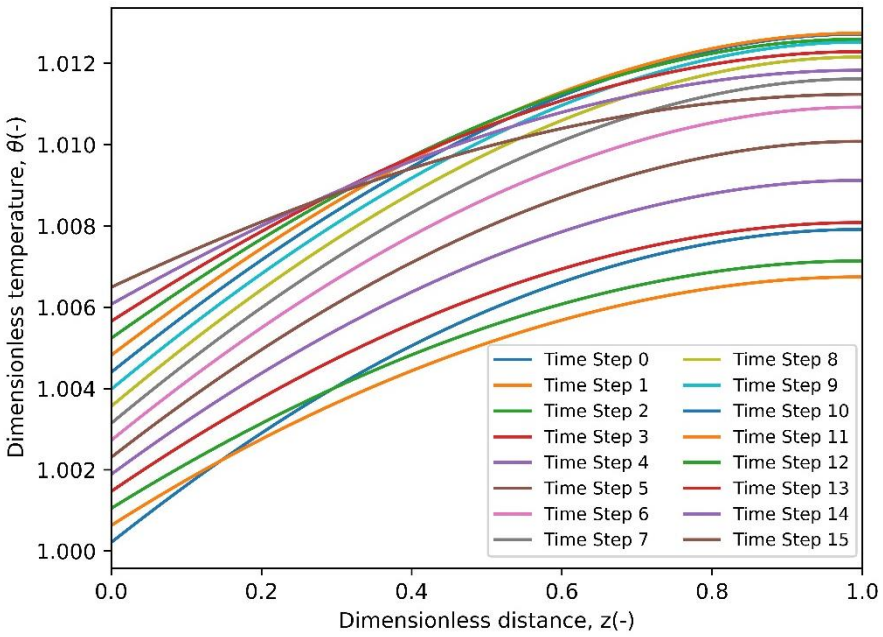

(c) Temperature

Figure 5.31 Unsteady-state profiles of (a) concentration A, (b) concentration B and (c) temperature by keeping $\boldsymbol{Pe_m = Pe_h = 1, \varphi_1 = \varphi_2 = 1.5, \varepsilon = 0.6, p = 0.5, \Omega = 0.8, \beta_1 = 0.01, \beta_2 = 0.01, \gamma_1 = 10, \gamma_2 = 15, \psi = 1, \zeta = 1, \delta_{mA} = 0.9, \delta = 10, \omega_{mA} = 0.5, \delta_h = 0.2}$ ***and*** $\boldsymbol{\omega_h = 0.005}$**.**

It is worth mentioning that the solution for concentration *B*, experiencing no time-dependent boundary conditions, is characterized by a single plot exhibiting an increasing trend across the porous space of the membrane, as depicted in **Figure 5.31 (b)**. Comprehending these intricate variations is essential for practical applications and optimization of associated processes.

Table 5.3 presents the highest achieved productivity values obtained by adjusting parameters in unsteady-state and non-isothermal conditions in the case of a sequential reaction. The table also includes productivity measurements in steady-state and their respective percentage increments. Notably, the most significant percentage increase in productivity is observed in the scenario where $p = 1.5$ and $Pe_m = 0.5$. In this case, the percent increment in productivity is 38.7. The simulations were conducted by varying p, Pe_m, δ_{mA}, and ω_{mA}.

The other simulation parameters that were kept constant are as follows: $\varphi_1 = 2.5$, $\varphi_2 = 2.5$, $\varepsilon = 0.6$, $\Omega = 0.8$, $\beta_1 = \beta_2 = 0.01$, $\gamma_1 = 10$, $\gamma_2 = 15$, $Pe_h = 1$, $\psi = 1$, $\zeta = 1$, $\delta = 90$, $\delta_h = 0.2$, $\omega_h = 0.005$.

Table 5.3 Productivity and percent increment for sequential reaction under non-isothermal conditions

p	Pe_m	Max. Productivity (unsteady-state)	Productivity (steady-state)	Percent increment	δ_{mA}	ω_{mA}
0.5	0.1	349.520	348.024	0.40	0.19	0.001
1.0	0.1	78.573	76.594	2.5	0.19	2.5e-5
1.0	0.5	116.391	115.052	1.2	0.19	2.5e-5
1.5	0.1	421.016	384.397	9.5	0.1	2.5e-5
1.5	0.5	462.689	333.507	38.7	0.81	2.5e-5
1.5	1.0	372.928	300.091	24.3	0.81	2.5e-5
1.5	5	326.562	288.372	13.2	0.81	0.001
1.5	10	415.012	364.702	13.8	0.81	0.001
1.5	15	455.325	398.112	14.4	0.81	0.006

Chapter 6 – Conclusions

The mathematical model for a cylindrical flow-through catalytic membrane reactor was developed and numerically analyzed. The investigated model is based on the system of non-linear diffusion-convection-reaction equations under both isothermal and non-isothermal conditions. Specifically, the model provides insight into the consecutive irreversible exothermic reactions that take place within the porous membrane, where the membrane's pores are impregnated with catalysts. To solve numerically the coupled system of non-linear diffusion-convection-reaction equations, we employed discretization based on the modified Crank-Nicolson scheme. The numerical approach we have developed for the cylindrical model demonstrates stable solutions for dead-core problems, particularly in situations characterized by small reaction exponent and large Thiele modulus.

Through a comprehensive comparison with the previously developed planar model, we have confirmed the convergence and accuracy of our newly proposed cylindrical model, particularly evident at extremely high δ values. Numerical analysis of the effect of the geometric parameter δ revealed a notable alignment between the dead core solutions of the planar and cylindrical geometries as the δ value approached infinity. Significant findings were found in our numerical analysis of model and process parameters on concentration profiles for a single reaction under steady-state. In such case, the dead zones formed when φ surpassed 3. As reaction exponents decreased, concentration profiles were notably affected, resulting in dead zones. It underscores the intricate relationship between reaction kinetics and mass transfer.

Extending our investigation to the steady-state non-isothermal model for a single reaction model has further enhanced our understanding of cylindrical flow-through membrane reactors. Dead-core solutions were obtained at elevated values of Thiele modulus, i.e., $\varphi = 4$. The Prater number affected temperature profiles, emphasizing exothermic and endothermic reactions in the porous membrane system. The temperature profile shifted with greater Prater numbers. The geometry parameter δ significantly impacted reactant *A* consumption and temperature profiles. Higher δ values result in reduced reactant *A* consumption and a higher temperature of the porous membrane system. The effect of mass and heat Peclet number on

concentration and temperature profiles was also examined. A lower mass Peclet number results in a decrease in the concentration profile of reactant *A*. A discernible shift in the temperature profile was observed at higher heat Peclet numbers.

Furthermore, analyzing the model for sequential reaction under varying mass and heat Peclet numbers, Thiele moduli, and reaction exponents provided a comprehensive understanding of the membrane reactor behavior. The parameter study revealed that as the mass Peclet number grows, the concentrations and temperature increase. However, when various heat Peclet numbers are considered, the concentration follows almost the same pattern. The higher temperature values were observed at the lower values of heat Peclet number. It is determined that specific Thiele modulus values exist for the formation of a dead core for each component *A* and *B*. As the Thiele modulus increases, the concentration of *A* falls, and the temperature increases. Moreover, the solution profiles with and without dead-zones were investigated, considering the influence of the reaction exponent.

We also found that the selectivity and yield of our desired product are significantly influenced by convective flow. The variations in mass and heat Peclet numbers significantly improved the performance indices of our membrane reactor. The correlation between heat and mass Peclet numbers and the increased selectivity and yield of the intermediate desired product indicates that the flow conditions can be optimized to improve the reactor's efficiency.

Our investigation into unsteady-state conditions, particularly under isothermal and non-isothermal scenarios for a singular reaction, has provided significant insights into the dynamic behavior of concentration and temperature profiles. Under isothermal conditions, the concentration profiles demonstrate fluctuations over time, influenced by parameters such as δ_{mA} and ω_{mA}. The analysis of productivity reveals substantial percent increments, with optimal conditions identified. Moreover, we investigated concentration and temperature profiles for the non-isothermal model in a single reaction. The productivity analysis under such conditions reveals lower overall percentage increments compared to isothermal conditions. Finally, the study extends to a sequential reaction to explore the concentration profiles of *A* and *B*, temperature profile and optimal conditions for productivity under unsteady-state conditions.

Further investigations for estimating critical Thiele moduli (the threshold value beyond which the dead zones form) and numerical simulations for the 3D coupled system to optimize reactor performance indicators can be topics of future work. Moreover, the optimization of parameters for the unsteady-state model could be considered in future work.

List of References

[1] T. Westermann and T. Melin, “Flow-through catalytic membrane reactors—Principles and applications,” *Chem. Eng. Process. Process Intensif.*, vol. 48, no. 1, pp. 17–28, Jan. 2009, doi: 10.1016/j.cep.2008.07.001.

[2] V. T. Zaspalis, W. Van Praag, K. Keizer, J. G. van Ommen, J. R. H. Ross, and A. J. Burggraaf, “Reactions of methanol over alumina catlytically active membranes modified by silver,” *Appl. Catal.*, vol. 74, no. 2, pp. 235–248, 1991.

[3] A. Julbe, D. Farrusseng, and C. Guizard, “Porous ceramic membranes for catalytic reactors — overview and new ideas,” *J. Memb. Sci.*, vol. 181, no. 1, pp. 3–20, Jan. 2001, doi: 10.1016/S0376-7388(00)00375-6.

[4] K. K. Sirkar, P. V. Shanbhag, and A. S. Kovvali, “Membrane in a Reactor: A Functional Perspective,” *Ind. Eng. Chem. Res.*, vol. 38, no. 10, pp. 3715–3737, Oct. 1999, doi: 10.1021/ie990069j.

[5] A. G. Dixon, “Recent Research in Catalytic Inorganic Membrane Reactors,” *Int. J. Chem. React. Eng.*, vol. 1, no. 1, Dec. 2003, doi: 10.2202/1542-6580.1123.

[6] T. Westermann, E. Kretzschmar, F. Pitsch, and T. Melin, “Heat transfer and temperature profiles in flow-through catalytic membrane reactors,” *Chem. Eng. J.*, vol. 155, no. 1–2, pp. 371–379, Dec. 2009, doi: 10.1016/j.cej.2009.07.059.

[7] B. Golman, K. Shinohara, and M. Kobayashi, “Selectivity and Yield of Exothermic Consecutive Reactions in Catalytically Active Porous Membrane Reactor.,” *J. Chem. Eng. JAPAN*, vol. 30, no. 3, pp. 507–513, 1997, doi: 10.1252/jcej.30.507.

[8] P. Skrzypacz, N. Chalkarova, B. Golman, V. Andreev, and F. Schieweck, “Numerical simulations of dead zone formation in the catalytic flow-through membrane reactor,” *Comput. Chem. Eng.*, vol. 152, p. 107368, Sep. 2021, doi: 10.1016/j.compchemeng.2021.107368.

[9] M. Szukiewicz, E. Chmiel-Szukiewicz, K. Kaczmarski, and A. Szałek, “Dead zone for hydrogenation of propylene reaction carried out on commercial catalyst pellets,” *Open Chem.*, vol. 17, no. 1, pp. 295–301, Jun. 2019, doi: 10.1515/chem-2019-0037.

[10] A. Spence, D. J. Worth, and S. T. Kolaczkowski, “The treatment of non-integer exponents in reaction rate expressions,” *Comput. Chem. Eng.*, vol. 19, no. 11, pp. 1169–1171, Nov. 1995, doi: 10.1016/0098-1354(94)00112-X.

[11] B. Golman, V. V. Andreev, and P. Skrzypacz, “Dead-core solutions for slightly non-isothermal diffusion-reaction problems with power-law kinetics,” *Appl. Math. Model.*, vol. 83, pp. 576–589, Jul. 2020, doi: 10.1016/j.apm.2020.03.016.

[12] V. V. Andreev, “Formation of a ‘dead zone’ in porous structures during processes that proceeding under steady-state and unsteady-state conditions,” *Rev. J. Chem.*, vol. 3, no. 3, pp. 239–269, Jul. 2013, doi: 10.1134/S2079978013030011.

[13] V. V. Andreev, P. Skrzypacz, and B. Golman, “Taylor series solutions to steady-state non-isothermal diffusion–reaction problems for porous catalyst pellets with arbitrary kinetics,” *Math. Methods Appl. Sci.*, vol. 47, no. 3, pp. 1514–1545, Feb. 2024, doi: 10.1002/mma.9699.

[14] K. R. Fowler and C. T. Kelley, “Pseudo-Transient Continuation for Nonsmooth Nonlinear Equations,” *SIAM J. Numer. Anal.*, vol. 43, no. 4, pp. 1385–1406, Jan. 2005, doi: 10.1137/S0036142903431298.

[15] J. Solsvik, S. Tangen, and H. A. Jakobsen, “Evaluation of weighted residual methods for the solution of the pellet equations: The orthogonal collocation, Galerkin, tau and least-squares methods,” *Comput. Chem. Eng.*, vol. 58, pp. 223–259, Nov. 2013, doi: 10.1016/j.compchemeng.2013.07.002.

[16] F. J. Valdes-Parada, M. Sales-Cruz, J. Alberto Ochoa-Tapia, and J. Alvarez-Ramirez, “On Green’s function methods to solve nonlinear reaction–diffusion systems,” *Comput. Chem. Eng.*, vol. 32, no. 3, pp. 503–511, Mar. 2008, doi: 10.1016/j.compchemeng.2007.03.013.
[17] E. M. Lemos, A. R. Secchi, and E. C. Biscaia, “Implementation of Galerkin and moments methods by Gaussian quadrature in advection–diffusion problems with chemical reactions,” *Comput. Chem. Eng.*, vol. 61, pp. 156–174, Feb. 2014, doi: 10.1016/j.compchemeng.2013.11.001.
[18] X. Chen, “A Superlinearly and Globally Convergent Method for Reaction and Diffusion Problems with a Non-Lipschitzian Operator BT - Topics in Numerical Analysis,” G. Alefeld and X. Chen, Eds., Vienna: Springer Vienna, 2001, pp. 79–90.
[19] S. L. Matson and J. A. Quinn, “Membrane Reactors,” in *Membrane Handbook*, Boston, MA: Springer US, 1992, pp. 809–832. doi: 10.1007/978-1-4615-3548-5_43.
[20] J. G. Sanchez Marcano and T. T. Tsotsis, *Catalytic Membranes and Membrane Reactors*. Wiley, 2002. doi: 10.1002/3527601988.
[21] T. Westermann, “Flow-through membrane microreactor for intensified heterogeneous catalysis.” Citeseer, 2009.
[22] W. J. Koros, Y. H. Ma, and T. Shimidzu, “Terminology for membranes and membrane processes (IUPAC Recommendations 1996),” *Pure Appl. Chem.*, vol. 68, no. 7, pp. 1479–1489, Jan. 1996, doi: 10.1351/pac199668071479.
[23] G. Saracco and V. Specchia, “Catalytic Inorganic-Membrane Reactors: Present Experience and Future Opportunities,” *Catal. Rev.*, vol. 36, no. 2, pp. 305–384, May 1994, doi: 10.1080/01614949408013927.
[24] J. Coronas and J. Santamaría, “Catalytic reactors based on porous ceramic membranes,” *Catal. Today*, vol. 51, no. 3–4, pp. 377–389, Jul. 1999, doi: 10.1016/S0920-5861(99)00090-5.
[25] S.-T. Hwang, “Inorganic membranes and membrane reactors,” *Korean J. Chem. Eng.*, vol. 18, no. 6, pp. 775–787, Nov. 2001, doi: 10.1007/BF02705597.
[26] A. Basile and F. Gallucci, *Membranes for membrane reactors: preparation, optimization and selection*. John Wiley & Sons, 2010.
[27] A. Seidel-Morgenstern, *Membrane reactors: distributing reactants to improve selectivity and yield*. John Wiley & Sons, 2010.
[28] S. Miachon and J.-A. Dalmon, “Catalysis in Membrane Reactors: What About the Catalyst?,” *Top. Catal.*, vol. 29, no. 1, pp. 59–65, 2004, doi: 10.1023/B:TOCA.0000024928.63811.8b.
[29] L. van Dyk, S. Miachon, L. Lorenzen, M. Torres, K. Fiaty, and J.-A. Dalmon, “Comparison of microporous MFI and dense Pd membrane performances in an extractor-type CMR,” *Catal. Today*, vol. 82, no. 1–4, pp. 167–177, Jul. 2003, doi: 10.1016/S0920-5861(03)00229-3.
[30] S. Bénard, A. Giroir-Fendler, P. Vernoux, N. Guilhaume, and K. Fiaty, “Comparing monolithic and membrane reactors in catalytic oxidation of propene and toluene in excess of oxygen,” *Catal. Today*, vol. 156, no. 3–4, pp. 301–305, Oct. 2010, doi: 10.1016/j.cattod.2010.07.019.
[31] T. Westermann, N. Kopriwa, A. Schröder, and T. Melin, “Effective dispersion model for flow-through catalytic membrane reactors combining axial dispersion and pore size distribution,” *Chem. Eng. Sci.*, vol. 65, no. 5, pp. 1609–1615, Mar. 2010, doi: 10.1016/j.ces.2009.10.023.
[32] R. Dittmeyer, K. Svajda, and M. Reif, “A Review of Catalytic Membrane Layers for Gas/Liquid Reactions,” *Top. Catal.*, vol. 29, no. 1/2, pp. 3–27, May 2004, doi: 10.1023/B:TOCA.0000024925.30020.a1.

[33] M. Kobayashi, J. Togawa, T. Kanno, J. Horiuchi, and K. Tada, “Comparing kinetic design of propene partial oxidation between a Cs Ag and a Re Ag immobilized membrane reactors,” *Desalination*, vol. 144, no. 1–3, pp. 399–403, Sep. 2002, doi: 10.1016/S0011-9164(02)00350-8.
[34] W. Shi *et al.*, “Continuous esterification to produce biodiesel by SPES/PES/NWF composite catalytic membrane in flow-through membrane reactor: Experimental and kinetic studies,” *Bioresour. Technol.*, vol. 129, pp. 100–107, Feb. 2013, doi: 10.1016/j.biortech.2012.10.039.
[35] A. Schmidt *et al.*, “A pore-flow-through membrane reactor for partial hydrogenation of 1,5-cyclooctadiene,” *AIChE J.*, vol. 54, no. 1, pp. 258–268, Jan. 2008, doi: 10.1002/aic.11379.
[36] A. Schmidt, R. Haidar, and R. Schomäcker, “Selectivity of partial hydrogenation reactions performed in a pore-through-flow catalytic membrane reactor,” *Catal. today*, vol. 104, no. 2–4, pp. 305–312, 2005.
[37] C. R. F. Lund, “Improving selectivity during methane partial oxidation by use of a membrane reactor,” *Catal. Letters*, vol. 12, no. 4, pp. 395–403, 1992, doi: 10.1007/BF00765070.
[38] M. Reif and R. Dittmeyer, “Porous, catalytically active ceramic membranes for gas–liquid reactions: a comparison between catalytic diffuser and forced through flow concept,” *Catal. Today*, vol. 82, no. 1–4, pp. 3–14, Jul. 2003, doi: 10.1016/S0920-5861(03)00197-4.
[39] C. Regmi, S. Lotfi, J. C. Espíndola, K. Fischer, A. Schulze, and A. I. Schäfer, “Comparison of Photocatalytic Membrane Reactor Types for the Degradation of an Organic Molecule by TiO2-Coated PES Membrane,” *Catalysts*, vol. 10, no. 7, p. 725, Jun. 2020, doi: 10.3390/catal10070725.
[40] J. Miao *et al.*, “Continuous and complete conversion of high concentration p -nitrophenol in a flow-through membrane reactor,” *AIChE J.*, vol. 65, no. 9, Sep. 2019, doi: 10.1002/aic.16692.
[41] M. I. Temkin, “Diffusion effects during the reaction on the surface pores of a spherical catalyst particle,” *Kinet. Catal*, vol. 16, pp. 104–112, 1975.
[42] F. M. Pereira and S. C. Oliveira, “Occurrence of dead core in catalytic particles containing immobilized enzymes: analysis for the Michaelis–Menten kinetics and assessment of numerical methods,” *Bioprocess Biosyst. Eng.*, vol. 39, no. 11, pp. 1717–1727, Nov. 2016, doi: 10.1007/s00449-016-1647-0.
[43] Z. Wang, J. Ma, C. Y. Tang, K. Kimura, Q. Wang, and X. Han, “Membrane cleaning in membrane bioreactors: A review,” *J. Memb. Sci.*, vol. 468, pp. 276–307, Oct. 2014, doi: 10.1016/j.memsci.2014.05.060.
[44] A. Drews, “Membrane fouling in membrane bioreactors—Characterisation, contradictions, cause and cures,” *J. Memb. Sci.*, vol. 363, no. 1–2, pp. 1–28, Nov. 2010, doi: 10.1016/j.memsci.2010.06.046.
[45] C. M. Kao, B. M. Yang, R. Y. Surampalli, and T. C. Zhang, “Limitation of Membrane Technology and Prevention of Membrane Fouling,” in *Membrane Technology and Environmental Applications*, Reston, VA: American Society of Civil Engineers, 2012, pp. 504–532. doi: 10.1061/9780784412275.ch17.
[46] J. Zhang, H. C. Chua, J. Zhou, and A. G. Fane, “Factors affecting the membrane performance in submerged membrane bioreactors,” *J. Memb. Sci.*, vol. 284, no. 1–2, pp. 54–66, Nov. 2006, doi: 10.1016/j.memsci.2006.06.022.
[47] E. Drioli, “Membrane reactors,” *Chem. Eng. Process. Process Intensif.*, vol. 43, no. 9, pp. 1101–1102, Sep. 2004, doi: 10.1016/j.cep.2004.04.002.
[48] M. Huuhtanen, P. K. Seelam, T. Kolli, E. Turpeinen, and R. L. Keiski, “Advances in

catalysts for membrane reactors," in *Handbook of Membrane Reactors*, Elsevier, 2013, pp. 401–432. doi: 10.1533/9780857097330.2.401.
[49] E. S. Martinsen *et al.*, "Modeling and Simulation of a Single Catalytic Fixed Bed in an Ammonia Reactor," *IFAC-PapersOnLine*, vol. 56, no. 2, pp. 6906–6912, 2023, doi: 10.1016/j.ifacol.2023.10.497.
[50] G. D. Smith, *Numerical solution of partial differential equations: finite difference methods*. Oxford university press, 1985.
[51] L. Chin and T. Dutta, *NumPy essentials*. Packt Publishing, Limited, 2016.
[52] B. Kruczek, "Convective Transport," in *Encyclopedia of Membranes*, Berlin, Heidelberg: Springer Berlin Heidelberg, 2015, pp. 1–3. doi: 10.1007/978-3-642-40872-4_1994-1.
[53] Y. Gu *et al.*, "Catalytic membrane reactor for Suzuki-Miyaura C−C cross-coupling: Explanation for its high efficiency via modeling," *AIChE J.*, vol. 63, no. 2, pp. 698–704, Feb. 2017, doi: 10.1002/aic.15379.
[54] H. S. Fogler, *Elements of chemical reaction engineering*. Third edition. Upper Saddle River, N.J. : Prentice Hall PTR, [1999] ©1999. [Online]. Available: https://search.library.wisc.edu/catalog/999810177702121
[55] M. Murmura, S. Cerbelli, and M. Annesini, "Modeling Fixed Bed Membrane Reactors for Hydrogen Production through Steam Reforming Reactions: A Critical Analysis," *Membranes (Basel).*, vol. 8, no. 2, p. 34, Jun. 2018, doi: 10.3390/membranes8020034.
[56] M. Abramowitz and I. A. Stegun, *Handbook of Mathematical Functions: With Formulas, Graphs, and Mathematical Tables*. in Applied mathematics series. Dover Publications, 1965. [Online]. Available: https://books.google.kz/books?id=MtU8uP7XMvoC
[57] R. Hazrat, *Mathematica®: A Problem-Centered Approach*. in Springer Undergraduate Mathematics Series. Cham: Springer International Publishing, 2015. doi: 10.1007/978-3-319-27585-7.

Appendices

Appendix A. Analytical solutions of planar and cylindrical models

The analytic solution to the two-point boundary value problem for the linear Eqs. (4.1) and (4.2) is given as:

$$c(z) = e^{\frac{Pe_m - \sqrt{Pe_m^2 + 4\varphi^2}}{2} z} \cdot \frac{M_{z,Pe_m,\varphi,\delta}}{N_{Pe_m,\varphi,\delta}}, \tag{A.1}$$

where

$$\begin{aligned}
M_{z,Pe_m,\varphi,\delta} = {} & Pe_m \cdot \mathcal{U}\left[P_{Pe_m,\varphi}, 1, Q_{z,Pe_m,\varphi,\delta}\right] \mathcal{L}\left[-P_{Pe_m,\varphi},\ Q_{1,Pe_m,\varphi,\delta}\right] \\
& - S_{Pe_m,\varphi,1} \cdot \mathcal{U}\left[P_{Pe_m,\varphi}, 1, Q_{z,Pe_m,\varphi,\delta}\right] \mathcal{L}\left[-P_{Pe_m,\varphi},\ Q_{1,Pe_m,\varphi,\delta}\right] \\
& - Pe_m \cdot \mathcal{U}\left[P_{Pe_m,\varphi}, 1, Q_{1,Pe_m,\varphi,\delta}\right] \mathcal{L}\left[-P_{Pe_m,\varphi},\ Q_{z,Pe_m,\varphi,\delta}\right] \\
& + S_{Pe_m,\varphi,1} \cdot \mathcal{U}\left[P_{Pe_m,\varphi}, 1, Q_{1,Pe_m,\varphi,\delta}\right] \mathcal{L}\left[-P_{Pe_m,\varphi},\ Q_{z,Pe_m,\varphi,\delta}\right] \\
& + Pe_m \cdot \mathcal{U}\left[1 + P_{Pe_m,\varphi}, 2, Q_{1,Pe_m,\varphi,\delta}\right] \mathcal{L}\left[-P_{Pe_m,\varphi},\ Q_{z,Pe_m,\varphi,\delta}\right] \\
& + S_{Pe_m,\varphi,1} \cdot \mathcal{U}\left[1 + P_{Pe_m,\varphi}, 2, Q_{1,Pe_m,\varphi,\delta}\right] \mathcal{L}\left[-P_{Pe_m,\varphi},\ Q_{z,Pe_m,\varphi,\delta}\right] \\
& - 2 \cdot S_{Pe_m,\varphi,1} \cdot \mathcal{U}\left[P_{Pe_m,\varphi}, 1, Q_{z,Pe_m,\varphi,\delta}\right] \mathcal{L}\left[-1 - P_{Pe_m,\varphi},\ 1,\ Q_{1,Pe_m,\varphi,\delta}\right],
\end{aligned}$$

$$\begin{aligned}
N_{Pe_m,\varphi,\delta} = {} & - Pe_m \cdot \mathcal{U}\left[P_{Pe_m,\varphi}, 1, Q_{1,Pe_m,\varphi,\delta}\right] \mathcal{L}\left[-P_{Pe_m,\varphi},\ S_{Pe_m,\varphi,\delta}\right] \\
& + S_{Pe_m,\varphi,1} \cdot \mathcal{U}\left[P_{Pe_m,\varphi}, 1, Q_{1,Pe_m,\varphi,\delta}\right] \mathcal{L}\left[-P_{Pe_m,\varphi},\ S_{Pe_m,\varphi,\delta}\right] \\
& + Pe_m \cdot \mathcal{U}\left[1 + P_{Pe_m,\varphi}, 2, Q_{1,Pe_m,\varphi,\delta}\right] \mathcal{L}\left[-P_{Pe_m,\varphi},\ S_{Pe_m,\varphi,\delta}\right] \\
& + S_{Pe_m,\varphi,1} \cdot \mathcal{U}\left[1 + P_{Pe_m,\varphi}, 2, Q_{1,Pe_m,\varphi,\delta}\right] \mathcal{L}\left[-P_{Pe_m,\varphi},\ S_{Pe_m,\varphi,\delta}\right] \\
& + Pe_m \cdot \mathcal{U}\left[P_{Pe_m,\varphi}, 1, S_{Pe_m,\varphi,\delta}\right] \mathcal{L}\left[-P_{Pe_m,\varphi},\ Q_{1,Pe_m,\varphi,\delta}\right] \\
& - S_{Pe_m,\varphi,1} \cdot \mathcal{U}\left[P_{Pe_m,\varphi}, 1, S_{Pe_m,\varphi,\delta}\right] \mathcal{L}\left[-P_{Pe_m,\varphi},\ Q_{1,Pe_m,\varphi,\delta}\right] \\
& - 2 \cdot S_{Pe_m,\varphi,1} \cdot \mathcal{U}\left[P_{Pe_m,\varphi}, 1, S_{Pe_m,\varphi,\delta}\right] \mathcal{L}\left[-1 - P_{Pe_m,\varphi},\ 1,\ Q_{1,Pe_m,\varphi,\delta}\right],
\end{aligned}$$

and

$$P_{Pe_m,\varphi} = \frac{Pe_m + \sqrt{{Pe_m}^2 + 4\varphi^2}}{2\sqrt{{Pe_m}^2 + 4\varphi^2}} ,$$

$$Q_{z,Pe_m,\varphi,\delta} = (z+\delta)\sqrt{{Pe_m}^2 + 4\varphi^2} ,$$

$$S_{Pe_m,\varphi,\delta} = \delta\sqrt{{Pe_m}^2 + 4\varphi^2} .$$

Here, $\mathcal{U}$ and $\mathcal{L}$ denote the confluent hypergeometric function of the second kind and generalized Laguerre polynomials, respectively.

The confluent hypergeometric function of the second kind, also known as Tricomi's confluent hypergeometric function, is defined for $a, z > 0$ as [56].

$$U[a,b,z] = \frac{1}{\Gamma(a)} \int_0^\infty e^{-zt} t^{a-1} (1+t)^{b-a-1} dt ,$$

where $\Gamma(t)$ denotes the Gamma function. The associated Laguerre polynomials $\mathcal{L}[n,a,z]$ are set of L_2 orthogonal polynomials of degree n with respect to the weight function $z^a e^{-z}$. They satisfy the following orthogonality relation

$$\int_0^\infty e^{-t} t^a \mathcal{L}[n,a,z] \mathcal{L}[m,a,z] dt = \begin{cases} 0 & \text{if } n \neq m , \\ \dfrac{\Gamma(a+n+1)}{n!} & \text{if } n = m . \end{cases}$$

A generalization of the associated Laguerre polynomials to not necessarily integers is called a generalized Laguerre function [56]. These generalized Laguerre functions can be defined as

$$\mathcal{L}[n,a,z] = \binom{n+a}{a} {}_1F_1[-n, a+1, z] ,$$

where $\binom{n+a}{a}$ denotes the generalized binomial coefficient, and confluent hypergeometric function of the first kind is given as:

$${}_1F_1[n,a,z] = \frac{\Gamma(a)}{\Gamma(a-n)\Gamma(n)} \int_0^1 e^{zt} t^{n-1} (1-t)^{a-n-1} dt$$

For non-negative integer values of *n*, the generalized Laguerre function returns the generalized Laguerre polynomials.

The analytical solution of Eq. (A.1) was computed symbolically by Mathematica® [57].

If $\delta \to \infty$, then the analytical solution for the planar geometry is given as [8].

$$c(z) = \mathrm{e}^{\frac{Pe_m - \sqrt{Pe_m^2 + 4\varphi^2}}{2} z} \frac{1 + \left(\frac{Pe_m - \sqrt{Pe_m^2 + 4\varphi^2}}{2\varphi}\right)^2 \mathrm{e}^{-\sqrt{Pe_m^2 + 4\varphi^2}} \mathrm{e}^{\sqrt{Pe_m^2 + 4\varphi^2} z}}{1 + \left(\frac{Pe_m - \sqrt{Pe_m^2 + 4\varphi^2}}{2\varphi}\right)^2 \mathrm{e}^{-\sqrt{Pe_m^2 + 4\varphi^2}}}. \quad \text{(A.2)}$$

By comparing the analytical solutions for our cylindrical geometry, as given in Eq. (A.1), with the solution for the planar case, as represented by Eq. (A.2), we observe that the profiles of these two solutions overlap at $\delta = 10$, as shown in **Figure A.1**. The parameters used for this comparison are $\varphi = 4$, $Pe_m = 1$, and $p = 1$.

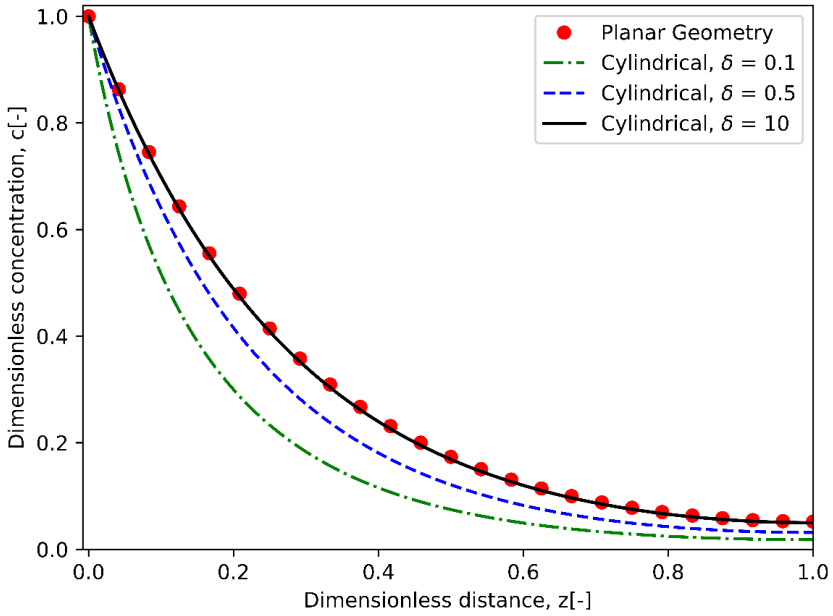

Figure A.1 Analytical solutions for planar and cylindrical geometry by keeping $\varphi = 4, Pe_m = 1, and\ p = 1$

Appendix B. Derivation of dimensional & dimensionless model equations

B.1. Mass balance for Component *A*

To obtain the mass balance equation for component *A*, we begin by considering the steady-state mass balance equation over a cylindrical shell given as follows:

$$\begin{aligned}&(\text{Rate of input of specie } A \text{ by diffusion and flow at } r \text{ in moles/time}) - \\ &(\text{Rate of output of specie } A \text{ by diffusion and flow at } r+\Delta r \text{ in moles/time}) + \\ &(\text{Rate of generation of species } A \text{ by reaction within } \Delta r \text{ in moles/time}) = 0\end{aligned} \tag{B.1}$$

The total molar flux of the component *A* through the porous medium of the membrane is a combination of molar fluxes by diffusion and convection given as follows:

$$j_{A,\text{tot}} = j_{A,\text{diff}} + j_{A,conv}. \tag{B.2}$$

Diffusion and convection molar fluxes for component *A* are defined by the subsequent equations, respectively.

$$j_{A,\text{diff}} = -D_{A,\text{eff}}\frac{dC_A}{dr}, \tag{B.3}$$

$$j_{A,conv} = u_D C_A \tag{B.4}$$

where u_D is the filter velocity (also known as the Darcian fluid velocity) which is already described previously.

The rate of generation within a cylindrical differential volume element is given by:

$$R_A \cdot 2\pi r h\,\Delta r \tag{B.5}$$

where R_A represents the rate of reaction of component *A*, i.e., $R_A = -r_1$ which is further defined according to Eq. (3.2).

Introducing Eqs. (B.2) and (B.5) into Eq. (B.1), the mass balance equation for component *A* becomes:

$$(j_{A,\text{tot}} \cdot 2\pi r h)|_r - (j_{A,\text{tot}} \cdot 2\pi r h)|_{r+\Delta r} + R_A \cdot 2\pi r h\,\Delta r = 0 \tag{B.6}$$

Dividing Eq. (B.6) by $2\pi r h$, subsequent rearrangement, and consideration of the limit as $\Delta r \to 0$ yields:

$$\frac{1}{r}\frac{d(j_{A,\mathrm{tot}}\cdot r)}{dr} - R_A = 0 \tag{B.7}$$

Introducing the value of $j_{A,\mathrm{tot}}$ from Eq. (B.2) while using Eqs. (B.3) and (B.4) into Eq. (B.7), we obtain the following differential equation for the mass balance.

$$\frac{1}{r}\frac{d}{dr}\left(\left(-D_{A,\mathrm{eff}}\frac{dC_A}{dr}+u_D C_A\right)\cdot r\right) - R_A = 0 \tag{B.8}$$

Now, taking the constant terms out of the derivative and rearranging, then Eq. (B.8) becomes:

$$-D_{A,\mathrm{eff}}\frac{d}{dr}\left(r\frac{dC_A}{dr}\right)+u_D\frac{d}{dr}(rC_A)-R_A\cdot r=0. \tag{B.9}$$

By rearranging Eq. (B.9), we get the following equation:

$$D_{A,\mathrm{eff}}\frac{d^2C_A}{dr^2}+\left(\frac{D_{A,\mathrm{eff}}}{r}-u_D\right)\frac{dC_A}{dr}+\left(R_A-\frac{u_D}{r}C_A\right) = 0 \tag{B.10}$$

Introducing the term R_A by utilizing Eqs. (3.2) (3.12) and (3.13) into Eq. (B.10), we obtain the mass balance equation for component *A* under non-isothermal conditions with power-law kinetics and temperature-dependent Arrhenius constant.

$$D_{A,\mathrm{eff}}\frac{d^2C_A}{dr^2}+\left(\frac{D_{A,\mathrm{eff}}}{r}-u_D\right)\frac{dC_A}{dr}-k_{1,0}\cdot\exp\left(\frac{-E_1}{R_G}\left(\frac{1}{T}-\frac{1}{T_0}\right)\right){C_A}^{p_1}-\frac{u_D}{r}C_A = 0 \tag{B.11}$$

In order to obtain the dimensionless form of Eq. (B.11) , the first derivative of the concentration with respect to radial position, $\frac{dC_A}{dr}$, can be expanded by using the chain rule of differentiation as follows:

$$\frac{dC_A}{dr}=\frac{dC_A}{dz}\cdot\frac{dz}{dr}=\frac{dC_A}{dc_A}\cdot\frac{dc_A}{dz}\cdot\frac{dz}{dr} \tag{B.12}$$

where $z=\frac{r-r_{in}}{L}$ and $c_A=\frac{C_A}{C_{A0}}$. The terms in Eq. (B.12) can be further simplified as follows:

$$\frac{dC_A}{dc_A}=\frac{d(c_A\cdot C_{A0})}{dc_A}=C_{A0} \tag{B.13}$$

$$\frac{dz}{dr} = \frac{d}{dr}\left(\frac{r - r_{in}}{L}\right) = \frac{1}{L}\left(\frac{dr}{dr} - \frac{dr_{in}}{dr}\right) = \frac{1}{L} \tag{B.14}$$

Substituting Eqs. (B.13) and (B.14) into Eq. (B.12), yields:

$$\frac{dC_A}{dr} = C_{A0} \cdot \frac{dc_A}{dz} \cdot \frac{1}{L} = \frac{C_{A0}}{L}\,\frac{dc_A}{dz} \tag{B.15}$$

Now, taking the derivative of Eq. (B.15), we get:

$$\begin{gathered}\frac{d^2C_A}{dr^2} = \frac{d}{dr}\left(\frac{C_{A0}}{L}\,\frac{dc_A}{dz}\right) = \frac{C_{A0}}{L}\,\frac{d}{dr}\left(\frac{dc_A}{dz}\right) = \\ \frac{C_{A0}}{L}\,\frac{d}{dz}\left(\frac{dc_A}{dz}\right)\frac{dz}{dr} = \frac{C_{A0}}{L}\,\frac{d^2c_A}{dz^2}\,\frac{dz}{dr}\end{gathered} \tag{B.16}$$

Putting the value of $\frac{dz}{dr}$ from Eq. (B.14) into Eq. (B.16), yields:

$$\frac{d^2C_A}{dr^2} = \frac{C_{A0}}{L^2}\,\frac{d^2c_A}{dz^2} \tag{B.17}$$

Introducing Eqs. (B.15) and (B.17) into Eq. (B.11) and converting terms C_A and ${C_A}^{p_1}$ into dimensionless forms, we get:

$$\begin{gathered}D_{A,\text{eff}}\left(\frac{C_{A0}}{L^2}\,\frac{d^2c_A}{dz^2}\right) + \left(\frac{D_{A,\text{eff}}}{r} - u_D\right)\left(\frac{C_{A0}}{L}\,\frac{dc_A}{dz}\right) - k_{1,0} \cdot \exp\left(\frac{-E_1}{R_G}\left(\frac{1}{T} - \frac{1}{T_0}\right)\right)(c_A \cdot C_{A0})^{p_1} \\ - \frac{u_D}{r}(c_A \cdot C_{A0}) = 0\end{gathered} \tag{B.18}$$

Dividing Eq. (B.18) by $\frac{D_{A,\text{eff}}C_{A0}}{L^2}$ and rearranging results in:

$$\begin{gathered}\frac{d^2c_A}{dz^2} + \left(\frac{1}{\frac{r_{in}}{L} + z} - \frac{u_D L}{D_{A,\text{eff}}}\right)\frac{dc_A}{dz} - \frac{k_{1,0}L^2}{D_{A,\text{eff}}C_{A0}} \cdot \exp\left(\frac{-E_1}{R_G}\left(\frac{1}{T} - \frac{1}{T_0}\right)\right)(c_A \cdot C_{A0})^{p_1} - \\ \frac{u_D\ L}{D_{A,\text{eff}}C_{A0}\left(\frac{r_{in}}{L} + z\right)}(c_A \cdot C_{A0}) = 0\end{gathered} \tag{B.19}$$

Introducing the dimensionless parameters from **Table 3.1** into Eq. (B.19) and the geometry parameter $\delta = \frac{r_{in}}{L}$, we get the final dimensionless mass balance equation for component *A*.

$$\frac{d^2 c_A}{dz^2} + \left(\frac{1}{\delta + z} - Pe_m\right)\frac{dc_A}{dz} - {\varphi_1}^2 \cdot \exp\left(\gamma_1\left(1 - \frac{1}{\theta}\right)\right){c_A}^{p_1} - \frac{Pe_m}{\delta + z}c_A \;=\; 0 \quad \text{(B.20)}$$

In case of isothermal conditions i.e., $\theta = 1$ and linear kinetics, Eq. (B.20) becomes:

$$\frac{d^2 c_A}{dz^2} + \left(\frac{1}{\delta + z} - Pe_m\right)\frac{dc_A}{dz} - \left({\varphi_1}^2 + \frac{Pe_m}{\delta + z}\right)c_A \;=\; 0 \quad \text{(B.21)}$$

Similarly, in case of isothermal conditions and power-law kinetics, Eq. (B.20) becomes

$$\frac{d^2 c_A}{dz^2} + \left(\frac{1}{\delta + z} - Pe_m\right)\frac{dc_A}{dz} - {\varphi_1}^2 {c_A}^{p_1} - \frac{Pe_m}{\delta + z}c_A \;=\; 0 \quad \text{(B.22)}$$

B.2. Mass balance for component *B*

By employing the similar procedures as described in the preceding section, the mass balance equation for component *B* can be derived as follows:

$$\frac{1}{r}\frac{d(j_{B,\text{tot}} \cdot r)}{dr} \;+\; R_B \;=\; 0 \quad \text{(B.23)}$$

The total molar flux of the component *B* through the porous medium of the membrane is defined in a similar way as follows:

$$\begin{aligned} j_{B,\text{tot}} &= j_{B,\text{diff}} + j_{B,conv} \\ j_{B,\text{tot}} &= -D_{B,\text{eff}}\frac{dC_B}{dr} + u_D C_B \end{aligned} \quad \text{(B.24)}$$

The rate of reaction of component *B* is defined as $R_B = r_1 - r_2$ where $r_1 = -k_1 {C_A}^{p_1}$ and $r_2 = k_2 {C_B}^{p_2}$.

According to Arrhenius Equation, the rate constants are defined as follows:

$$
\begin{aligned}
k_1 &= k_{1,0} \cdot \exp\left(-\frac{E_1}{R_G}\left(\frac{1}{T}-\frac{1}{T_0}\right)\right), \\
k_2 &= k_{2,0} \cdot \exp\left(-\frac{E_2}{R_G}\left(\frac{1}{T}-\frac{1}{T_0}\right)\right)
\end{aligned}
\tag{B.25}
$$

Introducing Eq. (B.24) into Eq. (B.23), yields:

$$
\frac{1}{r}\frac{d}{dr}\left(\left(-D_{B,\text{eff}}\frac{dC_B}{dr}+u_D C_B\right)\cdot r\right) + R_B = 0 \tag{B.26}
$$

Now, taking the constant terms out of the derivative and rearranging, then Eq. (B.26) becomes:

$$
-D_{B,\text{eff}}\frac{d}{dr}\left(r\frac{dC_B}{dr}\right)+u_D\frac{d}{dr}(rC_B)+R_B\cdot r=0\,. \tag{B.27}
$$

By rearranging Eq. (B.27), we get the following equation:

$$
D_{B,\text{eff}}\frac{d^2C_B}{dr^2}+\left(\frac{D_{B,\text{eff}}}{r}-u_D\right)\frac{dC_B}{dr}+\left(-R_B-\frac{u_D}{r}C_B\right) = 0 \tag{B.28}
$$

Introducing the term R_B and utilizing Eq. (B.25) into Eq. (B.28), we obtain the mass balance equation for component *B* under non-isothermal conditions with power-law kinetics and temperature-dependent Arrhenius constant.

$$
\begin{aligned}
D_{B,\text{eff}}\frac{d^2C_B}{dr^2}+\left(\frac{D_{B,\text{eff}}}{r}-u_D\right)\frac{dC_B}{dr}+k_{1,0}\cdot\exp\left(\frac{-E_1}{R_G}\left(\frac{1}{T}-\frac{1}{T_0}\right)\right){C_A}^{p_1} \\
-\ k_{2,0}\cdot\exp\left(\frac{-E_2}{R_G}\left(\frac{1}{T}-\frac{1}{T_0}\right)\right){C_B}^{p_2}-\frac{u_D}{r}C_B = 0
\end{aligned}
\tag{B.29}
$$

In order to obtain the dimensionless form of Eq. (B.29) , the first derivative can be expanded by using the chain rule of differentiation as follows:

$$
\frac{dC_B}{dr}=\frac{dC_B}{dz}\cdot\frac{dz}{dr}=\frac{dC_B}{dc_B}\cdot\frac{dc_B}{dz}\cdot\frac{dz}{dr} \tag{B.30}
$$

where $z=\dfrac{r-r_{in}}{L}$ and $c_B=\dfrac{C_B}{C_{A0}}$. The term $\dfrac{dC_B}{dc_B}$ in Eq. (B.30) can be further simplified as follows:

$$
\frac{dC_B}{dc_B}=\frac{d(c_B\cdot C_{A0})}{dc_B}=C_{A0} \tag{B.31}
$$

Introducing Eq. (B.31) and value of $\frac{dz}{dr}$ from Eq. (B.14) into Eq. (B.30).

$$\frac{dC_B}{dr} = C_{A0} \cdot \frac{dc_B}{dz} \cdot \frac{1}{L} = \frac{C_{A0}}{L} \frac{dc_B}{dz} \tag{B.32}$$

Now, taking the derivative of Eq. (B.32).

$$\begin{gathered} \frac{d^2C_B}{dr^2} = \frac{d}{dr}\left(\frac{C_{A0}}{L} \frac{dc_B}{dz}\right) = \frac{C_{A0}}{L} \frac{d}{dr}\left(\frac{dc_B}{dz}\right) = \\ \frac{C_{A0}}{L} \frac{d}{dz}\left(\frac{dc_B}{dz}\right) \frac{dz}{dr} = \frac{C_{A0}}{L} \frac{d^2c_B}{dz^2} \frac{dz}{dr} \end{gathered} \tag{B.33}$$

Putting the value of $\frac{dz}{dr}$ from Eq. (B.14) into Eq. (B.33), yields:

$$\frac{d^2C_B}{dr^2} = \frac{C_{A0}}{L^2} \frac{d^2c_B}{dz^2} \tag{B.34}$$

Introducing Eqs. (B.32) and (B.33) into Eq. (B.29) and converting terms C_B, ${C_A}^{p_1}$ and ${C_B}^{p_2}$ into dimensionless forms, we get:

$$\begin{gathered} D_{B,\text{eff}}\left(\frac{C_{A0}}{L^2} \frac{d^2c_B}{dz^2}\right) + \left(\frac{D_{B,\text{eff}}}{r} - u_D\right)\left(\frac{C_{A0}}{L} \frac{dc_B}{dz}\right) + k_{1,0} \cdot \exp\left(\frac{-E_1}{R_G}\left(\frac{1}{T} - \frac{1}{T_0}\right)\right)(c_A \cdot C_{A0})^{p_1} \\ - k_{2,0} \cdot \exp\left(\frac{-E_2}{R_G}\left(\frac{1}{T} - \frac{1}{T_0}\right)\right)(c_B \cdot C_{A0})^{p_2} - \frac{u_D}{r}(c_B \cdot C_{A0}) = 0 \end{gathered} \tag{B.35}$$

Dividing Eq. (B.35) by $\frac{D_{B,\text{eff}} C_{A0}}{L^2}$ and rearranging results in:

$$\begin{gathered} \frac{d^2c_B}{dz^2} + \left(\frac{1}{\frac{r_{in}}{L} + z} - \frac{u_D L}{D_{B,\text{eff}}}\right)\frac{dc_B}{dz} + \frac{k_{1,0}L^2}{D_{B,\text{eff}}C_{A0}} \cdot \exp\left(\frac{-E_1}{R_G}\left(\frac{1}{T} - \frac{1}{T_0}\right)\right)(c_A \cdot C_{A0})^{p_1} \\ - \frac{k_{2,0}L^2}{D_{B,\text{eff}}C_{A0}} \cdot \exp\left(\frac{-E_2}{R_G}\left(\frac{1}{T} - \frac{1}{T_0}\right)\right)(c_B \cdot C_{A0})^{p_2} - \frac{u_D \ L}{D_{B,\text{eff}}C_{A0}\left(\frac{r_{in}}{L} + z\right)}(c_B \cdot C_{A0}) = 0 \end{gathered} \tag{B.36}$$

Defining the following terms,

$$\begin{aligned} {\varphi_1}^2\psi &= \frac{L^2 {C_{A0}}^{p_1-1} k_{1,0}}{D_{e,B}} \\ {\varphi_2}^2\zeta &= \frac{L^2 {C_{A0}}^{p_2-1} k_{2,0}}{D_{e,B}} \end{aligned} \tag{B.37}$$

Now introducing the dimensionless parameters specified in **Table 3.1**, along with Eq. (B.37), into Eq. (B.36) and incorporating the geometric parameter $\delta = \frac{r_{in}}{L}$, the ultimate dimensionless mass balance equation for component *B* is obtained as follows:

$$\begin{aligned} \frac{d^2 c_B}{dz^2} + \left(\frac{1}{\delta + z} - Pe_m \psi\right)\frac{dc_B}{dz} + {\varphi_1}^2\psi \cdot \exp\left(\gamma_1\left(1 - \frac{1}{\theta}\right)\right){c_A}^{p_1} \\ - {\varphi_2}^2\zeta \cdot \exp\left(\gamma_2\left(1 - \frac{1}{\theta}\right)\right){c_B}^{p_2} - \frac{Pe_m \psi}{\delta + z} c_B = 0 \end{aligned} \tag{B.38}$$

B.3. Heat balance

To obtain the model equation for temperature, we begin by considering the steady-state energy balance over a cylindrical shell given as follows:

$$\begin{aligned} &(\text{Rate of energy in by conduction and flow at } r \text{ in Joules/time}) - \\ &(\text{Rate of energy out by conduction and flow at } r + \Delta r \text{ in Joules/time}) + \\ &(\text{Rate of generation of energy by reaction within } \Delta r \text{ in Joules/time}) = 0 \end{aligned} \tag{B.39}$$

The total heat flux through the porous medium of the membrane involves effective conduction and convective transport terms, which can be expressed as

$$q = q_{cond} + q_{conv} \tag{B.40}$$

The conduction heat transfer rate is based on Fourier's law of heat conduction and defined as:

$$q_{cond} = -K_{\text{eff}} \frac{dT}{dr} \tag{B.41}$$

Similarly, the convection heat transfer rate is given as follows:

$$q_{conv} = \rho_g c_p u_D T \tag{B.42}$$

Combining Eqs. (B.41) and (B.42) into Eq. (B.40), the total heat transfer rate becomes:

$$q \;=\; -K_{\text{eff}}\frac{dT}{dr} + \rho_g c_p u_D T \tag{B.43}$$

The energy balance equation can be stated by utilizing Eq. (B.40) and reaction rates into Eq. (B.39).

$$\begin{aligned} q\cdot(2\pi rh)|_r - \;\; q\cdot(2\pi rh)|_{r+\Delta r} + R_A\cdot 2\pi rh\,\Delta r(-\Delta H_1) \\ + R_B\cdot 2\pi rh\,\Delta r(-\Delta H_2) = 0 \end{aligned} \tag{B.44}$$

Dividing Eq. (B.44) by $2\pi rh$, subsequent rearrangement, and consideration of the limit as $\Delta r \to 0$ yields:

$$\frac{1}{r}\frac{d(q\cdot r)}{dr} \;-\; \left(R_A\cdot(-\Delta H_1) + R_B\cdot(-\Delta H_2)\right) \;=\; 0 \tag{B.45}$$

Introducing Eq. (B.43) into Eq. (B.45), we obtain the following differential equation for the energy balance.

$$\frac{1}{r}\frac{d\left(\left(-K_{\text{eff}}\frac{dT}{dr} + \rho_g c_p u_D T\right)\cdot r\right)}{dr} - \left(R_A\cdot(-\Delta H_1) + R_B\cdot(-\Delta H_2)\right) \;=\; 0 \tag{B.46}$$

Now, taking the constant terms out of the derivative and rearranging, then Eq. (B.46) becomes:

$$-K_{\text{eff}}\frac{d}{dr}\left(r\frac{dT}{dr}\right) + \rho_g c_p u_D \frac{d}{dr}(rT) - \left(R_A\cdot r(-\Delta H_1) + R_B\cdot r(-\Delta H_2)\right) \;=\; 0 \tag{B.47}$$

By rearranging Eq. (B.47), we get the following equation:

$$K_{\text{eff}}\frac{d^2T}{dr^2} + \left(\frac{K_{\text{eff}}}{r} - \rho_g c_p u_D\right)\frac{dT}{dr} + \left(R_A\cdot(-\Delta H_1) + R_B\cdot(-\Delta H_2) - \frac{\rho_g c_p u_D}{r}T\right) \;=\; 0 \tag{B.48}$$

Introducing the terms R_A and R_B into Eq. (B.48), by rearranging, we get the final dimensional equation for temperature.

$$K_{\text{eff}}\frac{d^2T}{dr^2}+\left(\frac{K_{\text{eff}}}{r}-\rho_g c_p u_D\right)\frac{dT}{dr}+k_{1,0}\cdot\exp\left(\frac{-E_1}{R_G}\left(\frac{1}{T}-\frac{1}{T_0}\right)\right)C_A{}^{p_1}\cdot(-\Delta H_1)$$
$$+k_{2,0}\cdot\exp\left(\frac{-E_2}{R_G}\left(\frac{1}{T}-\frac{1}{T_0}\right)\right)C_B{}^{p_2}\cdot(-\Delta H_2)-\frac{\rho_g c_p u_D}{r}T\;=\;0. \tag{B.49}$$

A similar approach, like mass balance equations, is applied here to obtain the dimensionless temperature equation. The first derivative of temperature with respect to the radial position, $\frac{dT}{dr}$, can be expanded by using the chain rule of differentiation as follows:

$$\frac{dT}{dr}=\frac{dT}{dz}\cdot\frac{dz}{dr}=\frac{dT}{d\theta}\cdot\frac{d\theta}{dz}\cdot\frac{dz}{dr} \tag{B.50}$$

where $z=\frac{r-r_{in}}{L}$ and $\theta=\frac{T}{T_0}$. The term $\frac{dT}{d\theta}$ in Eq. (B.50) can be further simplified as follows:

$$\frac{dT}{d\theta}=\frac{d(\theta\cdot T_0)}{d\theta}=T_0 \tag{B.51}$$

Introducing Eq. (B.51) and value of $\frac{dz}{dr}$ from Eq. (B.14) into Eq. (B.50).

$$\frac{dT}{dr}=T_0\cdot\frac{d\theta}{dz}\cdot\frac{1}{L}=\frac{T_0}{L}\frac{d\theta}{dz} \tag{B.52}$$

The second derivative of Eq. (B.52) is found as:

$$\frac{d^2T}{dr^2}=\frac{d}{dr}\left(\frac{dT}{dr}\right)=\frac{d}{dr}\left(\frac{T_0}{L}\cdot\frac{d\theta}{dz}\right)=\frac{T_0}{L}\frac{d}{dz}\left(\frac{d\theta}{dz}\right)\frac{dz}{dr}=\frac{T_0}{L^2}\frac{d^2\theta}{dz^2} \tag{B.53}$$

Substituting the first and second derivatives given by Eqs. (B.52) and (B.53) into Eq. (B.49) and subsequently converting the terms $C_A{}^{p_1}$, $C_B{}^{p_2}$ and T into their respective dimensionless forms, the resultant expression is given as:

$$K_{\text{eff}}\left(\frac{T_0}{L^2}\,\frac{d^2\theta}{dz^2}\right)+\left(\frac{K_{\text{eff}}}{r}-\rho_g c_p u_D\right)\left(\frac{T_0}{L}\frac{d\theta}{dz}\right)+k_{1,0}\cdot\exp\left(\frac{-E_1}{R_G}\left(\frac{1}{T}-\frac{1}{T_0}\right)\right)(c_A\cdot C_{A0})^{p_1}\cdot(-\Delta H_1)$$
$$+k_{2,0}\cdot\exp\left(\frac{-E_2}{R_G}\left(\frac{1}{T}-\frac{1}{T_0}\right)\right)(c_B\cdot C_{A0})^{p_2}\cdot(-\Delta H_2)-\frac{\rho_g c_p u_D}{r}(\theta\cdot T_0)\;=\;0 \tag{B.54}$$

Dividing Eq. (B.54) by $\frac{K_{\text{eff}}T_0}{L^2}$ and rearranging results in:

$$\frac{d^2\theta}{dz^2}+\left(\frac{1}{\frac{r_{in}}{L}+z}-\frac{\rho_g c_p u_D L}{K_{\text{eff}}}\right)\frac{d\theta}{dz}+\frac{k_{1,0}L^2}{K_{\text{eff}}T_0}\cdot\exp\left(\frac{-E_1}{R_G}\left(\frac{1}{T}-\frac{1}{T_0}\right)\right)(c_A\cdot C_{A0})^{p_1}\cdot(-\Delta H_1)$$
$$+\frac{k_{2,0}L^2}{K_{\text{eff}}T_0}\cdot\exp\left(\frac{-E_2}{R_G}\left(\frac{1}{T}-\frac{1}{T_0}\right)\right)(c_B\cdot C_{A0})^{p_2}\cdot(-\Delta H_2)-$$
$$\frac{\rho_g c_p u_D L}{K_{\text{eff}}T_0\left(\frac{r_{in}}{L}+z\right)}(\theta\cdot T_0)\;=\;0 \tag{B.55}$$

Defining and adjusting the following terms,

$$\begin{aligned}\varphi_1{}^2\beta_1 &= \frac{(-\Delta H_1)C_{A0}{}^{p_1}L^2k_{1,0}}{K_{\text{eff}}T_0}\\ \varphi_2{}^2\beta_2\zeta &= \frac{(-\Delta H_2)C_{A0}{}^{p_2}L^2k_{2,0}}{K_{\text{eff}}T_0}\end{aligned} \tag{B.56}$$

Consequently introducing the dimensionless parameters specified in **Table 3.1**, along with Eq. (B.56), into Eq. (B.55) and incorporating the geometric parameter $\delta=\frac{r_{in}}{L}$, the ultimate dimensionless equation for temperature is obtained as follows:

$$\frac{d^2\theta}{dz^2}+\left(\frac{1}{\delta+z}-Pe_h\right)\frac{d\theta}{dz}+\varphi_1{}^2\beta_1\cdot\exp\left(\gamma_1\left(1-\frac{1}{\theta}\right)\right)c_A{}^{p_1}$$
$$+\varphi_2{}^2\beta_2\zeta\cdot\exp\left(\gamma_2\left(1-\frac{1}{\theta}\right)\right)c_B{}^{p_2}-\frac{Pe_h}{\delta+z}\theta\;=\;0. \tag{B.57}$$

Appendix C. Python code implementation

C.1. Code for concentrations *A*, *B* and temperature profiles in series reaction

```
import numpy as np
import matplotlib.pyplot as plt
import scipy.sparse

# Thiele moduli
Phi_1 = 2.5
Phi_2 = 3.0
# diffusivity ratio
psi = 1.0
# reaction rate ratio
# xi = 4.0
# inlet conc power ratio
zeta = 1.0
# reaction exponent p
p = 0.5
# energy generation function
beta1 = 0.01
beta2 = 0.01
# Arrhenius number
gamma1 = 10
gamma2 = 15
# mass Peclet number
Pe = 1.0
# heat Peclet number
Peh = 1.0
# thickness ratio = r_in/L
d = 90

# Dirichlet b.c.'s
ua = 1 # for A
ca = 0 # for B
Ta = 1 # for temperature

# number of spatial grid points
Nx = 199
# generate spatial grid points
x = np.linspace(0, 1, Nx)
# converting x into column (transpose)
xx = x.reshape(-1, 1)
# spatial mesh size
hx = 1 / (Nx - 1)
# number of temporal grid points
Nt = 1000
# mesh for time
```

```
tau = 1 / (Nt - 1)

# IC's
uold = np.ones((Nx - 2, 1))
cold = np.ones((Nx - 2, 1))
Told = np.ones((Nx-2, 1))

# time stepping
unew = np.zeros((Nx - 2, 1))
cnew = np.zeros((Nx - 2, 1))
Tnew = np.zeros((Nx-2,1))

# fixed point iteration at each time step
unew_new = np.zeros((Nx-2,1))
cnew_new = np.zeros((Nx-2,1))
Tnew_new = np.zeros((Nx-2,1))

# for plotting
ufull = np.zeros((Nx, 1))
cfull = np.zeros((Nx, 1))
Tfull = np.zeros((Nx,1))

# identity matrix
I = np.eye(Nx - 2)

# Diagonals for Matrix A , component A
main  = np.zeros(Nx-2)
lower = np.zeros(Nx-2)
upper = np.zeros(Nx-1)
main[:]  = -2 / (hx ** 2) + (1 / (d + x[1:Nx-1]) - Pe) / (hx) - Pe / ( (d +
x[1:Nx-1]))
lower[:] = 1 / ((hx ** 2)) - (1 / (d + x[2:Nx]) - Pe) / (hx)
upper[:] = 1 / ((hx ** 2))
# Defining the sparse matrix A
A = scipy.sparse.diags(diagonals=[main, lower, upper],
    offsets=[0, -1, 1], shape=(Nx-2, Nx-2), format='csr')
# modify zero r.h.s because of Dirichlet b.c.’s
fu = np.zeros((Nx - 2, 1))
fu[0] = 1 / (hx ** 2) - (1 / (d + xx[1]) - Pe) / hx
# Applying Neumann b.c.'s
A[Nx - 3, Nx - 3] = A[Nx - 3, Nx - 3] + 1 / (hx ** 2)

# Diagonals for Matrix M , component B
main1  = np.zeros(Nx-2)
lower1 = np.zeros(Nx-2)
upper1 = np.zeros(Nx-1)
main1[:]  = -2 / (hx ** 2) + (1 / (d + x[1:Nx-1]) - (Pe*psi)) / (hx) -
(Pe*psi) / ( (d + x[1:Nx-1]))
lower1[:] = 1 / ((hx ** 2)) - (1 / (d + x[2:Nx]) - (Pe*psi)) / (hx)
```

```
upper1[:] = 1 / ((hx ** 2))
# Defining the sparse matrix M
M = scipy.sparse.diags(diagonals=[main1, lower1, upper1],
    offsets=[0, -1, 1], shape=(Nx-2, Nx-2), format='csr')
# modify zero r.h.s because of Dirichlet b.c.’s
fc = np.zeros((Nx - 2, 1))
# Applying Neumann b.c.'s
M[Nx - 3, Nx - 3] = M[Nx - 3, Nx - 3] + 1 / (hx ** 2)

# Diagonals for Matrix B, temperature
main2  = np.zeros(Nx-2)
lower2 = np.zeros(Nx-2)
upper2 = np.zeros(Nx-1)
main2[:]  = -2 / (hx ** 2) + (1 / (d + x[1:Nx-1]) - Peh) / (hx) - Peh / ((d +
x[1:Nx-1]))
lower2[:] = 1 / ((hx ** 2)) - (1 / (d + x[2:Nx]) - Peh) / ( hx)
upper2[:] = 1 / ( (hx ** 2))
# Defining the sparse matrix B
B = scipy.sparse.diags(diagonals=[main2, lower2, upper2],
    offsets=[0, -1, 1], shape=(Nx-2, Nx-2), format='csr')
# modify zero r.h.s because of Dirichlet b.c.’s
fT = np.zeros((Nx - 2, 1))
fT[0] = 1 / (hx ** 2) - (1 / (d + xx[1]) - Peh) / hx
# Applying Neumann b.c.'s
B[Nx - 3, Nx - 3] = B[Nx - 3, Nx - 3] + 1 / (hx ** 2)

# time marching scheme main equations
Nt_iter = Nt
for i in range(Nt_iter):
    # updating old values
    unew_old = uold
    cnew_old = cold
    Tnew_old = Told
    for j in range(2):
        unew_new = np.linalg.solve(I - 1/2*tau * A, uold + 1/2*tau *
A.dot(uold) -  1/2*Phi_1** 2 * tau * np.exp(gamma1*(1 - 1/Told))
*(np.maximum(unew_old, 0)**p + np.maximum(uold, 0)**p ) + tau * fu)
        cnew_new = np.linalg.solve(I - 1/2*tau * M, cold + 1/2*tau *
M.dot(cold) + Phi_1 ** 2 * psi * tau * np.exp(gamma1*(1 - 1 / Told)) *
np.maximum(uold, 0)**p - 1/2* tau * Phi_2**2 * zeta * np.exp(gamma2 *(1 - 1/
Told))*(np.maximum(cnew_old, 0)**p + np.maximum(cold, 0)**p ))
        Tnew_new = np.linalg.solve(I - 1/2*tau * B, Told + 1/2*tau *
B.dot(Told) +  1/2*tau * beta1 * Phi_1 ** 2 * (np.exp(gamma1 * (1 - 1 / Told))
+ np.exp(gamma1 * (1 - 1 / Tnew_old))) * np.maximum(uold, 0) ** p +
1/2*tau*beta2*Phi_2**2*zeta * (np.exp(gamma2 * (1 - 1 / Told)) + np.exp(gamma2
* (1 - 1 / Tnew_old))) * np.maximum(cold, 0) ** p + tau * fT)
        uold =  0.5*np.maximum(unew_new, 0) +  0.5*np.maximum(uold, 0)
        cold =  0.5*np.maximum(cnew_new, 0) +  0.5*np.maximum(cold, 0)
        Told =  0.5*np.maximum(Tnew_new, 0) +  0.5*np.maximum(Told, 0)
```

```
    unew = np.maximum(unew_new, 0)
    ufull[0] = ua
    ufull[1:Nx-1] = unew
    ufull[Nx-1] = unew[Nx-3]
    cnew = np.maximum(cnew_new, 0)
    cfull[0] = ca
    cfull[1:Nx-1] = cnew
    cfull[Nx-1] = cnew[Nx-3]
    Tnew = np.maximum(Tnew_new, 0)
    Tfull[0] = Ta
    Tfull[1:Nx-1] = Tnew
    Tfull[Nx-1] = Tnew[Nx-3]


# Plotting

plt.figure(1)
# Setting the x-axis and y-axis limits for proper plot alignment
plt.xlim(0, 1)
plt.ylim(None, 1)
plt.plot(x, ufull, '-k')
plt.xlabel('Dimensionless distance, z(-)')
plt.ylabel('Dimensionless concentration, $c_A$(-)')
plt.savefig("component_A.png", dpi = 1000)
plt.savefig("component_A.pdf", dpi = 600)
plt.show()

plt.figure(2)
# Setting the x-axis and y-axis limits for proper plot alignment
plt.xlim(0, 1)
plt.ylim(0, 0.1)
plt.plot(x, cfull, '-k')
plt.xlabel('Dimensionless distance, z(-)')
plt.ylabel('Dimensionless concentration, $c_B$(-)')
plt.savefig("component_B.png", dpi = 1000)
plt.savefig("component_B.pdf", dpi = 600)
plt.show()

plt.figure(3)
# Setting the x-axis and y-axis limits for proper plot alignment
plt.xlim(0, 1)
plt.ylim(1, 1.017)
plt.plot(x, Tfull, '-k')
plt.xlabel('Dimensionless distance, z(-)')
plt.ylabel('Dimensionless temperature, $\\theta$(-)')
plt.savefig("Temperature.png", dpi = 1000)
plt.savefig("Temperature.pdf", dpi = 600)
plt.show()
```

C.2. Code for selectivity, yield and conversion under non-isothermal conditions

```
import numpy as np
import matplotlib.pyplot as plt
import scipy.sparse

# Parameters
# Thiele modulus
# Phi_1 = 2.5
# Phi_2 = 1.2
# diffusivity ratio
psi = 1.0
# inlet conc power ratio
zeta = 1.0
# reaction exponent
p = 0.8
# energy generation function
beta1 = 0.01
beta2 = 0.01
# Arrhenius number
gamma1 = 10
gamma2 = 15
# mass Peclet number
# Pe = 1.0
# heat Peclet number
Peh = 0
# thickness ratio = r_in/L
d = 10

# Dirichlet b.c.'s
ua = 1 # for A
ca = 0 # for B
Ta = 1 # for temperature

# number of spatial grid points
Nx = 199
# generate spatial grid points
x = np.linspace(0, 1, Nx)
# converting x into column (transpose)
xx = x.reshape(-1, 1)
# spatial mesh size
hx = 1 / (Nx - 1)
# number of temporal grid points
Nt = 500
# mesh for time
tau = 1 / (Nt - 1)
```

```
# Initial conditions
uold = np.ones((Nx - 2, 1))
cold = np.ones((Nx - 2, 1))
Told = np.ones((Nx-2, 1))

# Lists to store results
conversion_values_list = []
selectivity_values_list = []
yield_values_list = []

# Thiele modulus values to vary
Phi_values = [2.2, 2.6, 3.1]

# Loop for Thiele modulus values
for Phi in Phi_values:
    # Update Thiele modulus value
    Phi_1 = Phi
    Phi_2 = Phi

    # Generate spatial grid points
    x = np.linspace(0, 1, Nx)
    xx = x.reshape(-1, 1)
    hx = 1 / (Nx - 1)

    # Initial conditions
    uold = np.ones((Nx - 2, 1))
    cold = np.ones((Nx - 2, 1))
    Told = np.ones((Nx-2, 1))

    # time stepping
    unew = np.zeros((Nx - 2, 1))
    cnew = np.zeros((Nx - 2, 1))
    Tnew = np.zeros((Nx-2, 1))

    # fixed point iteration at each time step
    unew_new = np.zeros((Nx-2, 1))
    cnew_new = np.zeros((Nx-2, 1))
    Tnew_new = np.zeros((Nx-2, 1))

    # for plotting
    ufull = np.zeros((Nx, 1))
    cfull = np.zeros((Nx, 1))
    Tfull = np.zeros((Nx, 1))

    #identity matrix
    I = np.eye(Nx - 2)

    Nt_iter = Nt
```

```
    # Creating array for mass peclet numbers
    mass_peclet_numbers = np.linspace(0, 15, 50)

    # Lists to store results for each Mass Peclet Number
    conversion_values = []
    selectivity_values = []
    yield_values = []

    # Loop over mass peclet values
    for Pe in mass_peclet_numbers:
        # Diagonals for Matrix A , component A
        main = np.zeros(Nx-2)
        lower = np.zeros(Nx-2)
        upper = np.zeros(Nx-1)
        main[:] = -2 / (hx ** 2) + (1 / (d + x[1:Nx-1]) - Pe) / (hx) - Pe / (
(d + x[1:Nx-1]))
        lower[:] = 1 / ((hx ** 2)) - (1 / (d + x[2:Nx]) - Pe) / (hx)
        upper[:] = 1 / ((hx ** 2))
        # Defining the sparse matrix A
        A = scipy.sparse.diags(diagonals=[main, lower, upper],
                               offsets=[0, -1, 1], shape=(Nx-2, Nx-2),
format='csr')
        # modify zero r.h.s because of Dirichlet b.c.’s
        fu = np.zeros((Nx - 2, 1))
        fu[0] = 1 / (hx ** 2) - (1 / (d + xx[1]) - Pe) / hx
        # Applying Neumann b.c.'s
        A[Nx - 3, Nx - 3] = A[Nx - 3, Nx - 3] + 1 / (hx ** 2)

        # Diagonals for Matrix M , component B
        main1 = np.zeros(Nx-2)
        lower1 = np.zeros(Nx-2)
        upper1 = np.zeros(Nx-1)
        main1[:] = -2 / (hx ** 2) + (1 / (d + x[1:Nx-1]) - (Pe*psi)) / (hx) -
(Pe*psi) / ( (d + x[1:Nx-1]))
        lower1[:] = 1 / ((hx ** 2)) - (1 / (d + x[2:Nx]) - (Pe*psi)) / (hx)
        upper1[:] = 1 / ((hx ** 2))
        # Defining the sparse matrix M
        M = scipy.sparse.diags(diagonals=[main1, lower1, upper1],
                               offsets=[0, -1, 1], shape=(Nx-2, Nx-2),
format='csr')
        # modify zero r.h.s because of Dirichlet b.c.’s
        fc = np.zeros((Nx - 2, 1))
        # Applying Neumann b.c.'s
        M[Nx - 3, Nx - 3] = M[Nx - 3, Nx - 3] + 1 / (hx ** 2)

        # Diagonals for Matrix B, temperature
        main2 = np.zeros(Nx-2)
        lower2 = np.zeros(Nx-2)
        upper2 = np.zeros(Nx-1)
```

```
        main2[:] = -2 / (hx ** 2) + (1 / (d + x[1:Nx-1]) - Peh) / (hx) - Peh /
((d + x[1:Nx-1]))
        lower2[:] = 1 / ((hx ** 2)) - (1 / (d + x[2:Nx]) - Peh) / ( hx)
        upper2[:] = 1 / ( (hx ** 2))
        # Defining the sparse matrix B
        B = scipy.sparse.diags(diagonals=[main2, lower2, upper2],
                               offsets=[0, -1, 1], shape=(Nx-2, Nx-2),
format='csr')
        # modify zero r.h.s because of Dirichlet b.c.'s
        fT = np.zeros((Nx - 2, 1))
        fT[0] = 1 / (hx ** 2) - (1 / (d + xx[1]) - Peh) / hx
        # Applying Neumann b.c.'s
        B[Nx - 3, Nx - 3] = B[Nx - 3, Nx - 3] + 1 / (hx ** 2)

        # time marching scheme main equations
        for i in range(Nt_iter):
            # updating old values
            unew_old = uold
            cnew_old = cold
            Tnew_old = Told
            for j in range(2):
                unew_new = np.linalg.solve(I - 1/2*tau * A, uold + 1/2*tau *
A.dot(uold) -  1/2*Phi_1** 2 * tau * np.exp(gamma1*(1 - 1/Told))
*(np.maximum(unew_old, 0)**p + np.maximum(uold, 0)**p ) + tau * fu)
                cnew_new = np.linalg.solve(I - 1/2*tau * M, cold + 1/2*tau *
M.dot(cold) + Phi_1 ** 2 * psi * tau * np.exp(gamma1*(1 - 1 / Told)) *
np.maximum(uold, 0)**p - 1/2* tau * Phi_2**2 * zeta * np.exp(gamma2 *(1 - 1/
Told))*(np.maximum(cnew_old, 0)**p + np.maximum(cold, 0)**p ))
                Tnew_new = np.linalg.solve(I - 1/2*tau * B, Told + 1/2*tau *
B.dot(Told) +  1/2*tau * beta1 * Phi_1 ** 2 * (np.exp(gamma1 * (1 - 1 / Told))
+ np.exp(gamma1 * (1 - 1 / Tnew_old))) * np.maximum(uold, 0) ** p +
1/2*tau*beta2*Phi_2**2*zeta * (np.exp(gamma2 * (1 - 1 / Told)) + np.exp(gamma2
* (1 - 1 / Tnew_old))) * np.maximum(cold, 0) ** p + tau * fT)
                uold =  0.5*np.maximum(unew_new, 0) +  0.5*np.maximum(uold, 0)
                cold =  0.5*np.maximum(cnew_new, 0) +  0.5*np.maximum(cold, 0)
                Told =  0.5*np.maximum(Tnew_new, 0) +  0.5*np.maximum(Told, 0)
            unew = np.maximum(unew_new, 0)
            ufull[0] = ua
            ufull[1:Nx-1] = unew
            ufull[Nx-1] = unew[Nx-3]
            cnew = np.maximum(cnew_new, 0)
            cfull[0] = ca
            cfull[1:Nx-1] = cnew
            cfull[Nx-1] = cnew[Nx-3]
            Tnew = np.maximum(Tnew_new, 0)
            Tfull[0] = Ta
            Tfull[1:Nx-1] = Tnew
            Tfull[Nx-1] = Tnew[Nx-3]
```

```
        # Calculate conversion, selectivity, and yield
        X = 1 - ufull[Nx-1] #Conversion
        Sel = cfull[Nx-1] / X  #selectivity
        Y = X * Sel   #yield

        # Store for this Thiele modulus
        conversion_values.append(X)
        selectivity_values.append(Sel)
        yield_values.append(Y)

    # Store for Thiele modulus in the main loop
    conversion_values_list.append(conversion_values)
    selectivity_values_list.append(selectivity_values)
    yield_values_list.append(yield_values)

# ploting
plt.figure(1)
# Defining line styles and colors for plot
line_styles = ['--', '-.', '-']
colors = ['b', 'g', 'k']
# Plotting conversion
for i, Phi in enumerate(Phi_values):
    # Setting the x-axis and y-axis limits for proper plot alignment
    plt.xticks(np.arange(0, 16, step=3))
    plt.xlim(0, 15)
    plt.ylim(0.3,1.0)
    plt.plot(mass_peclet_numbers, conversion_values_list[i], line_styles[i],
color=colors[i], label=f'$ϕ_1$ = {Phi_values[i]}, $ϕ_2$ = {Phi_values[i]}',
linewidth=1.2)

plt.xlabel('Mass Peclet Number, $Pe_m$(-)')
plt.ylabel('Conversion, X(-)')
plt.legend()
plt.savefig('conversion_noniso.png', dpi = 1000)
plt.savefig('conversion_noniso.pdf', dpi = 600)
plt.show()

# Plotting Selectivity
plt.figure(2)
for i, Phi in enumerate(Phi_values):
    # Setting the x-axis and y-axis limits for proper plot alignment
    plt.xticks(np.arange(0, 16, step=3))
    plt.xlim(0, 15)
    plt.ylim(0,0.6)
    plt.plot(mass_peclet_numbers, selectivity_values_list[i], line_styles[i],
color=colors[i], label=f'$ϕ_1$ = {Phi_values[i]}, $ϕ_2$ = {Phi_values[i]}',
linewidth=1.2)

plt.xlabel('Mass Peclet Number, $Pe_m$(-)')
```

```
plt.ylabel('Selectivity, S(-)')
plt.legend()
plt.savefig('selectivity_noniso.png', dpi = 1000)
plt.savefig('selectivity_noniso.pdf', dpi = 600)
plt.show()

# Plotting Yield
plt.figure(3)
for i, Phi in enumerate(Phi_values):
    # Setting the x-axis and y-axis limits for proper plot alignment
    plt.xticks(np.arange(0, 16, step=3))
    plt.xlim(0, 15)
    plt.yticks(np.arange(0.03, 0.33, step=0.05))
    plt.ylim(0.03,0.28)
    plt.plot(mass_peclet_numbers, yield_values_list[i], line_styles[i],
color=colors[i], label=f'$ϕ_1$ = {Phi_values[i]}, $ϕ_2$ = {Phi_values[i]}',
linewidth=1.2)

plt.xlabel('Mass Peclet Number, $Pe_m$(-)')
plt.ylabel('Yield, Y(-)')
plt.legend()
plt.savefig('yield_noniso.png', dpi = 1000)
plt.savefig('yield_noniso.pdf', dpi = 600)
plt.show()
```

C.3. Code for productivity calculations

```
import numpy as np
import matplotlib.pyplot as plt
import scipy.sparse

# Thiele modulus
Phi = 2.5
# porosity
e = 0.6
# reaction exponent p
p = 1.5
# mass Peclet number
Pe = 1.0
# thickness ratio = r_in/L
d = 10
# Dirichlet b.c.'s
# ua = 1
# number of spatial grid points
Nx = 50
# generate spatial grid points
x = np.linspace(0, 1, Nx)
# converting x into column (transpose)
xx = x.reshape(-1, 1)
# spatial mesh size
hx = 1 / (Nx - 1)
# number of temporal grid points
Nt = 1000000
N_periods = 2

# Initial conditions
uold = np.ones((Nx - 2, 1))

# time stepping
unew = np.zeros((Nx - 2, 1))

# fixed point iteration at each time step
unew_new = np.zeros((Nx-2,1))

# for plotting
ufull = np.zeros((Nx, 1))

# identity matrix
I = np.eye(Nx - 2)

# Diagonals for Matrix A, component A
main  = np.zeros(Nx-2)
lower = np.zeros(Nx-2)
```

```
upper = np.zeros(Nx-1)
main[:]  = -2 / (hx ** 2) + (1 / (d + x[1:Nx-1]) - Pe) / (hx) - Pe / ( (d +
x[1:Nx-1]))
lower[:] = 1 / ((hx ** 2)) - (1 / (d + x[2:Nx]) - Pe) / (hx)
upper[:] = 1 / ((hx ** 2))
# Defining the sparse matrix A
A = scipy.sparse.diags(diagonals=[main, lower, upper],
    offsets=[0, -1, 1], shape=(Nx-2, Nx-2), format='csr')
# modify zero r.h.s because of Dirichlet b.c.’s
fu = np.zeros((Nx - 2, 1))
fu[0] = 1 / (hx ** 2) - (1 / (d + xx[1]) - Pe) / hx
# Applying Neumann b.c.'s
A[Nx - 3, Nx - 3] = A[Nx - 3, Nx - 3] + 1 / (hx ** 2)

# Define a range of T_c and delta_m_A values
T_c_values = [2000 * np.pi, 8000 * np.pi, 10000 * np.pi, 20000 * np.pi, 80000
* np.pi, 320000 * np.pi, 2560000 * np.pi, 20480000 * np.pi]
delta_m_A_values = np.linspace(0.1, 0.99, 11)  # Range of delta_mA

# Initializing in order to store the productivity values
productivity_values = np.zeros((len(T_c_values) * len(delta_m_A_values), 3))

index = 0
# Loop over T_c values in order to calculate respective omega_mA
for i, T_c in enumerate(T_c_values):
    # Loop over delta_mA values
    for j, delta_m_A in enumerate(delta_m_A_values):
        Nt_iter = Nt
        u_results = np.zeros((Nt_iter, Nx))
        omega_m_A = (2 * np.pi) / T_c
        T_final = N_periods * T_c
        tau = T_final / (Nt - 1)

        # time marching scheme main equations
        for k in range(Nt_iter):
         # Calculate the time-dependent boundary conditions at each time step
            tt_k   = k * tau
            tt_k_1 = (k+1)*tau
            ua_1 = 1 + delta_m_A * np.sin(omega_m_A * tt_k)
            ua_2 = 1 + delta_m_A * np.sin(omega_m_A * tt_k_1)
            ua = 0.5*(ua_1 + ua_2)
            # updating the old values
            unew_old = uold

            for m in range(2):
                unew_new = np.linalg.solve(I - 1/(2*e) * tau * A, uold +
1/(2*e) * tau * A.dot(uold) -  1/(2*e) * Phi ** 2 * tau *(np.maximum(unew_old,
0)**p + np.maximum(uold, 0)**p ) + (tau*fu*ua)/e)
```

```
                uold =  0.5*np.maximum(unew_new, 0) +  0.5*np.maximum(uold, 0)
            unew = np.maximum(unew_new, 0)
            ufull[0] = ua
            ufull[1:Nx-1] = unew
            ufull[Nx-1] = unew[Nx-3]

            u_results[k, :] = ufull.flatten()

        # Initializing array to store productivity values
        productivity_values_ij = []

        # Defining terms for productivity calculation
        l = 1.0  # length of cylinder
        De_A = 1.0  # effective diffusivity
        c_bA = 1.0  # bulk concentration

        for k in range(Nt_iter):
            TT = k * tau
            # Calculate the concentration gradient at x=0
            dC_dx_0 = (-3 * u_results[k, 0] + 4 * u_results[k, 1] -
u_results[k, 2]) / (2 * hx)

            # terms to calculate productivity
            term1 = -d * dC_dx_0
            term2 = Pe * (1 + delta_m_A * np.sin(omega_m_A * TT)) * d
            term3 = Pe * (u_results[k, Nx-1] * (1 + d))

            # Calculate the productivity
            productivity = 2 * np.pi * l * De_A * c_bA * (term1 + term2 -
term3)

            # Store the productivity value
            productivity_values_ij.append(productivity)

        # Calculate average productivity excluding the transient period
        transient_period = 10  # can be varied according to conditions
        average_productivity = (1 / (T_final - transient_period * tau)) *
np.trapz(productivity_values_ij[transient_period:], dx=tau)

        # Store the productivity value along with omega_m_A and delta_m_A
        productivity_values[index, :] = [(2*np.pi)/T_c, delta_m_A,
average_productivity]
        index += 1

        # Print
        print(f'omega = {omega_m_A:.10f}, delta_m_A = {delta_m_A:.2f}, Average
Productivity (J): {average_productivity}')
```